Progress Toward a Search for a Permanent Electric Dipole Moment in Liquid ^{129}Xe

Micah Ledbetter

A Dissertation

Presented to the Faculty

of Princeton University

in Candidacy for the Degree

of Doctor of Philosophy

Recommended for Acceptance

by the Department of

Physics

November, 2005

Abstract

Here we report progress toward the measurement of a permanent electric dipole moment (EDM) in hyperpolarized liquid ^{129}Xe which violates invariance under both parity and time reversal. The standard model (SM) predicts atomic EDMs well beyond current experimental limits while many natural extensions to the SM predict EDMs within the expected sensitivity of current experiments. Hence the search for a non-zero EDM is viewed as an ideal test for new physics.

Liquid ^{129}Xe is an attractive medium in which to perform such a search because it has a high number density and a high electric field breakdown strength. For experimentally realizable parameters it should be possible to achieve a sensitivity of $\sim 10^{-32}\,e$-cm for one day of integration, several orders of magnitude beyond current experimental limits on EDMs.

In preparation for performing a search for an EDM in liquid xenon, we have conducted a thorough experimental and theoretical investigation of the spin dynamics of hyperpolarized liquid ^{129}Xe. In a highly polarized liquid magnetic dipolar interactions can strongly influence spin precession. For small tip angles of the magnetization away from the holding field, the system is insensitive to perturbations, leading to extended free induction decays. For large tip angles the system develops a dynamical instability so that spin precession due to a small magnetic field gradient is amplified exponentially relative to the non-interacting case. In principle, this amplification can be quite large, leading to enhanced sensitivity of spin precession measurements when noise in the detection system is much greater than spin-projection noise.

Experimentally, we have achieved amplification of spin precession due to a small applied field gradient by a factor of 9.5 relative to the non-interacting case in the large tip angle regime. Considerable improvement is expected with further optimization of high order gradients. In the small tip angle regime we have realized an extension of the free induction decay by up to a factor of 100 compared to the non-interacting case. We discuss how these two different regimes can be used in a search for an EDM in liquid xenon and analyze the expected sources of systematic effects.

Acknowledgements

First I would like to thank my advisor, Professor Michael Romalis, who has guided my development as a scientist. Without his experience, insights, whip-cracking, and funding, none of this would have been possible. Professor Will Happer also deserves a great deal of thanks for fostering an environment in which atomic physics could flourish, and for developing many of the experimental techniques that make this work possible. I am also indebted to Igor Savukov who has provided many insights into numerical modelling. I owe a great deal of thanks to my current labmates, friends and collaborators, Tom Kornack, Scott Seltzer and Rajat Ghosh. It has been a pleasure to share with you the failures and successes that every experimental physicist must go through. To my kindred atomic physics students on the second floor, Amber Post, Brian Patton, Yuan Yu Jau, Nhan Tran and Nick Kuzma, thank you for providing an exceptional environment in which to study physics. Finally, Charles Sule, no one can match your expertise in filling nitrogen tanks!

My friend Eric "Bivy" (Shea-)Brown has been my climbing partner and constant companion in academics from the early days at Berkeley. Without your encouragement, I may not have gotten off the couch to take the GRE! Colleen Shea-Brown, thank you for keeping us from working too hard and getting us out on the rock and ice! Tony Lobay, it's time to climb something big! My friends in Capoeira, life without you would have been lonely.

Finally, I would not be where I am today without the support of my mother and father, Ellen and Denis, and my sister Emma. I still remember the day I was handed a screwdriver and urged to go tinker. Thank you all for encouraging me onward in my academic journey.

Contents

List of Figures

List of Tables

Chapter 1

Introduction

1.1 Overview

The motivation for this work is to conduct a search for a T, P odd permanent electric dipole moment (EDM) in liquid ^{129}Xe. By the CPT theorem a non-zero EDM also violates invariance under CP, the combined symmetry of charge and parity. The standard model predicts EDMs many orders of magnitude beyond current experimental limits, and hence a non-zero EDM is an unambiguous signal for new physics, the interpretation of which is unclouded by difficult standard model calculations.

In the proposed experiment, two SQUID (superconducting quantum interference device) magnetometers will detect the precession of the spins in a sample with a common magnetic field divided into two regions of opposing electric fields, as illustrated in Fig. 1.1. The signature of an EDM would be a shift in the Larmor precession frequencies of spin polarized nuclei in regions of opposing electric field. Since the SQUID magnetometers preferentially detect the magnetization in either half of the cell, this would show up as a growing phase difference between the two SQUID signals.

To perform such a search, a thorough understanding of the dynamics of a hyperpolarized liquid in a low magnetic field environment in the presence of long range magnetic dipolar interactions is crucial. We find that there are two dramatically distinct regimes depending

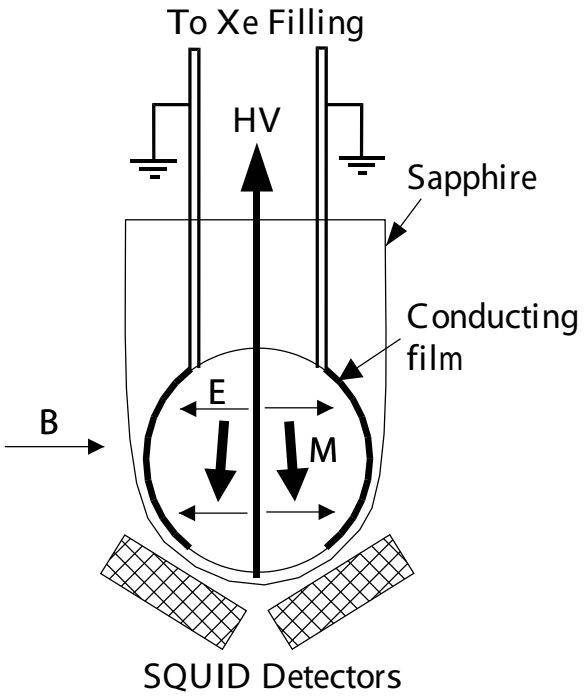

Figure 1.1: Schematic of the proposed experiment. Two SQUID magnetometers detect the oscillating magnetic field generated by the precessing spins.

on the tip angle of the magnetization with respect to the holding field. For small tip angles we find that the system is remarkably insensitive to perturbations such as applied field gradients or initial magnetization inhomogeneities, an effect known as spectral clustering. In the large tip angle regime, the system develops a dynamical instability and gradients of the magnetization grow exponentially in response to a very small linear applied field gradient.

In the context of a search for an EDM, the latter behavior is very exciting because gradients of the magnetization would be amplified exponentially in response to the interaction of a non-zero EDM with an applied electric field gradient. Rather than having to wait a long time for spin precession due to the electric field to grow large enough to be measured by the SQUIDs, dipolar interactions amplify it exponentially, raising it above the noise level of the SQUID detectors. The possibility of performing a search for an EDM in the small tip angle regime is also discussed.

This work is organized as follows: This chapter presents background on the physics behind atomic electric dipole moments, the experimental techniques we employ and summarizes the most striking features of long range dipolar interactions. Chapter 2 discusses in depth our particular experimental setup. Chapter 3 presents a detailed discussion of the methods we developed to model the aforementioned non-linear effects arising from long range dipolar interactions. We compare our experimental results to theory in Chapter 4. In Chapter 5 we discuss two different schemes for performing an EDM experiment and their expected sensitivity. We also estimate the expected sources of systematic effects. Finally, in Chapter 6 we conclude by summarizing our findings.

1.2 Motivating the search for an Electric Dipole Moment

The search for a permanent electric dipole moment, proportional to the spin vector of a spin 1/2 particle or nucleus,

$$\mathbf{d} = d\frac{\mathbf{S}}{s}, \tag{1.1}$$

has long been hailed as an ideal search for new physics. The possibility of a non-zero permanent electric dipole moment of a spin 1/2 particle was first proposed by Ramsey and Purcell [1]. Prior to this work, permanent electric dipole moments were generally assumed to be zero on the basis that the laws of physics should be invariant under parity. It is straightforward to show that Eq. 1.1 violates parity: the electric dipole operator $\mathbf{d} = \int \mathbf{r}\rho(\mathbf{r})d^3\mathbf{r}$ is odd under parity, while the spin is an axial vector, even under parity. An experimental search for a neutron EDM was reported in Ref. [2], setting a limit of $d_n < 5 \times 10^{-20}\, e-$cm. The experimental limit on the neutron EDM has been improved by a spectacular 6 orders of magnitude since this first measurement. The current limit on the neutron EDM and several other systems of interest are summarized in Table 1.1.

Parity non-conservation, first observed through β decay of the ^{60}Co nucleus [7] and later in a number of other atomic systems, was instrumental in developing the vector-axial vector nature of weak interactions. Following the observation of parity violation, Landau[8] pointed out that a permanent electric dipole moment also violates time reversal invariance,

System	Limit (e-cm)	Reference
^{199}Hg	2×10^{-28}	[3]
^{129}Xe	4×10^{-27}	[4]
neutron	6.3×10^{-26}	[5]
electron	1.6×10^{-27}	[6]

Table 1.1: Current best limits on the electric dipole moments of ^{199}Hg, ^{129}Xe, neutron and the electron.

at the time thought to be a good symmetry. The discovery of CP violation (the combined symmetries of charge and parity) in the K^0 system[9] brought about renewed interest in the search for a permanent EDM, because a violation of CP implies a violation of time reversal symmetry by the CPT theorem.

The argument that an EDM violates time reversal symmetry is similar to that given above for parity. The electric dipole moment operator $\mathbf{d}$ is even under T while the spin $\mathbf{s}$ is odd under T. If there were another degree of freedom so that $\mathbf{d}$ could be either parallel or antiparallel to the spin $\mathbf{s}$ the existence of a non-zero EDM would not violate T. However there is considerable evidence that no such degeneracy exists. For example, the atomic and nuclear shell models clearly exclude such a possibility for electrons and nucleons. Hence we conclude the T violating nature of Eq. 1.1 for $d \neq 0$. For a more general discussion of time reversal invariance, the reader is urged to consult Ref. [10].

CP violation in the K_0 meson is well accounted for in the standard model through a complex phase in the CKM matrix. Standard model physics however predicts very small electric dipole moments, far beyond current experimental sensitivity. Exact calculations of EDMs in the standard model are difficult because contributions to EDMs occur at the three loop level. Based on dimensional analysis, estimates for the electron and neutron EDM in the standard model are $d_e = 10^{-40}\,e$-cm and $d_n = 10^{-32} - 10^{-31}\,e$-cm[11] respectively. Thus the search for a permanent electric dipole moment is still hailed as an unambiguous test of CP violation beyond the standard model.

The search for CP violation outside the standard model is phenomenologically motivated by the observed baryon asymmetry of the universe. We look around and all we see is matter, no antimatter. A good thing too, as they have a tendency to annihilate each

other on contact! To account for this, baryogenesis requires (**1**) a departure from thermal equilibrium (**2**) a baryon number nonconserving process and (**3**) CP violation.[12] The standard model possesses all three features, however most of the literature indicates that CP violation arising from a single phase in the CKM matrix is insufficient to account for the observed baryon asymmetry of our Universe [13, 14, 15]. Recently, however, there has been a suggestion that the CKM phase is sufficient to account for baryogenesis if the Yukawa couplings between quarks and the Higgs were large prior to nucleosynthesis[16]. For a comprehensive review of baryogenisis, see Ref. [17].

While there are a large number of possible extensions to the standard model that violate CP and naturally generate large electric dipole moments, the most cherished among theorists is supersymmetry, a symmetry between bosonic and fermionic degrees of freedom. For every fermion, there is a supersymmetric scaler partner the "sfermion", and for every gauge boson there is a ferimonic partner, the "gaugino." Supersymmetry was originally motivated to explain the mass spectrum of the known particles. From measurements of the properties of the electroweak interactions, it is known that the Higgs mass must be on the order of $m_H^{\approx} 100\,\mathrm{GeV}$. However coupling between the Higgs and the fermions generate corrections to the mass of the Higgs. The largest of these is due to coupling with the top quark, depending quadratically on the cutoff momentum beyond which point new physics such as string theory enters into the problem. Assuming the cutoff is at the Planck scale, for the top quark these corrections can be up to 30 orders of magnitude larger than the desired value $m_H^2 \approx -(100\,\mathrm{GeV})^2$. This requires a great deal of fine tuning of the bare Higgs mass. Since all the quarks and leptons, as well as the electroweak gauge bosons Z^0 and $W^{\pm}$ owe their mass to coupling with the Higgs, they become sensitive to the cutoff scale. Conveniently, the contributions to the Higgs mass from the fermions can be exactly cancelled by similar contributions from their superpartners. Supersymmetry also provides a mechanism for unifying the electroweak and strong interactions, as well as a candidate for dark matter (the lightest supersymmetric partner) and is required by string theory. Despite a great deal of effort, there has been no evidence of SUSY at particle accelerators and cur-

rent limits on EDMs place serious constraints on the minimally supersymmetric standard model (MSSM). Weinberg discusses supersymmetry in detail in Ref. [18]

1.3 General features of EDM experiments

The Hamiltonian of a spin 1/2 particle possessing both electric and magnetic dipole moments in a combined electric and magnetic field is

$$H = -\left(\mu \frac{\mathbf{S}}{s} \cdot \mathbf{B} + d \frac{\mathbf{S}}{s} \cdot \mathbf{E}\right). \tag{1.2}$$

Thus, the atoms precess around the combined electric and magnetic fields (assuming both the fields are either parallel or antiparallel to each other) with a frequency

$$h\nu = 2\mu B \pm 2dE \tag{1.3}$$

In principle, all that is required to search for an electric dipole moment is to look for a shift in the Larmor precession frequency associated with the application of the electric field. Comagnetometers are typically used to distinguish between frequency shifts due to fluctuations in the magnetic field and a true EDM signal.

Electric dipole moment experiments are naturally divided into three categories: the search for a neutron EDM, electron EDM or the EDM of a diamagnetic atom. In the MSSM, the EDM of each of these particles results from a linear combination of several different CP violating phases, and hence, to fully constrain the MSSM it is important to perform experiments in each of these systems.

Limits on the neutron EDM place constraints on CP violation primarily in the hadronic sector. In particular, the neutron EDM can arise from either the CP violating θ term in the QCD lagrangian, or directly from the chromoelectric dipole moments of the quarks (a chromoelectric dipole moment is similar to a regular EDM, though instead of interacting with an electromagnetic field it interacts with the color field).

Experiments in paramagnetic atoms with an unpaired electron directly yield information about the EDM of the electron. From a theoretical standpoint, the EDM of the electron

is an attractive quantity to work with because there are no QCD uncertainties involved in constraining the minimally supersymmetric standard model. In experiments with paramagnetic atoms, it is favorable to use heavy atoms because relativistic effects enhance the atomic EDM relative to the bare electron EDM and for thallium this enhancement factor is approximately 600. Paramagnetic atoms also receive an EDM contribution from a hypothetical CP violating electron-nucleon interaction which mixes states of opposite parity. Such an interaction is important in certain multi-Higgs theories.

Heavy polar molecules can also be used to perform a search for an electron EDM, and have the advantage that the internal electric field of the molecule can be quite large, on the order of 10^9 V/cm. Hence, a small externally applied electric field can be used to polarize the molecules, reducing systematic effects such as leakage currents, while the electrons feel a very large molecular electric field. Dave DeMille and coworkers are currently conducting such an experiment in lead oxide with an expected sensitivity on the order of $10^{-29} - 10^{-30}\, e$cm.[19]

Diamagnetic atoms are sensitive to a number of sources of CP violation. The biggest contribution to the EDM in diamagnetic atoms occurs in the hadronic sector from either the θ term in the QCD lagrangian or the chromo-electric dipole moments of the quarks. Falk *et al.* [20] recently pointed out that because of various computational and theoretical uncertainties, the extraction of limits on CP violating phases is more reliable in diamagnetic atoms than in the neutron. Like paramagnetic atoms, diamagnetic atoms also receive an EDM contribution from a semi-leptonic weak current. Finally, despite the fact that diamagnetic atoms have a closed electron shell, the bare EDM of an electron can also induce an atomic EDM by mixing states of opposite parity. This effect is fairly small since it occurs at 2nd order in perturbation theory, in conjunction with the magnetic field of the nucleus.

From the viewpoint of simply placing the tightest limit on the electric dipole moment of anything, experiments in diamagnetic atoms are attractive because the gyromagnetic ratios are roughly a factor of 2000 smaller than for paramagnetic atoms, and therefore, noise due to

magnetic field fluctuations is reduced considerably. Despite the greatly reduced sensitivity to the electron EDM, the spectacular sensitivity of the mercury experiment allows it to approach the limit of the more direct measurement in thallium[6].

1.4 Mechanisms generating an Atomic EDM

Atomic EDMs can be induced by several mechanisms[21]: **1**) A P, T odd electron-nucleon interaction. **2**) A P, T odd nuclear moment arising from either an EDM of a valence nucleon or a CP odd nucleon-nucleon interaction. **3**) Intrinsic EDM of an electron. There is an extensive body of literature on this subject, and hence I will only give a very brief review here, focussing on mechanisms specific to diamagnetic atoms. The reader is urged to consult Refs. [11] and [21] for a more complete reviews. After discussing these model independent mechanisms for generating an atomic EDM, we briefly discuss several of the more popular models of CP violation beyond the standard model.

1.4.1 Electron-Nucleon interaction

A CP violating interaction between the electrons and nucleons generates an atomic EDM by mixing states of opposite parity. In general there are three four-fermion operators that violate P and T, [11]

$$H = C_{SP}\frac{G_F}{\sqrt{2}}\bar{N}N\bar{e}i\gamma_5 e + C_T\frac{G_F}{\sqrt{2}}\frac{1}{2}\epsilon_{\mu\nu\kappa\lambda}\bar{N}\sigma_{\mu\nu}N\bar{e}\sigma_{\kappa\lambda}e + C_{PS}\frac{G_F}{\sqrt{2}}\bar{N}i\gamma_5 N\bar{e}e \tag{1.4}$$

where G_F is the Fermi constant. While Eq. 1.4 assumes the interaction is between a nucleon and an electron, the same form also applies to CP violating nucleon-nucleon interactions and we will address this latter contribution in the next section. The first term in Eq. 1.4 is a scalar-pseudoscalar interaction, the second is a tensor interaction and the third is a pseudoscalar-scalar interaction. In the approximation that the nucleus is infinitely massive, the pseudoscalar-scalar interaction does not contribute. For paramagnetic atoms with non-zero ground state electronic angular momentum, either of the scalar-pseudoscalar or tensor terms can mix states of opposite parity to induce an atomic EDM. For diamagnetic atoms

with zero electron angular momentum, the tensor term mixes states of opposite parity, directly inducing an atomic EDM. Using the Hartree-Fock method to calculate the atomic wavefunctions, Ref. [22] showed that the atomic EDM induced by the tensor term is

$$d_{\mathrm{Xe}} = C_T \times 5.2 \times 10^{-21}\, e\text{−cm} \tag{1.5}$$

$$d_{\mathrm{Hg}} = C_T \times 2.0 \times 10^{-20}\, e\text{−cm}. \tag{1.6}$$

The scalar-pseudoscalar term along with the hyperfine interaction generates an atomic EDM at second order in perturbation theory, reducing the sensitivity to this interaction in diamagnetic atoms. The result of the Hartree-Fock calculation of the induced atomic EDM is

$$d_{\mathrm{Xe}} = C_{SP} \times 5.6 \times 10^{-23}\, e\text{−cm} \tag{1.7}$$

$$d_{\mathrm{Hg}} = C_{SP} \times 5.9 \times 10^{-22}\, e\text{−cm}. \tag{1.8}$$

[21, 22] The current limit on the mercury EDM [3] sets the tightest constraints on these parameters $C_T < 1 \times 10^{-8}$ and $C_{SP} < 3 \times 10^{-7}$. Thus, the sensitivity of a measurement of the ^{129}Xe EDM must exceed the sensitivity of the ^{199}Hg measurement by a factor of 4 and 10 respectively to improve on the current limits of C_T and C_{SP} respectively. The effective interaction in Eq. 1.4 can be generated by the exchange of a Higgs boson in certain multi-Higgs models.

1.4.2 Hadronic CP violation

The best limits on CP violation in the hadronic sector can be derived from limits on diamagnetic atoms, and hence we will devote considerable attention to this problem. Unfortunately, to access the CP violating phases in physics beyond the standard model requires a complex series of calculations. Naively, one would expect that because the diamagnetic atoms of interest, ^{199}Hg and ^{129}Xe, have nuclear spin $I = 1/2$, an atomic EDM simply corresponds to the EDM of the nucleus. However this is not the case, as was first pointed out by Schiff.[27] Consider an atom with a nucleus of negligible size and a nonzero electric dipole moment

in an externally applied electric field. In a stationary state, the electrons must rearrange themselves so that the total electric field at the nucleus must be zero to prevent the nucleus from flying off into the middle of nowhere. Hence it is not possible to directly measure the electric dipole moment of the nucleus. Fortunately, finite size effects prevent complete shielding of the nucleus from the electric field. To illustrate, suppose a valence neutron had a nonzero electric dipole moment. The electric field is zero at the center of charge of the nucleus, however, the electric field need not be zero at the valence neutron. Taking into account the screening effects of the electrons, the first nonzero CP odd nuclear moment that can generate an atomic EDM is known as the Schiff moment, which is essentially a difference in the distribution of charge and electric dipole moment in the nucleus. We first discuss at some length the Schiff moment and its contribution to atomic EDMs and then address how the Schiff moment arises from the effective nucleon-nucleon interaction.

Schiff moment and atomic EDMs

The electrostatic potential produced by the nuclear charge density is [29]

$$\phi(\mathbf{R}) = \int \frac{e\rho(\mathbf{r})}{\mid \mathbf{R}-\mathbf{r} \mid} d^3\mathbf{r} + \frac{1}{Z}(\mathbf{d}\cdot\nabla)\int \frac{\rho(\mathbf{r})}{\mid \mathbf{R}-\mathbf{r} \mid} d^3\mathbf{r} \tag{1.9}$$

where $\rho(\mathbf{r})$ is the nuclear charge density, normalized so that $\int \rho(\mathbf{r}) d^3\mathbf{r} = Z$ and $\mathbf{d} = \int e\mathbf{r}\rho(\mathbf{r}) d^3\mathbf{r}$ is the electric dipole moment of the nucleus. The first term here is the usual electrostatic potential, the second is the result of screening by the electron cloud. There are several typographical errors in the derivation given by Spevak *et al.* [29]. To clarify, we go through a complete derivation here.

Ignoring spin-spin and spin-orbit coupling, the Hamiltonian of an atom in an externally applied electric field is

$$H = \sum_i [K_i - e\phi_0(\mathbf{R}_i) + e\mathbf{R}_i\cdot\mathbf{E}_0] + \sum_{j>k} \frac{e^2}{\mid \mathbf{R}_j - \mathbf{R}_k \mid} - \mathbf{d}\cdot\mathbf{E}_0 \tag{1.10}$$

where K_i and $\mathbf{R}_i$ are the kinetic energy and coordinate of the ith electron and

$$\phi_0(\mathbf{R}_i) = e\int \frac{\rho(\mathbf{r})}{\mid \mathbf{R}_i - \mathbf{r} \mid} d^3\mathbf{r} \tag{1.11}$$

is the usual electrostatic nuclear potential. The third term in brackets in Eq. 1.10 is the interaction $-\mathbf{p}_{el} \cdot \mathbf{H}$ of the electric dipole moment of the atomic electrons (note that we are not concerned with the intrinsic dipole moment of the electron here) with the applied electric field. Since the electron charge is negative $\mathbf{p}_{el} = -e\mathbf{R}_i$, yielding the correct sign in Eq. 1.10.

With insight from Spevak *et al.* we add to the Hamiltonian an auxiliary potential

$$V = \mathbf{d} \cdot \mathbf{E}_0 - \frac{1}{Z}\mathbf{d} \cdot \sum_i \nabla_i \phi_0(\mathbf{R}_i). \tag{1.12}$$

The addition of V to the Hamiltonian leaves the energy levels unchanged, because as we now show, $\langle V \rangle = 0$. First note that

$$\frac{i}{\hbar}\left[\sum_i \mathbf{p}_i, H\right] = -e\sum_i \nabla_i \phi_0(\mathbf{R}_i) + Ze\mathbf{E_0} \tag{1.13}$$

where we have used the well know relation $[\mathbf{p}_i, f(\mathbf{R})] = -i\hbar\nabla f(\mathbf{R})$ and the fact that, by symmetry the total momentum operator commutes with the electron interaction term. Also note that $\langle n \mid [\sum_i \mathbf{p}_i, H] \mid n\rangle = E_n\langle n \mid \sum_i \mathbf{p}_i \mid n\rangle - E_n\langle n \mid \sum_i \mathbf{p}_i \mid n\rangle = 0$, and hence, making use of Eq. 1.13

$$\left\langle \sum_i \nabla_i \phi_0(\mathbf{R}_i) \right\rangle = Z\mathbf{E}_0. \tag{1.14}$$

Finally, we arrive at

$$\langle V \rangle = \mathbf{d} \cdot \mathbf{E}_0 - \frac{1}{Z}\mathbf{d} \cdot Z\mathbf{E}_0 = 0. \tag{1.15}$$

Thus the addition of V to the Hamiltonian leaves the energy levels unchanged. The modified Hamiltonian is then

$$\tilde{H} = H + V = \sum_i [K_i - e\phi(\mathbf{R}_i) + e\mathbf{R}_i\mathbf{E}_0] + \sum_{j>k} \frac{e^2}{\mid \mathbf{R}_j - \mathbf{R}_k \mid} \tag{1.16}$$

where $\phi(\mathbf{R})$ is given by Eq. 1.9. Note that $\tilde{H}$ does not directly contain the interaction $\mathbf{d} \cdot \mathbf{E}_0$.

Focusing on the T, P odd terms in a multipole expansion of $\phi(\mathbf{R})$, we see that the dipole term of the first is cancelled by the monopole term of the second

$$-\int e\left(\mathbf{r}\nabla\frac{1}{R}\right)\rho(\mathbf{r})d^3\mathbf{r} + \frac{1}{Z}\mathbf{d} \cdot \nabla\frac{1}{R}\int \rho(\mathbf{r})d^3\mathbf{r} = 0. \tag{1.17}$$

The first nonzero T, P odd term can be written in terms of a vector $\mathbf{S}$ and a rank 3 tensor after separation of the trace

$$\begin{aligned} \phi^{(3)} &= \phi^{(3)}_{Schiff} + \phi^{(3)}_{octupole} \\ \phi^{(3)}_{Schiff} &= 4\pi \mathbf{S} \nabla \delta(R) \\ \phi^{(3)}_{octupole} &= -\frac{1}{6} Q_{\alpha\beta\gamma} \nabla_\alpha \nabla_\beta \nabla_\gamma \frac{1}{R} \end{aligned} \tag{1.18}$$

where

$$\mathbf{S} = \frac{1}{10}\left(\int e\rho(\mathbf{r}) r^2 d^3\mathbf{r} - \frac{5}{3}\mathbf{d}\frac{1}{Z}\int \rho(\mathbf{r}) r^2 d^3\mathbf{r} \right) \tag{1.19}$$

is the Schiff moment and $Q_{\alpha\beta\gamma}$ is the electric octupole moment. Note that here we adopt the convention used by Flambaum, Dzuba and coworkers with a factor of 4π appearing explicitly in the definition of ϕ_{Schiff}. Some other authors absorb this in the definition of the Schiff moment. The Schiff moment can be thought of as a charge distribution that produces a constant electric field inside the nucleus.[30] When electrons penetrate the nucleus, states of opposite parity are mixed, generating an atomic EDM. Recently there has been some interest in the nuclear electric octupole moment for its potential to enhance the nuclear Schiff moment [29, 31, 32], in heavier nuclei such as ^{223,225}Ra or ^{223}Rn. In Ref. [32] the enhancement factor is estimated to be on the order of $10^2 - 10^3$ compared to ^{199}Hg or ^{129}Xe.

The electric dipole moment of the atom is

$$D_z = -e\langle \tilde{\psi} \mid r_z \mid \tilde{\psi} \rangle \tag{1.20}$$

where $\tilde{\psi}$ is the atomic wave function perturbed by the potential 1.18

$$\mid \tilde{\psi} \rangle = \mid k_1 \rangle + \sum_{k_2} \frac{\mid k_2 \rangle \langle k_1 \mid \phi^{(3)} \mid k_2 \rangle}{E_{k_1} - E_{k_2}}. \tag{1.21}$$

Here $\mid k_1 \rangle$ is the unperturbed atomic ground state and $\{\mid k_2 \rangle\}$ is the set of opposite parity states. Thus, to lowest order

$$D_z = -2e \sum_{k_2} \frac{\langle k_1 \mid r_z \mid k_2 \rangle \langle k_1 \mid -e\phi^{(3)} \mid k_2 \rangle}{E_{k_1} - E_{k_2}}. \tag{1.22}$$

The nuclear electric octupole cannot directly generate an atomic EDM because of simple selection rules. The triangle rule for addition of angular momenta dictates that $\langle k_1 \mid r_z \mid k_2 \rangle$

Atom	EDM (units are $10^{-17}[S/e\text{-fm}^3]$e cm)
Xe	0.38
Rn	3.3
Hg	-2.8
Ra	-8.5
Pu	-11

Table 1.2: Values of atomic EDMs induced by the nuclear Schiff moment for a variety of atoms. From Ref. [34]

or $\langle k_1 \mid \phi^{(3)}_{Schiff} \mid k_2\rangle$ can only have nonzero values if $\mid J_1 - J_2 \mid \leq 1 \leq J_1 + J_2$ while $\langle k_1 \mid \phi^{(3)}_{octupole} \mid k_2\rangle$ can be nonzero if $\mid J_1 - J_2 \mid \leq 3 \leq J_1 + J_2$. Hence only the p-orbitals get mixed with the $J = 0$ ground state by the Schiff moment, and the octupole moment cannot contribute to mixing of the $J = 0$ state with any other states. A similar argument holds for the T, P violating magnetic quadrupole moment, preventing it from contributing to an atomic electric dipole moment.

Dzuba *et. al.* [34] carried out a series of detailed Hartree-Fock calculations to evaluate Eq. 1.22 for a variety of atoms. The results are summarized in Table 1.2. Generally the heavier atoms have larger electric dipole moments because relativistic effects enhance the wavefunction near the origin.

From the Schiff moment to nucleon-nucleon interactions

The Schiff moment can be generated by either an intrinsic dipole moment of a valence nucleon or by CP odd interactions between nucleons. It was shown by Sushkov *et al.* [33] that the contribution to the Schiff moment from the nucleon-nucleon interaction is approximately a factor of 60 larger than the contribution from a valence nucleon and hence we focus on the nucleon-nucleon interaction.

In the non-relativistic limit the potential between nucleons can be treated as a contact interaction [33]

$$\begin{aligned} W &= \frac{G}{\sqrt{2}}\frac{1}{2m_p}(\eta_{ab}\sigma_a - \eta_{ba}\sigma_b \cdot \nabla_a \delta^3(\mathbf{r}_a - \mathbf{r}_b) \\ &\quad + \eta'_{ab}[\sigma_a \times \sigma_b]\{(\mathbf{p}_a - \mathbf{p}_b), \delta^3(\mathbf{r}_a - \mathbf{r}_b)\}). \end{aligned} \tag{1.23}$$

^{129}Xe	^{131}Xe	^{199}Hg	^{201}Hg	^{203,205}Tl
$1.75\eta_{np}$	$-2.6\eta_{np}$	$-1.4\eta_{np}$	$2.4\eta_{np}$	$1.2\eta_{pp} - 1.4\eta_{pn}$

Table 1.3: Values of the nuclear Schiff moment $S/(e{-}\mathrm{fm}^3)\times 10^8$ induced by CP odd nucleon-nucleon coupling. These calculations were reported in Ref. [35] and used the nuclear shell model and Woods-Saxon potential.

Here m_p is the mass of the proton. The above potential generates T, P odd nuclear moments in the usual fashion, mixing states of opposite parity with the nuclear ground state. Flambaum *et al.* [35] report the results of calculations of the nuclear Schiff moment induced by the interaction 1.23 in the nuclear shell model using wavefunctions and Greens functions for the standard Woods-Saxon potential $U(r) = \frac{-V}{1+\exp{(r-R)/a}}$ where $V = 52$ MeV, $R = 1.25A^{1/3}$ fm is the nuclear radius and $a = 0.52$ fm is the distance over which the nuclear density falls off. Contributions to the Schiff moment from virtual excitations of paired nucleons are comparable to the contribution from excited states of the valence nucleon. The results of these calculations are summarized in Table 1.3. The first four atoms are primarily sensitive to η_{np} because the valence nucleon is a neutron and generates excitations of the internal protons. From the values in Tables 1.2 and 1.3 we see that to improve on limits of CP violation in the hadronic sector, the sensitivity of an experiment in xenon must exceed that of mercury by a factor of approximately 6.

The potential in Eq. 1.23 is an effective interaction that is dominated by the exchange of a pion because it is the lightest of the mesons, generating the longest range interactions. The effective interaction constant η_{np} written in terms of the CP violating nucleon-pion coupling constant $\bar{g}_{\pi NN}$ is

$$\eta_{np} = \frac{\sqrt{2}}{G_F}\frac{\bar{g}_{\pi NN} g}{m_\pi^2} \tag{1.24}$$

where g is the strong coupling constant and m_π is the pion mass. The CP odd coupling constant $\bar{g}_{\pi NN}$ can arise from either a CP odd term in the QCD lagrangian or from the chromo-electric dipole moments of the quarks that appear in supersymmetric theories. We will briefly address both of these contributions shortly.

1.4.3 Electron EDM

An atomic EDM in diamagnetic atoms can also be generated by the intrinsic EDM of the electron, despite the fact that these atoms zero electronic angular momentum. Two effects lead to a contribution from the electron EDM to the atomic EDM in high order perturbation theory: the interaction of the electron EDM with the magnetic field of the nucleus and the interaction of the electron EDM with the coulomb field of the nucleus in conjunction with the hyperfine interaction.[11] A detailed Hartree-Fock calculation [26] reports that an electron EDM would induce an atomic EDM in xenon $d_{Xe} = -0.8 \times 10^{-3} d_e$. Hence, to improve on the electron EDM measurement performed in thallium and reported in Ref. [6], a measurement in xenon will require a sensitivity at the level of $\sim 10^{-30}\, e$-cm.

1.4.4 Models of CP violation

Our discussion up till now has focused on model independent parameters that are valid for any model of CP violation. A detailed discussion of possible CP violating extensions to the standard model is beyond the scope of this work, so we will briefly survey several of the more popular theories. A more thorough review can be found in Ref. [23].

Strong CP problem

In quantum chromodynamics, there is a CP violating term in the Lagrangian

$$L_\theta = -\theta_{QCD} \frac{\alpha_s}{8\pi} \tilde{G}^a_{\mu\nu} G^a_{\mu\nu}. \tag{1.25}$$

This interaction gives rise to the CP odd pion-nucleon coupling. In Ref. [36] it was shown that $\bar{g}_{\pi NN} \approx -0.027\theta_{QCD}$. The limit on the mercury EDM [3] currently sets the tightest constraints on this phase, $\theta_{QCD} < 1.5 \times 10^{-10}$.

The smallness of this parameter is of great concern to theorists when *a priori* it is of order unity. One possible solution to this problem is the introduction of the Peccei-Quinn symmetry [37], named after its authors, which would render the θ_{QCD} term harmless. The breaking of the PQ symmetry introduces a new, near massless pseudoscalar particle known

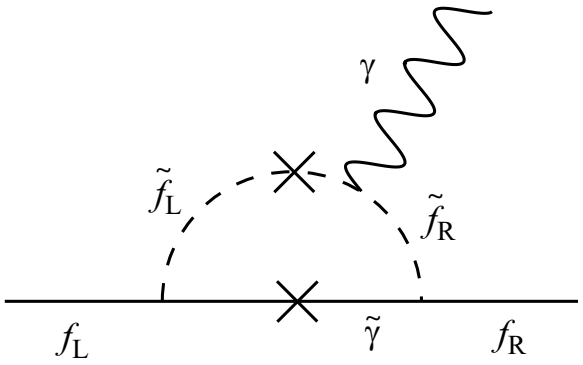

Figure 1.2: Generic contribution to the EDM of fermions in the minimally supersymmetric standard model.[23]

as the axion.[38, 39] Thus far there has been no experimental evidence for the existence of the axion.

Minimally supersymmetric standard model

The CP odd nucleon-nucleon coupling constant arises in the MSSM due to non-zero quark chromo-EDMs, resulting in [20]

$$\eta_{np} = \frac{1}{4\pi G_F}\frac{3g_{\pi pp}m_0^2}{f_\pi m_\pi^2}(\tilde{d_d} - \tilde{d_u} - 0.012\tilde{d_s}) \tag{1.26}$$

where $g_{\pi pp}$ is the CP conserving vertex in the exchange of the pion and f_π is the pion form factor. Note that this differs by a factor of 4π from the expression derived in Ref. [20] because those authors absorb a factor of 4π into the definition of the Schiff moment. The mercury EDM measurement [3] sets a limit

$$e \mid \tilde{d_d} - \tilde{d_u} - 0.012\tilde{d_s} \mid < 7 \times 10^{-27} e\text{cm} \tag{1.27}$$

EDMs of fermions arise from the exchange of a supersymmetric partner at the one loop level, as shown in Fig. 1.2 The chromo-EDMs of quarks couple to the color field rather than the electromagnetic, so the external photon line is replaced with a gluon. In the MSSM, there are two phases that arise in the breaking of supersymmetry, θ_A and θ_μ.[20] Diagrams such as that shown in Fig. 1.2 lead to chromo-EDMs of the form

$$\tilde{d_q} \propto \frac{m_q}{M_{SUSY}^2}\sin\phi. \tag{1.28}$$

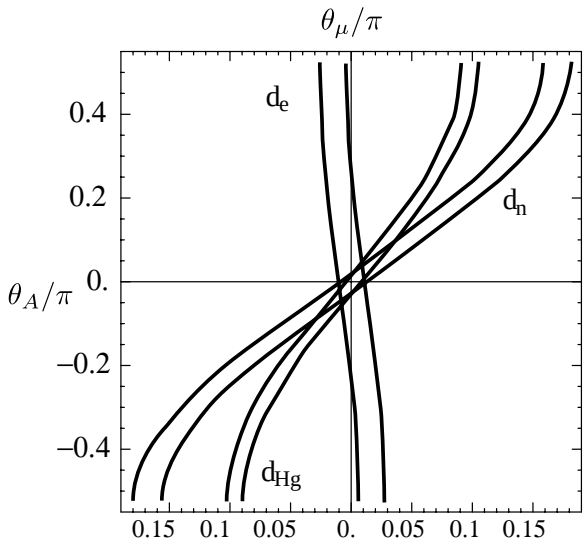

Figure 1.3: Limits on the two CP violating phases in the MSSM, assuming a supersymmetric mass scale of 500GeV. Calculations performed by Maxim Pospelov, updated from work published in Ref [20] to include the recent limits on the mercury EDM.

Limits on $d(^{199}\mathrm{Hg})$, d_e and d_n place severe constraints on the two phases θ_A and θ_μ. Fig. 1.3 shows calculations, updated by Maxim Pospelov from Ref [20], to include the most recent results in mercury assuming a supersymmetric mass scale of 500 GeV. We see that for this scale, the phases must be constrained to $O(10^{-2})$, requiring significant fine tuning, when *a priori* these phases are of order unity. To reconcile SUSY with existing EDM limits requires a great deal of fine tuning of the phases, or an increase of the supersymmetric masses. However, increasing the mass of the supersymmetric partners much beyond the TeV level makes SUSY less viable as a mechanism for suppressing the gauge hierarchy problem discussed earlier. Another possible solution recently considered is the suppression of electric dipole moments due to cancellation between various contributions.[41] Taking into account of only the constraints from the neutron and electron allow cancellations in certain regions of parameter space, however when the results of mercury are taken into account this idea has been largely disproved by the work of Falk *et al.*

1.5 Why liquid Xe?

Given that ^{129}Xe is less sensitive to CP violating interactions than ^{199}Hg, why is it desirable to perform a search for an EDM in the former system? For N uncorrelated atoms, the fundamental limit to the precision with which one can measure the precession frequency is

$$\delta\omega = 1/\sqrt{NT_2\tau} \tag{1.29}$$

where τ is the total measurement time, assumed to be long compared to the transverse relaxtion time T_2. Beyond this limit, quantum fluctuations will influence the outcome of a measurement. Thus, assuming that the spins can be measured very efficiently, a figure of merit for an EDM experiment is

$$\delta d = \frac{\hbar}{4E\sqrt{NT_2\tau}} \tag{1.30}$$

where E is the electric field strength, T_2 is the transverse relaxation time and τ is the measurement time. Liquid xenon has a high electric field breakdown strength ($\sim$ 400 kV/cm)[44], large number density ($\sim 10^{22}$ cm^{-3}), and a long transverse relaxation time $\sim$ 1300 s (our measurements of T_2 are discussed below), dominated by the spin rotation interaction [45, 46] making it a near ideal medium in which to search for an EDM. Inserting these numbers into Eq. 1.30 we see that spin-projection noise limits a measurement of an EDM in this system to $\approx 10^{-36}$ e cm for one day of integration, far beyond any current experimental limit on EDMs.

While the shot noise limit is a useful figure of merit for determining the best possible performance of an experiment, it is not really representative of the expected sensitivity. Issues such as magnetic field noise and the sensitivity of the detection system will limit the performance well before quantum fluctuations. Large quantities of hyperpolarized xenon can be readily produced using the method of spin exchange optical pumping (see below and Ref. [47]), creating large magnetic fields that can be efficiently detected with SQUID magnetometers. The magnetic field from a 1 cm diameter sphere filled with 5% polarized xenon in natural abundance a distance 1.5 cm from the center of the cell is about 200 μG. Commercially available low T_c SQUID magnetometers can achieve a sensitivities at the

level of $2 \times 10^{-5}\,\mu\mathrm{G}/\sqrt{\mathrm{Hz}}$, yielding signal to noise ratio $SNR = 10^7\,\sqrt{\mathrm{Hz}}$. Assuming that a measurement of the spins is made for the duration of their coherence time T_2, and then repeated for a total measurement time τ, the precession frequency can be determined with an accuracy

$$\delta\nu = \frac{1}{T_2 SNR\sqrt{\tau}}. \tag{1.31}$$

Thus, neglecting other sources of noise such as drifts in the ambient magnetic fields, in principle it is possible resolve frequency shifts at the level of $\delta\nu = 2.6 \times 10^{-13}$ Hz in one day of integration. Relating electric dipole moments to frequency shifts via Eq. 1.2 we find

$$\delta d = \frac{h\delta\nu}{2E} = 2.6 \times 10^{-32}\,e\,\mathrm{cm}. \tag{1.32}$$

Hence, despite the slightly reduced sensitivity to sources of CP violation, it is expected that the improved precision will set new limits on CP violating parameters. This simple analysis ignores many practical issues such as the magnetic field noise created by the magnetic shields and more importantly non-linear effects due to long range dipolar interactions.

It should be noted that there have been several prior EDM experiments in xenon. The first, performed at the University of Washington [43] used an optically pumped rubidium vapor to detect the precession of the xenon atoms and set a limit on $d_{\mathrm{Xe}} = (-0.3 \pm 1.1) \times 10^{-26}\,e{-}\mathrm{cm}$. The second, performed at the University of Michigan, set a new limit $d_{\mathrm{Xe}} = (-0.7 \pm 3.3(\mathrm{stat}) \pm 0.1(\mathrm{sys})) \times 10^{-27}\,e{-}\mathrm{cm}$ using a spin exchange pumped ^{3}He and ^{129}Xe comagnetometer.[4].

1.6 Spin-exchange optical pumping

To achieve the high nuclear polarization mentioned in the previous section, we use the standard method of spin exchange optical pumping, where angular momentum is transferred from an optically pumped alkali vapor to the nuclei of a noble gas via spin-exchange collisions. Hyperpolarized noble gases produced in this fashion have found a wide range of applications, from studies of the neutron structure function [48], medical imaging of lungs[49], to a variety of other tests of fundamental symmetries [50, 51, 52]. The physics

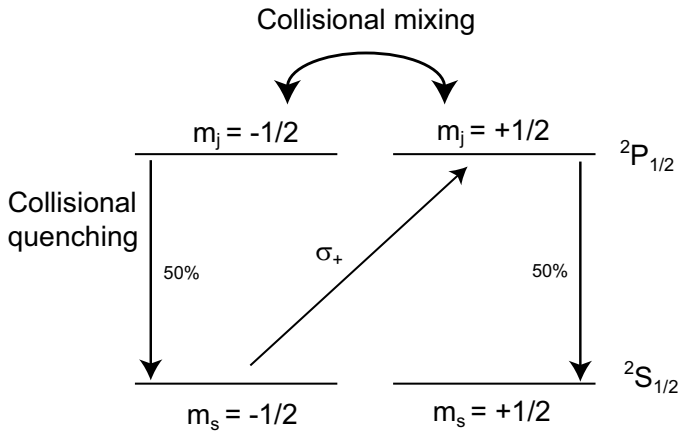

Figure 1.4: Optical pumping of the ground state of an alkali metal atomic vapor.

involved in this process has been discussed in detail in the literature, so I will merely give a brief overview. A more complete review may be found in Ref. [53].

Optical pumping of the alkali vapor is accomplished by illuminating the cell with circularly polarized light tuned to the wavelength of a transition from the ground state to an excited state of the alkali atom. As illustrated in Fig. 1.4, selection rules dictate that only transitions with $\Delta m = +1$ are allowed for right circularly polarized light [54]. Because high power lasers are commercially available in the region around the 794.7 nm D1 transition of Rb, Rb is a common choice for many spin exchange optical pumping experiments.

If an atom in the excited state were to make a transition to the ground state by emitting a photon, the stray photon could be absorbed by an atom already in the optically pumped state, a problem known as radiation trapping. [55] To avoid this problem, a small amount of N_2 is generally included in the gas mixture to collisionally quench the excited state. For the production of large amounts of polarized xenon, as in our application, it is typical to include a high pressure buffer gas such as ^{4}He or N_2 to pressure broaden the absorption line, facilitating the absorption of the broadband emission spectrum of high power diode lasers. Given these conditions, absorption of the circularly polarized light optically pumps one of the ground state zeeman sublevels, as in Fig. 1.4.

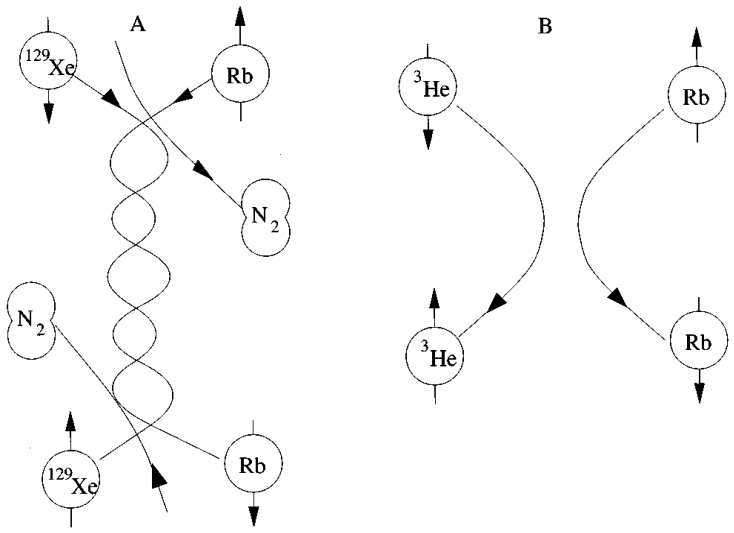

Figure 1.5: Processes through which spin angular momentum is transferred from alkali metal atoms to noble gas nuclei (Figure adopted from Ref [53]). A) Spin exchange through formation of a van der Walls molecule by interacting with a third body. Third body need not necessarily be N_2. B) Binary spin exchange, dominant for the high pressure conditions suitable for high volume production of polarized xenon gas.

The mean photon absorption rate per atom is

$$\langle \delta\Gamma \rangle = (1 - 2\langle S_z \rangle) R_p \tag{1.33}$$

where R_p is the absorption rate and depends on the spectral profile of the light and the line shape of the atomic transition. Assuming that there is rapid collisional mixing between the excited state Zeeman sublevels, on average, each atom has -1/2 unit of angular momentum before pumping and 0 units of angular momentum afterwards, as illustrated in Fig. 1.4. Hence the total angular momentum of the atom grows as

$$\frac{d\langle F_z \rangle}{dt} = R_p(1/2 - \langle S_z \rangle). \tag{1.34}$$

Spin exchange between the alkali-metal vapor and the noble-gas atom during a collision can be described by the perturbation,

$$V_1(\mathbf{R}) = \gamma(R)\mathbf{N} \cdot \mathbf{S} + A_b(R)\mathbf{I}_b \cdot \mathbf{S} \tag{1.35}$$

where $\mathbf{R}$ is the internuclear separation. The first term, called the spin-orbit or spin-rotation interaction, causes relaxation due to exchange of alkali metal electron spin $\mathbf{S}$ with relative orbital angular momentum $\mathbf{N}$ between alkali and noble gas atoms. The second term is responsible for exchange of angular momentum between alkali electron spin and noble gas nuclear spin $\mathbf{I}_b$. As illustrated in Fig. 1.5, there are two mechanisms that can generate spin exchange between alkali-metal and noble-gas atoms: binary collisions and the formation of van der Walls molecules via the interaction with a third body. However, at high pressures suitable for absorbing intense, broadband, circularly polarized laser light, the contribution to spin exchange through formation of van der Walls molecules is suppressed due to rapid break up of the molecules with buffer gas atoms [56]. Spin-exchange and relaxation rates $\Gamma = n\sigma\bar{v}$ can be calculated from first order time-dependent perturbation theory, where n is the alkali number density, σ is the cross section and $\bar{v}$ is the average thermal velocity of the atoms.[57] The results of these calculations are summarized in Fig. 1.6.

Assuming an alkali-metal spin temperature distribution [60] and noble gas nuclear spin of 1/2 as in ^{3}He or ^{129}Xe the evolution of angular momentum as a result of collisions can be described by

$$\frac{d\langle F_z\rangle}{dt} = -\Gamma_a(\gamma)\langle S_z\rangle - \Gamma_a(A_b)[\langle S_z\rangle - \langle I_{bz}\rangle] \tag{1.36}$$

$$\frac{d\langle I_{bz}\rangle}{dt} = \Gamma_b(A_b)[\langle S_z\rangle - \langle I_{bz}\rangle] - \bar{\Gamma}\langle I_{bz}\rangle \tag{1.37}$$

where the alkali-metal spin relaxation rate is $\Gamma_a(\gamma) = [A]\bar{v}\sigma_{SD}$, the spin exchange rate is $\Gamma_b(A_b) = [A]\bar{v}\sigma_{SE}$. $\bar{\Gamma}$ is the noble gas spin relaxation rate which includes relaxation due to spin conserving and nonconserving collisions with the alkali-metal vapor as well as other sources of relaxation such as collisions with the cell walls.

For noble gas atoms with nuclear spin $I_b = 1/2$, the efficiency of the transfer of photonic angular momentum to nuclear spin is given by [61]

$$\eta = \frac{\Gamma_a(A_b)}{2(\bar{\Gamma} + \Gamma_a(A_b))} \tag{1.38}$$

where $\bar{\Gamma}$ represents the sum of all alkali metal relaxation processes. Based on the values of cross sections given in Fig. 1.6, the efficiency ranges from $\eta = 0.04$ for Rb-Xe to $\eta = 0.38$

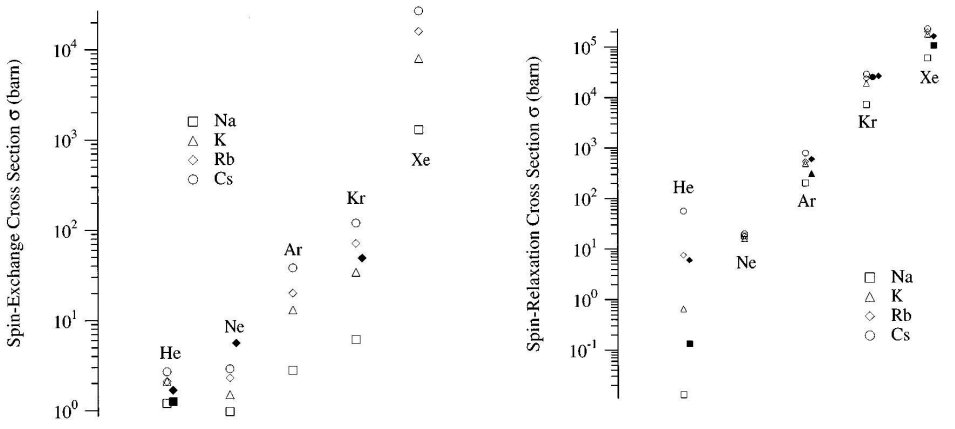

Figure 1.6: Summary of spin-exchange and spin-destruction cross sections for alkali-metal noble-gas atom collisions, figure adopted from Ref. [53].

for K-He.

1.7 SQUID magnetometers

Until the recent development of spin-exchange relaxation free atomic magnetometry[62], SQUID magnetometers have been unparalleled in sensitivity to small magnetic fields. In conventional NMR experiments, the signal is proportional to B^2, where one power of B comes from the fact that the polarization is proportional to the magnetic field, and the second comes from the fact that for inductive detection, the signal is proportional to the time derivative of the flux through the pickup coil. SQUID magnetometers, in contrast, are sensitive to the flux Φ through a pickup loop, rather than $d\Phi/dt$, eliminating the latter penalty associated with low field NMR (using hyperpolarized xenon eliminates the former penalty). Typical low T_c SQUID magnetometers achieve sensitivities on the order of $1 - 2 \times 10^{-5}\,\mu\mathrm{G}/\sqrt{\mathrm{Hz}}$. High T_c SQUIDs are about an order of magnitude less sensitive. For the work discussed here, we use two high T_c SQUID magnetometers manufactured by Tristan Technologies.

A schematic of a typical SQUID magnetometer is shown in Fig. 1.7 a). The flux through a superconducting loop is conserved, regardless of a change in the external field. Hence a

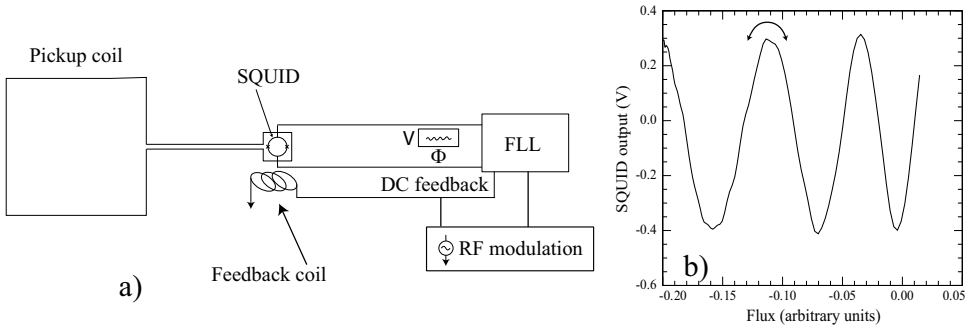

Figure 1.7: a) Schematic of a SQUID magnetometer, showing SQUID, pickup coil, feedback/modulation coil and flux locked loop. b) Voltage across SQUID loop as a function of flux. b)

change in the external field cutting the pickup coil induces a supercurrent to flow through the pickup and input coil, which is inductively coupled to the SQUID loop. In an idealized SQUID, the critical current through the Josephson junctions is an oscillating function of the flux through the SQUID loop. In practical devices, the SQUID loop is biased with a small DC current, in which case the voltage across the loop is an approximately sinusoidal function of the flux through the loop with period of one flux quantum $\Phi_0 = hc/2e$, as shown Fig. 1.7b). To achieve a linear response to the magnetic field, most DC SQUID magnetometers operate in feedback mode. A small RF current is driven through the feedback coil located on top of the SQUID loop, inducing a small RF flux in the SQUID loop. A flux locked loop monitors the first harmonic of this signal to detect a peak on the flux vs voltage curve. To remain locked to the same peak, the flux locked loop sends a small dc current through the coil, thereby keeping the total flux through the SQUID loop constant, regardless of changes in the external field. A change in the magnetic field is then directly proportional to the feedback current. For a comprehensive review of SQUIDs and their applications, see Refs. [63, 64].

1.8 Measurement of the transverse relaxation time

In preparation for a search for an electric dipole moment, the first thing we did was to measure the transverse relaxation time of liquid xenon. These measurements were published

in Ref. [73] and I only briefly discuss them here. The longitudinal spin relaxation time T_1 of liquid ^{129}Xe was investigated in work reported in Refs. [46, 65]; at 180 K it is about 30 min. Spin relaxation in liquid ^{129}Xe is dominated by spin-rotation interactions and an estimate of T_1 from the chemical shift of ^{129}Xe [45] is in good agreement with the experiment. In a liquid one would expect that the correlation time τ_c of the spin-rotation interaction would be very short, and in the regime of motional narrowing ($\omega \ll 1/\tau_c$) T_2 should be equal to T_1. However, existence of long-lived Xe Van der Waals molecules [66, 67] could result in shorter values of T_2. In previous studies of the transverse relaxation in liquid ^{129}Xe [68, 69] measured values of T_2 were no longer than several seconds. During the course of our investigations, we realized that a thorough understanding of long range dipolar interactions would be crucial to performing an EDM search in liquid xenon.

Our measurements were performed using ^{129}Xe polarized by spin-exchange optical pumping [47]. A schematic of the apparatus is shown in Figure 1.8. A mixture of 2% Xe (in natural abundance), 2% N_2, and 96% ^{4}He flowed at a pressure of 3 atm through an optical pumping cell containing Rb vapor at 155°C. The Rb was optically pumped by a 40 W diode laser array whose spectrum was narrowed using an etalon.[70] Polarized ^{129}Xe gas froze out of the mixture as it passed through a cold trap (77 K) in a magnetic field of 1.5 kG, where it had a longitudinal spin relaxation time of several hours. After 40 min of accumulation, approximately 7 g of Xe ice was collected in the cold trap. The trap was then warmed and Xe gas flowed through glass tubing to a 1.3 cm dia. spherical glass cell, where it liquefied at a temperature of 180 K maintained by a mixture of acetone ice and liquid.

The NMR measurements were performed in a magnetic field of 32 G ($\omega = 2\pi \times 37.5$ kHz). To eliminate radiation damping effects the NMR coil was connected to a high impedance amplifier without using a resonant circuit. The gradients of the external magnetic field were reduced to about 0.1 mG/cm by first-order gradient coils, so that the free induction decay time due to dephasing of the spins was $T_2^* = 2 - 3$ sec. The timing of the RF pulses was controlled by an NMR pulser PC card [71], while the phases of the pulses were set with high precision using a DSP function generator that was controlled through serial interface

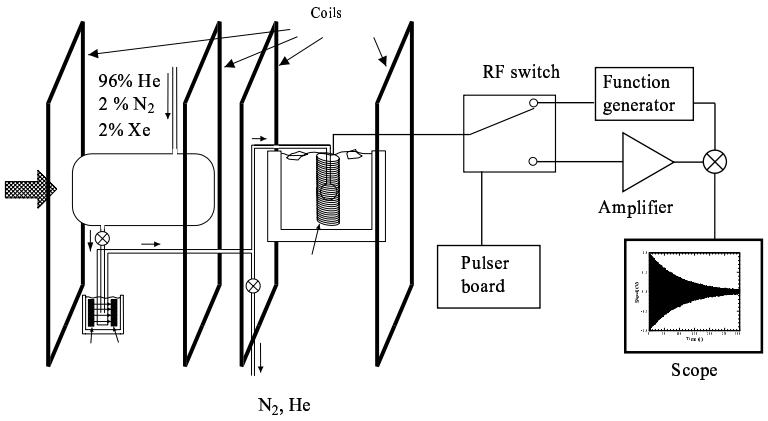

Figure 1.8: Schematic of the apparatus used to produce large quantities of hyperpolarized liquid xenon and the NMR spectrometer used to measure T_2 with the method of spin echoes. The coils used to produce a 32 G field were arranged so that there were two regions of uniform magnetic field.

commands also generated by the pulser card. Our measurements of T_1 were in agreement with those reported in Ref. [65].

To suppress spin dephasing due to residual external magnetic field gradients we used a standard CPMG spin-echo pulse sequence [72]. It consisted of a $\pi/2$ pulse followed by a train of π pulses at times τ , 3τ, 5τ, ... whose phases were shifted by 90° from the phase of the $\pi/2$ pulse. The duration of the π pulses was about 1 msec. Typical values of τ were 30 to 100 msec, much shorter than T_2^*. The decay of the magnetization due to spin diffusion between π pulses was negligible.

The spin-echo technique does not prevent spin dephasing due to gradients created by the dipolar fields, since these gradients are reversed by π pulses together with the magnetization. For a uniform ^{129}Xe polarization in a spherical cell the dipolar field seen by ^{129}Xe atoms adds up to zero. However, in the presence of a small gradient of the external magnetic field the magnetization of ^{129}Xe will develop a helix which in turn produces a gradient of the magnetic field, resulting in exponential growth of the magnetization gradients for a $\pi/2$ pulse. When the gradients of the magnetization become large enough, the decay of the average transverse magnetization becomes highly non-exponential as shown by the solid circles in Figure 1.9.

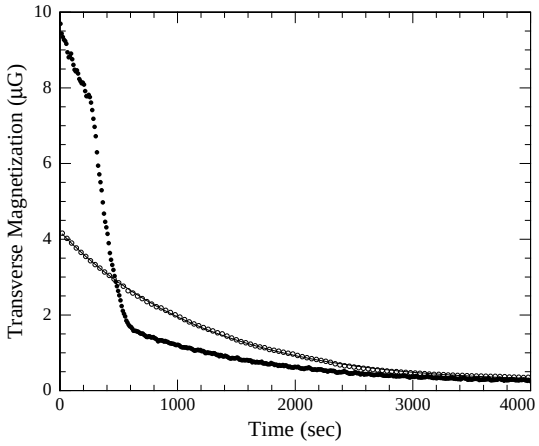

Figure 1.9: Spin-echo envelope for CPMG sequence with $\tau = 100$ msec, $dH_{Ez}/dx = 1.4$ mG/cm and the π pulse intentionally shortened by 3% (solid circles); with $\tau = 30$ msec and gradients reduced to about 0.1 mG/cm (open circles). An exponential fit to the latter gives $T_2 = 1290\,\mathrm{sec}$ (solid line). Fits to the initial and final decay of the data shown with solid circles also give similar values of T_2.

Figure 1.9 also shows the spin-echo envelope for a CPMG sequence with a smaller M_0 and a shorter π pulse spacing τ. In this case the transverse magnetization decayed exponentially, with a time constant $T_2 = 1290\,\mathrm{sec}$. Lower magnetization reduces the strength of the dipolar interactions and the shorter spacing between π pulses can suppress the instability due to dipolar interactions by causing a slow rotation around the x axis in the rotating frame. This effect is discussed further in Ref. [73]. In other data sets we obtained values of T_2 up to 1360 sec. Most systematic effects would decrease the value of T_2 and we cannot exclude the possibility of an additional relaxation rate on the order of $1/T_2 - 1/T_1 = 2 \times 10^{-4}\ \mathrm{sec}^{-1}$. For example, it could be due to partial transverse spin relaxation on the walls of the cell. Note that if the walls of the cell were completely depolarizing, it would give a diffusion-limited relaxation rate of $1 \times 10^{-3}\ \mathrm{sec}^{-1}$. Thus, our data are also consistent with intrinsic T_2 for liquid ^{129}Xe equal to $T_1 = 1800\,\mathrm{sec}$.

1.9 Dynamical instabilities and spin precession

Observation of spin-precession signals forms the basis of such prevalent experimental techniques as NMR and EPR. It is also used in searches for physics beyond the standard model [3, 6, 51, 74] and sensitive magnetometery [62]. Hence, there is significant interest in the development of general techniques for increasing the sensitivity of spin-precession measurements. Several methods for reducing spin-projection noise using quantum nondemolition measurements have been explored [75, 76], and it has been shown that in some cases they can lead to improvements in sensitivity [77, 78]. Here we demonstrate a different technique that increases the sensitivity by amplifying the spin-precession signal rather than reducing the noise. The amplification technique is based on the exponential growth of the spin-precession angle in systems with a dynamic instability caused by collective spin interactions. Such instabilities can be caused by a variety of interactions, such as, dipolar magnetic fields in a nuclear-spin-polarized liquid as discussed here, or electron-spin-polarized gas [79], spin-exchange collisions in an alkali-metal vapor [80], or mixtures of alkali-metal and noble-gas atoms [50]. This amplification technique can be used in a search for a permanent electric dipole moment in liquid ^{129}Xe. It is also likely to find applications in a variety of other systems with strong dipolar interactions, such as cold atomic gases [81] and polar molecules[82].

Consider first an ensemble of noninteracting spins with a gyromagnetic ratio γ initially polarized in the x direction and precessing in a small magnetic field B_z . The spin-precession signal

$$\langle Sy\rangle = \gamma\langle S_x\rangle B_z t \tag{1.39}$$

grows linearly in time for $\gamma B_z t \ll 1$. The measurement time t_m is usually limited by spin-relaxation processes and determines, together with the precision of spin measurements $\delta\langle S_y\rangle$, the sensitivity to the magnetic field

$$\delta B_z = \frac{\delta\langle S_y\rangle}{\gamma\langle S_x\rangle t_m} \tag{1.40}$$

or any other interaction coupling to the spins.

In the presence of a dynamic instability, the initial spin precession away from a point of unstable equilibrium can be generally written as $\langle S_y \rangle = \langle S_x \rangle B_z \sinh \beta t$, where β is a growth rate characterizing the strength of spin interactions. The measurement uncertainty is now given by

$$\delta B_z = \frac{\delta \langle S_y \rangle}{\langle S_x \rangle \sinh \beta t_m}. \tag{1.41}$$

Hence, for the same uncertainty in the measurement of $\delta \langle S_y \rangle$, the sensitivity to B_z is improved by a factor of $G = \sinh(\beta t_m)/(\beta t_m)$. It will be shown that quantum (as well as nonquantum) fluctuations of $\langle S_y \rangle$ are also amplified, so this technique cannot be used to increase the sensitivity in measurements limited by the spin-projection noise. However, the majority of experiments are not limited by quantum fluctuations. For a small number of spins the detector sensitivity is usually insufficient to measure the spin-projection noise of $N^{1/2}$ spins, while for a large number of particles the dynamic range of the measurement system is often insufficient to measure a signal with a fractional uncertainty of $N^{-1/2}$. Amplifying the spin-precession signal before detection reduces the requirements for both the sensitivity and the dynamic range of the measurement system. Optical methods allow efficient detection of electron spins and some nuclear spins [3] in atoms or molecules with convenient optical transitions. However, for the majority of nuclei, optical detection methods are not practical and magnetic detection, using, for example, magnetic resonance force microscopy, has not yet reached the sensitivity where it is limited by the spin-projection noise [83, 84]. Therefore, nonlinear amplification can lead to particularly large improvements in precision measurements relying on nuclear spin precession.

Here we use long-range magnetic dipolar interactions between nuclear spins that lead to exponential amplification of spin precession due to a magnetic field gradient. It has also been shown that long-range dipolar fields in conjunction with radiation damping due to coupling with an NMR coil lead to an increased sensitivity to initial conditions and chaos [85]. To amplify a small spin-precession signal above detector noise it is important that the dynamic instability involves only spin interactions since instabilities caused by the feedback from the detection system would couple the detector noise, such as the Johnson noise of

the NMR coil, back to the spins. We measure spin precession using SQUID magnetometers that do not have a significant backreaction on the spins and show that under well controlled experimental conditions the dynamic instability due to collective spin interactions can be used to amplify small spin-precession signals in a predictable way.

1.10 Dipolar interactions

Most experimental work on dipolar interactions has been carried out in liquids using the conventional NMR techniques sensitive to the total magnetization of the sample to look at the behavior of the free induction decay signals [87, 88, 89] or spin echo trains [73]. As discussed above and in Ref. [88], it has been found that following a 90° RF pulse in a uniform magnetic field the magnetization develops a dynamic instability leading to an abrupt decay of the NMR signal. On the other hand, for small tip angles the NMR signal often persists longer than one would expect in the absence of magnetic dipolar interactions. In particular, it was found that in U shaped samples the NMR spectrum develops a series of sharp lines [88, 90] when one would naively expect a broad spectral profile due to magnetic field gradients created by dipolar fields.

For most of the analysis and data in this work, we assume nominally spherical geometry and small perturbations from uniform polarization. For the moment we also assume that deviations of the applied field from perfect homogeneity are dominated by linear gradients in the longitudinal direction $\mathbf{H} = (H_0 + gz)\hat{\mathbf{z}}$. We look for perturbations of the magnetization with a linear gradient in the longitudinal direction

$$\mathbf{M}(t) = \mathbf{M}_0 + M_0\{m_x(t), m_y(t), m_z(t)\}\frac{z}{R}. \tag{1.42}$$

We are primarily sensitive to the gradient of the y component of the magnetization (see Fig. 1.10). Including the dipolar field due to the above magnetization profile in the Bloch equation leads to the following solution for m_y following a pulse that tips the magnetization into the x direction of the rotating frame by an angle α:

$$m_y(t) = -\frac{\gamma g R M_0}{\beta}\sin(\alpha)\sinh(\beta t),$$

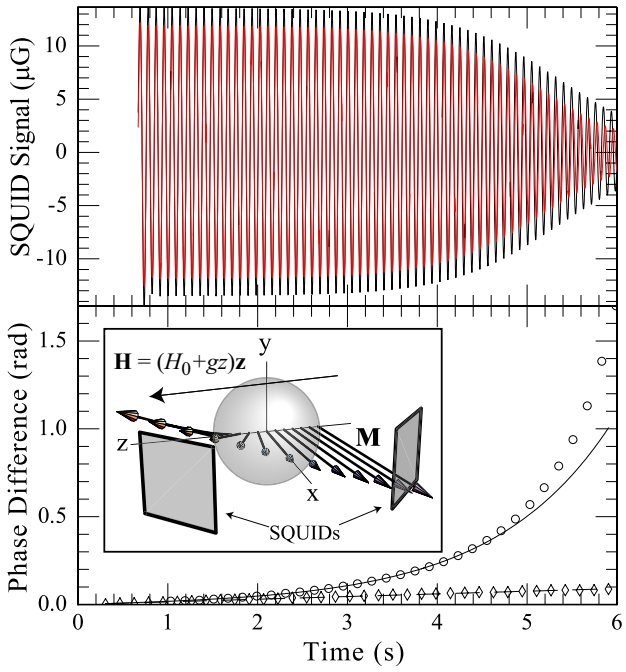

Figure 1.10: Top panel: SQUID signals following a $\pi/2$ pulse in a small magnetic field gradient. Bottom panel: phase difference between the two SQUID signals (circles) fit to linear model (solid line) and expected phase deviation neglecting dipolar interactions (diamonds). Inset shows the Relative orientation of SQUIDs and magnetization. The magnetic field is in the z direction.

$$\beta = \frac{4\sqrt{2}\pi}{15} M_0 \gamma \left(1 - 3\cos(2\alpha)\right)^{1/2}. \tag{1.43}$$

(See Chapter 3 for a detailed derivation). Here β is proportional to the strength of the long-range dipolar interactions. Thus, for $\alpha < 35°$ the linear magnetization gradients oscillate at a frequency $\omega_{lin} = i\beta$ while for $\alpha > 35°$ they grow exponentially, consistent with earlier results [91, 92].

Fig. 1.10 shows the SQUID signals and the phase difference between the two signals, directly proportional to the gradient m_y (this is discussed further in Chapter 3) following a $\pi/2$ pulse. The phase difference grows exponentially and is well described by the linear model, as indicated by the agreement between the circles and the solid line in the bottom panel, until the phase difference becomes large. The top panel of Fig. 1.11 shows the SQUID signals (solid and dashed lines) following a small tip angle pulse (β imaginary) in the presence of a large gradient. Note that the free induction decay is extended substantially

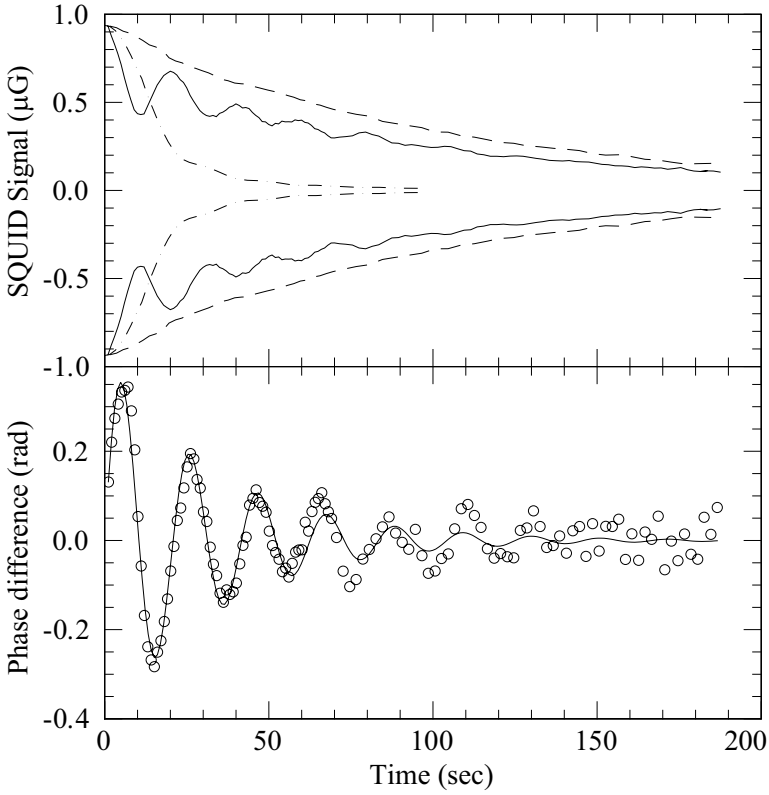

Figure 1.11: Top panel: SQUID signal envelopes (solid and dashed lines) following a small tip angle pulse in the presence of a large magnetic field gradient. The dash-dot line shows the expected signal neglecting dipolar interactions. Bottom panel: phase difference between the two SQUID signals

compared to the non-interacting case, given by the dash-dot line. The bottom panel of Fig. 1.11 shows the phase difference between the two SQUID signals. As predicted by the linear model, in the small tip angle regime, the gradient m_y, and thus the phase difference oscillate. The frequency and amplitude of phase oscillations are in good agreement with the predictions of the linear model.

The large tip angle behavior predicted by the linear model immediately presents us with a very attractive way to measure very small applied magnetic (or electric) field gradients. For $\alpha = 90^\circ$ the solution for the y component of the magnetization gradient becomes

$$m_y(t) = -\frac{\gamma g R}{\beta} \sinh(\beta t),$$
$$\beta = \frac{8\sqrt{2}\pi}{15} M_0 \gamma. \tag{1.44}$$

The gradient of the y component of the magnetization thus grows exponentially with a time constant β. For magnetization distributions well described by the linear model, the phase difference in the SQUID signals is directly proportional to the gradient of the y component of the magnetization $\Delta\phi = \zeta m_y(t)$ where ζ depends on the relative geometry between the cell and the SQUID pickup coils. Thus comparing the interacting case with the noninteracting case where the phase difference in the SQUID signals is $\Delta\phi_{NI} = \zeta\gamma g R t$, we see that the phase difference is amplified by a gain factor

$$G = \frac{\sinh \beta t}{\beta t}. \tag{1.45}$$

In principle this can be quite large. For $M_0 = 100\mu$G (we regularly reach $M_0 = 400\mu$G), $\beta = 1.75$ s^{-1}, and at 5 seconds $G = 360$. Rather than having to wait a long time for the effects of a small gradient to grow large enough to measure with relatively noisy SQUID magnetometers, as in linear spin precession, nonlinear effects from dipolar interactions amplify the effects of small magnetic field gradients until they are large enough to be easily measured.

Chapter 2

Experimental Setup

2.1 Overview

An overview of the experiment may be found in Fig. 2.1. Hyperpolarized xenon gas is produced outside the magnetic shields via spin exchange in an optically pumped rubidium vapor cell and stored in solid form at high magnetic field in a LN_2 cold trap. When the trap is warmed, polarized gas flows through a copper or glass tube to condense in a spherical cell inside the magnetic shields. A set of coils allow control of all three components of the magnetic field, linear gradients of the magnetic field and some higher order gradients. The cell sits inside a narrow, vacuum insulated, double wall tube through which we flow nitrogen vapor to maintain a temperature of 173K. Two high T_c SQUID magnetometers adjacent to the cell, oriented at 45 and 135 degrees to the magnetic field, monitor the oscillating magnetic field created by the precessing magnetization. As discussed in the introduction, gradients of the magnetization in the longitudinal direction show up as a phase difference in the two SQUID signals.

2.2 Production of Hyperpolarized Liquid ^{129}Xe

Hyperpolarized ^{129}Xe was produced using the standard method of spin exchange optical pumping [47] where collisions between xenon atoms with an optically pumped Rb vapor

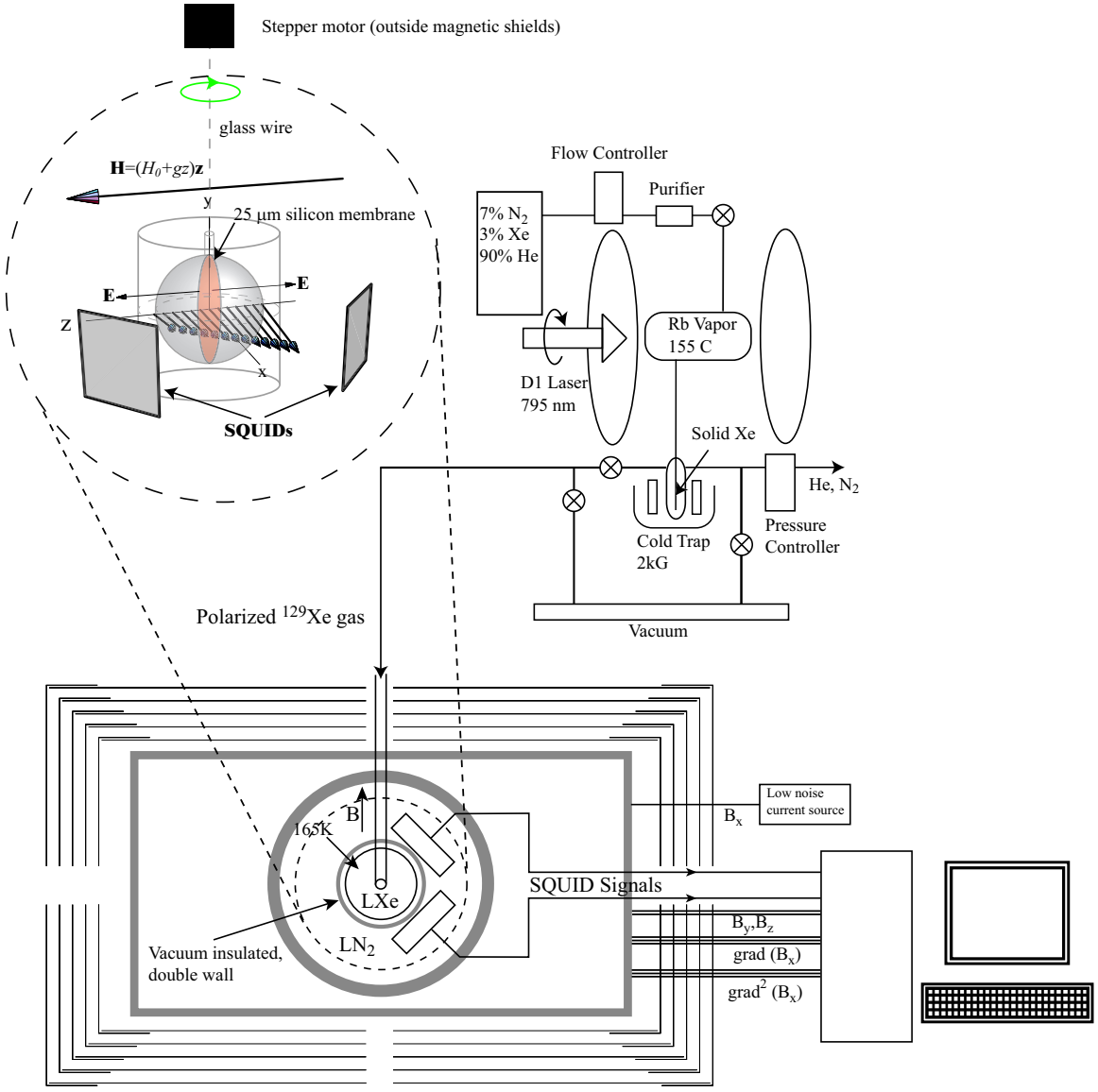

Figure 2.1: Overview of the experimental setup. A major component of the system not shown is the vacuum system.

transfers optical angular momentum to the Xe nuclei. A brief review of this method may be found in the introduction, or for a more complete review of the physics behind spin exchange optical pumping, see Ref. [53].

A gas mixture of 3% Xe (natural abundance), 7% N_2 and 90% He flowed through a purifier and the optical pumping cell containing Rb vapor. The cell temperature was monitored via a non-magnetic thermocouple. We maintained the temperature at 155° C by flowing air first through a heater controlled by an Omega temperature processor and then through the oven containing the optical pumping cell. A set of 4 coils, arranged so that gradients of the magnetic field up to 4th order were cancelled, generated a magnetic field of approximately 40 G in the region of the Rb cell. We polarized the Rb vapor by illuminating the cell with circularly polarized light from a 120 watt diode laser array (kindly donated by Amersham Nycomed corporation) tuned to the 795 nm D1 transition, which propagated in the direction of the magnetic field. The Rb vapor was optically thick on resonance, and about 50% of the broadband radiation was absorbed. As discussed in the introduction, the Rb ground state angular momentum is transferred to the xenon nuclei through spin exchange. For spin-exchange cross sections, refer to Chapter 1, Fig 1.6.

To optimize the polarization, we monitored the xenon NMR signal in the optical pumping cell with a resonant LC circuit tuned to the Larmor precession frequency located on top of the optical pumping cell. We used a pulse sequence generator to flip an RF switch between "listening" and "pulsing" modes, similar to the right side of Fig. 1.8. In the former, the NMR LC circuit was connected to a preamp (gain of 5000) and in the latter, the LC circuit was connected to a function generator tuned within 100 Hz of the Larmor precession frequency of the xenon nuclei. The output of the preamp is multiplied with a reference signal by an RF mixer and the high frequency components were filtered out to yield a signal at the difference frequency between resonance and reference. Typical signals were on the order of 70 mV. To calibrate the spectrometer, we placed a small coil through which we ran a known current to generate an oscillating dipole moment and analyzed the resulting signal in the spectrometer. We found that the typical polarization in the cell was

around 5%, with an error of about a factor of 2 due to geometry.

The polarized gas mixture flowed out of the optical pumping cell, through a cold trap immersed in liquid nitrogen in a 2kG field, where the xenon froze out of the mixture and the buffer gas leaves the system. In a sufficiently large field ($B > 600$ G) and for temperatures below 120 K, the longitudinal relaxation time of frozen xenon is several hours [93], dominated by modulation of the spin-rotation interaction via phonons. At temperatures above 120 K, modulation of the dipole-dipole interaction via vacancy diffusion dominates the relaxation process, substantially reducing the relaxation time. We operated at 77 K, and hence, little polarization was lost during storage. After approximately 25 minutes of flowing at a rate of 1.2 liters per minute, we have accumulated enough solid xenon to fill the liquid xenon cell inside the magnetic shields. The remainder of the He and N_2 is evacuated from the system. As the relaxation time of the frozen xenon is shorter at higher temperatures, we endeavored to warm the cell as quickly as possible to minimize the amount of time the frozen xenon spends at high temperatures. To facilitate this, we minimized the volume of the cold trap, isolating it from the liquid xenon cell through a series of valves. This process increased the rate at which the pressure and the heat conductivity of the xenon vapor rises. When the pressure reaches the triple point, the valve to the xenon cell was opened, while continuing to heat the cold trap with the heat gun. We attempt to maintain the pressure at about 100 psi while the xenon is condensing in the cell. We have achieved polarizations in the liquid phase of about 3% (about 400 μG). In more detailed studies of the freezing and thawing process, Brian Patton in the Happer group has found that for fields in the neighborhood of 2kG, up to 80% of the polarization is retained during the freezing and thawing process. If the calibrations in the optical pumping cell are to be believed, the entire transfer of xenon from optical pumping cell to liquid xenon cell is quite efficient.

2.3 Magnetic Shields and Coil

To reduce the magnetic field noise from external sources, we performed our measurements inside a set of 5 layer, cylindrical, high μ metal magnetic shields manufactured by Amuneal

Shield number	length (inches)	radius (inches)
1	48	24
2	40	22
3	34	20
4	30	18
5	28	16

Table 2.1: Physical dimensions of magnetic shields

with a shielding factor of approximately 500000. The dimensions of our shields may be found in Table 2.1. A titanium support structure kept the shields in a concentric configuration and allowed minor adjustments of the location of the magnetic field windings with respect to the inner shield. Titanium was chosen because it has a similar coefficient of thermal expansion as high μ metal, reducing thermal stress in the magnetic shields and the associated magnetic field drifts. We chose to apply the holding magnetic field in the horizontal plane because most of the 60 Hz magnetic field noise is in the vertical direction from power lines running along the walls. Further, the holding field of about 10 mG is applied transverse to the axis of the shields, in the x direction of the lab frame, as the transverse shielding factor is about twice that of the longitudinal shielding factor. High μ metal shields have been extensively used in similar applications; a general discussion may be found in Ref. [94].

Control of the magnetic field was accomplished via a set of coils wound around a 12 inch diameter G10 cylinder. The homogeneous field in the transverse directions were created by a set of windings, shown in Figure 2.2a), which approximate a sinusoidal or cosinusoidal distribution of current for which, inside an infinitely long cylinder the magnetization is perfectly uniform. For reference, the angular coordinates of the wires in the first quadrant for producing a magnetic field in the x direction are 14.8352, 25.842, 33.5574, 39.9445, 45.573, 50.7036, 55.4819, 60.0, 64.3208, 68.4899, 72.5424, 76.5066, 80.406, 84.2609, 88.0898. The field along the symmetry axis of the shields was created by a simple solenoidal coil, each turn being spaced 1.27 cm apart. Care was taken to cancel the axial component of the current by making each turn a complete circle, connected to the next by a short piece of wire. The return current traced the short segments back. Using a Mathematica notebook, we numerically integrate the contribution to the relevant component of the magnetic field

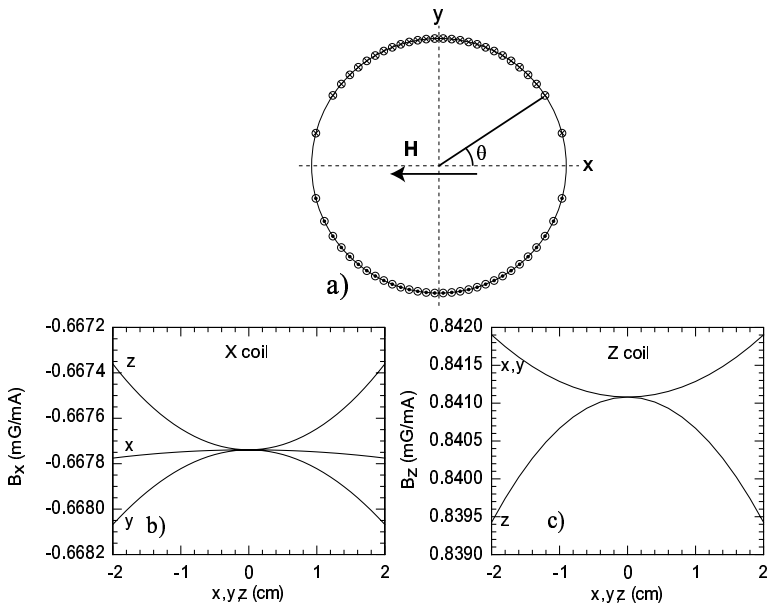

Figure 2.2: a) Coil to produce homogeneous magnetic field in x direction. b) Results of numerical calculations of the magnetic field from the coil shown in a). c) Results of numerical calculations for the simple solenoidal coil creating a magnetic field in the z direction.

from a series of straight wires and arcs, neglecting image currents in the magnetic shields. The results of these calculations are shown in Fig 2.2b) and c). Our numerical integrations indicate that the magnetic field should be uniform to about 3 parts in 10^5 over the region of the cell. For an infinitely long solenoid it would be possible to take into account image currents. Our coil has a fairly small aspect ratio and thus we neglect image currents, resulting in a difference between calibration and calculation of about 30%.

The actual calibrations of the magnetic field, determined by using a flux gate magnetometer are 0.89 mG/mA and 0.84 mG/mA for the transverse and longitudinal fields respectively, differing from the calculated calibrations due to the image currents in the magnetic shields. These calibrations are subject to change slightly depending on the number of shields in place. Ambient magnetic field gradients were on the order of 5 μG/cm. We will discuss the effects of magnetic field inhomogeneities in more detail later.

An ultra low noise current source [95] with a power spectral density of 10^{-20} A^2/Hz supplied about 10 mA to the "X" transverse coil. A mercury battery is used as a voltage

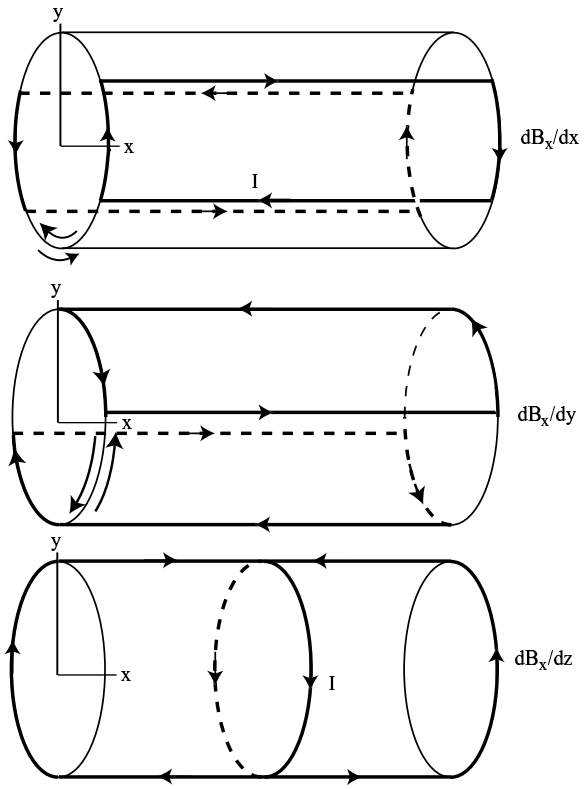

Figure 2.3: Schematic of the windings used to create gradients of the x component of the magnetic field

reference to bias the gates of a pair of FETs and a feedback circuit used to keep the drain-source voltage constant. We use an analog output card to directly supply oscillating current to the "Y" and "Z" coils, 90 degrees out of phase with each other, generating a true rotating field to tip the spins into the transverse direction

A set of three extra coils depicted in Fig. 2.3 allowed control of the gradients $\partial B_x/\partial x, \partial B_x/\partial y, \partial B_x/\partial y$. As the magnitude of the magnetic field associated with these gradient coils is substantially smaller than the homogeneous fields we worried less about the stability of the current source and used a simple op-amp circuit as a voltage source referenced to the output of the analog output card in the computer, allowing computer control of the magnetic field gradients. The calibrations were 0.44 mG/cm/mA for dB_x/dx and dB_x/dy and 0.41 mG/cm/mA for dB_x/dz.

A third set of three coils, topologically equivalent to Helmholtz coils, provide some

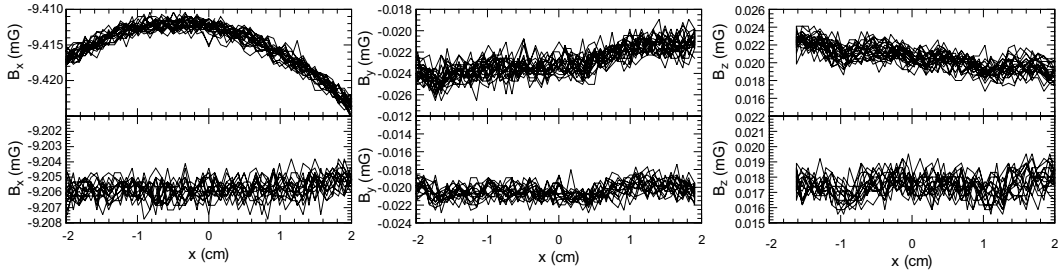

Figure 2.4: Measurements of the magnetic field inside the magnetic shields along the x direction. Top panels are unshimmed, bottom panels show the field with corrections using the three first order gradient coils and one of the second order gradient coils.

control of 2nd order gradients of B_x. Unfortunately, these coils each produce gradients $\partial^2 B_x/\partial x^2$,$\partial^2 B_x/\partial y^2$ and $\partial^2 B_x/\partial z^2$ and are not orthogonal in 2nd order gradient space. Hence it is difficult to fully zero all second order gradients with reasonably small currents. However it is possible to substantially reduce the second order gradient $\partial^2 B_x/\partial x^2$ with a single coil at small cost to the other 2nd order gradients. Numerical simulations generally indicate that gradients of the magnetization grow faster in response to longitudinal gradients of the applied field than transverse gradients of the applied field, so this is an acceptable state of affairs. Fig 2.4 shows measurements of the magnetic field made by oscillating a three axis flux gate magnetometer back and forth along the x direction. To obtain information about the first order gradients $\partial B_x/\partial y$ and $\partial B_x/\partial z$, one can use the fact that $\nabla \times \mathbf{B} = 0$. Use of the second order gradient coil reduces $\partial^2 B_x/\partial x^2$ by a factor of greater than 5. Without correction there is a variation in the longitudinal direction by about a part in 10^4.

2.4 SQUIDS, dewar and cell

We used high T_c SQUID magnetometers manufactured by Tristan Technologies. Our SQUID magnetometers had a noise level of about $2 \times 10^{-3}\mu G/\sqrt{Hz}$ at 10 Hz. Shown in Fig. 2.5 is a power spectrum of our SQUID magnetometers. Tristan rates these at about $3 \times 10^{-4}\mu G/\sqrt{Hz}$. We suspect that the poor performance is related to RF pickup in the cables connecting the SQUID to the flux locking loop.

As an entertaining aside, out of the box, the SQUID magnetometers connected to the

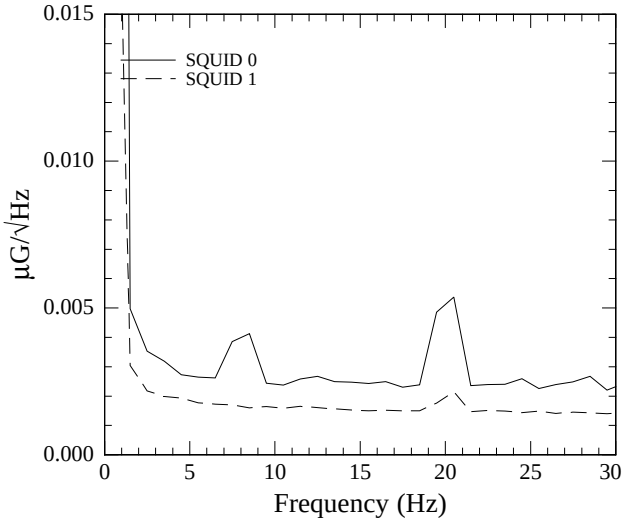

Figure 2.5: Noise spectrum of our SQUID magnetomters.

flux locking loop via a very aesthetically pleasing brass connector. Unknown to us when we started working with these magnetometers, brass is quite magnetic, and in our setup these connectors were creating magnetic field gradients on the order of 50-100 μG/cm at the xenon cell, wreaking havoc on the xenon spin precession, especially for large tip angles. We finally realized this by wiggling one SQUID relative to the other. Removing the brass connectors greatly improved our data. Unfortunately, this required the use of homemade cables which could be responsible for the larger levels of noise shown in Fig. 2.5.

As we shall discuss in more detail later, the action of the feedback loop to keep the flux through the SQUID constant is a potential source of noise in the measurement of an EDM. To keep the flux through the SQUID constant the feedback coil generates a small magnetic field, and because it is necessarily relatively close to the sample, this field is quite inhomogeneous. Fig. 2.6 shows the phase deviation (solid line) of the xenon NMR signal relative to its average frequency and the DC value of the SQUID signal (dashed line) during the free induction decay following a small angle pulse. When the SQUID loses lock and jumps between flux quanta, the current through the feedback loop abruptly changes causing a jump in the magnetic field. The magnetic field is proportional to the derivative of the

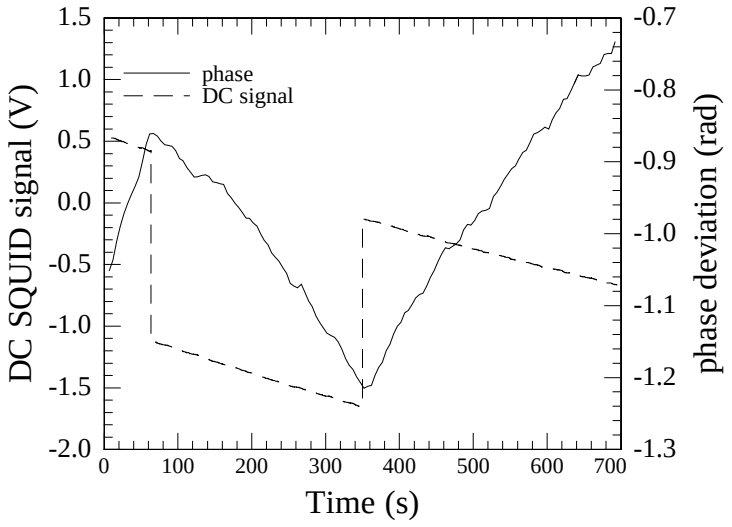

Figure 2.6: Phase of xenon spin precession (solid line) and DC SQUID signal (dashed line). The dashed line is the DC SQUID signal. When the SQUIDs jump to a new lock, there is is a kink in the phase of the xenon spin precession.

phase $B = \frac{1}{\gamma}\frac{d\phi}{dt}$ so a discontinuity in the magnetic field corresponds to a discontinuity in the slope of the phase deviation. From the data shown here, we determine that the SQUID creates an average magnetic field over the cell of about $\langle B_{sq}\rangle_V = 0.37\,\mu$G/Volt or using the calibration of the SQUIDs $\langle B_{sq}\rangle_V = \frac{0.37\,\mu\text{G/V}}{7.4\,\mu\text{G/V}} = 0.05\,\mu\text{G}/\mu\text{G}$.

The feedback coil is several mm in diameter compared to its distance from the center of the cell of ~ 1.5 cm and hence we approximate it as a dipole. Referring to Fig. 2.1, it is oriented parallel to the y axis, rotated by 45° relative to the x axis, $\mathbf{m}_{sq} = \frac{m_{sq}}{\sqrt{2}}(\hat{\mathbf{x}} + \hat{\mathbf{z}})$. To find the magnitude of the dipole moment, we numerically average the $\hat{\mathbf{z}}$ component of the magnetic field it generates over the cell to find for $R = 0.5$ cm and the SQUIDs a distance $r_{sq} = 1.5$ cm from the center of the cell

$$m_{sq} = \left\langle B_z^{(sq)} \right\rangle_V \times 1.2\,(\text{cm}^3) \tag{2.1}$$

so that $m_{sq} \approx 0.44\,\mu$erg/G/Volt. The calibrations of our SQUIDs are approximately 7.4 μG/Volt on high gain so $m_{sq} = \eta\delta B$ where $\eta = 0.059\mu$erg/G/μG and δB_{sq} is the average magnetic field through the pickup loop. A dipole magnetic moment oriented at 45° relative to the magnetic field and a distance $r_{sq} = 1.5$ cm from the center of the cell generates an

average gradient of the $\hat{\mathbf{z}}$ component of the magnetic field

$$\langle g^{(sq)} \rangle_V = \frac{1}{V} \int_V \frac{dB_z^{sq}}{dz} dV = 0.6(\mathrm{cm}^{-4}) m_{sq}. \tag{2.2}$$

We thus see that a fluctuation of the output of the SQUID generates an average gradient across the cell.

$$g^{(sq)} = 0.044(\mathrm{cm}^{-1}) \delta B_{sq}. \tag{2.3}$$

In Chapter 5 we discuss a modification on the standard SQUID magnetometer that can suppress this effect.

A side view of the dewar, SQUIDs, cell and all the mounting hardware is shown in Fig 2.7. The dewar, constructed of glass by H.S. Martin, is topologically equivalent to a donut. The outer walls are silvered to improve the boil off time of the N_2, with the exception of a thin strip through which an image of the cell can be projected onto a CCD camera. The inner column is also double walled and vacuum insulated but lacks the silvering to reduce magnetic noise due to Johnson currents, and to allow optical access to the cell. To keep the liquid xenon cell at 173 K, cold nitrogen vapor flows down through the inside of the inner column. Temperature gradients can be applied by a jet of nitrogen flowing up through the bottom of the dewar. The dewar is held rigidly between two 1/4" G10 plates attached together via four 3/8" G10 rods. The SQUIDs are mounted to the upper of these two plates via 3/8" G10 rods. The dewar and SQUID assembly is held between two additional G10 plates via 1/4" $\times$ 20 nylon screws which provide both vertical adjustment and apply pressure to the G10 cylinder so that the assembly cannot move with respect to the windings on the cylinder.

The cell has its own mount so that it can be easily inserted into the dewar without disassembling the magnetic shields. A photo of the assembly is shown in Fig. 2.8. A G10 plug through which nitrogen vapor flows to control the cell temperature, forms a seal with the inner column of the dewar and holds the cell stem with a nylon set screw. The G10 plug is connected to an aluminum block that sits outside the shields via two 1/4" aluminum rods.

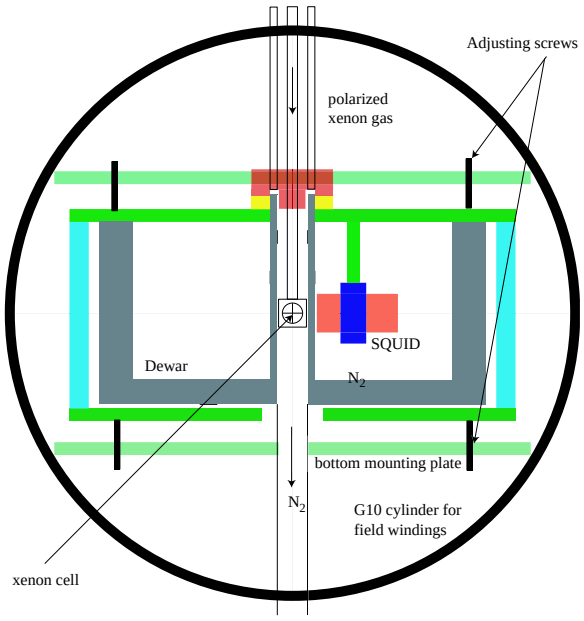

Figure 2.7: View of SQUIDs, dewar and cell from the side. All materials are G10 except for the dewar. Not shown are the input and output ports for liquid nitrogen

Our early cells were simple blown glass constructions, courtesy of our expert glass blower, Mike Souza. After some time we realized that despite Mike Souza's great skill, these cells were not spherical enough. The effects of cell deformations are briefly discussed in the next two chapters. To remedy this problem, we switched to cells constructed from two hemispherical lenses (manufactured by Mindrum Precision Inc.), one with a 1 mm hole, and a piece of 1mm capillary tubing joined to a larger diameter (3 mm ID) piece of pyrex tubing glued together with Norland NOA 88 UV curing cement. Inside the cell was a 25μm thick octagonal silicon membrane, cut from a larger wafer of silicon using a diamond dicing saw. Glued to the membrane was a thin glass wire. To construct the cell, we used the following procedure:

1. All pieces were washed in a bath of acetone in an ultrasonic cleaner.

2. Glass tube/capillary piece was mounted in cell holder.

3. Lens with hole was glued to capillary (short cure 5-10m).

4. Glass wire was glued to silicon membrane and inserted into the long glass tube.

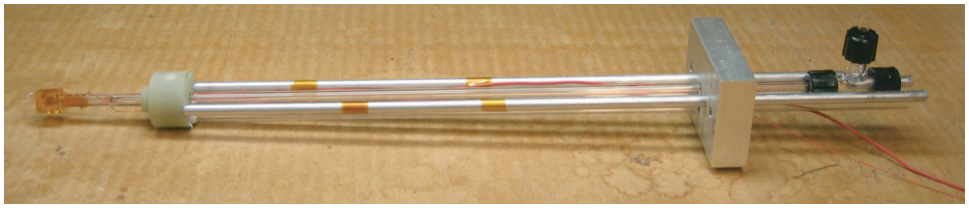

Figure 2.8: Photo of cell and mount.

5. Vacuum feedthru for turning glass rod was attached.

6. Second hemisphere glued to the first.

7. Assembly was cured for 12 hours under the UV lamp.

8. Apparatus was connected to the vacuum system and baked out for several days at 180°C.

The last step was important to ensure long relaxation times as the pumping speed through the thin capillary was quite small. Without baking out the cell, contamination (probably residual water on the walls of the cell) reduced the relaxation time to approximately 800 seconds. We determined the exact distance from the cell to the SQUIDs by measuring the signal that a known current flowing in a calibration loop attached to the cell induces in the SQUIDs.

In older cells which were made of blown glass we characterized the degree of sphericity of inner cell walls by submerging them in mineral oil which has approximately the same index of refraction as glass, so only the inner surface of the cell reflects light. We reflected a laser from the cell as it was rotated around its center. Any deviations of the cell inner surface from the spherical shape result in motion of the laser beam. Using a beam position monitor we measured the displacement of the beam and characterized the shape of the cell in terms of spherical harmonics. Simple calculations show that for small deviations from spherical shape the $l = 2$ terms generate a homogenous magnetic field and $l = 3$ terms generate a first order magnetic field gradient. In general, these magnetic fields and gradients rotate together with the magnetization, so their effects are not trivial, though in a few cases there

are simple solutions. We briefly discuss these effects in the next two chapters.

2.5 SQUID feedback for spin control

To reduce uncertainties in the tip angle, we suppressed residual unwanted transverse components of the magnetization by employing a feedback scheme which generated a magnetic field $\pi/2$ out of phase with the precessing magnetization. Depending on the sign of the phase shift this either tips the magnetization towards or away from the z direction. The output of one of the SQUID magnetometers was connected to the "Y" coil. The plane of the SQUID pickup coils were parallel to the y axis of the lab frame and hence this did not directly introduce any extra signal in the SQUID magnetometers. In this way it was possible to completely remove the homogeneous part of the transverse component of the magnetization. By using the difference between the two SQUID signals and feeding this back into the appropriate gradient coils it should be possible to reduce residual gradients of the transverse components of the magnetization.

Chapter 3

Theoretical understanding of long range dipolar interactions

3.1 Introduction

In this chapter, we explore a variety of analytical and numerical models to understand the effects of long range magnetic dipolar interactions. Much of this work was previously reported in Refs. [73, 101, 96, 97]. The theoretical basis for treatment of distant dipolar fields has been well-established. They can be modelled classically as a sum of the fields produced by the magnetic dipoles of individual spins [98]. A full quantum-mechanical treatment is also possible by following the evolution of a density matrix representing all spins in the sample [99]. It has been shown that the two approaches are equivalent under most conditions [98, 99, 100]. Detailed analysis of dipolar interactions is complicated, in spite of their formal simplicity, because they cause non-linear and non-local effects which are sensitive to the geometry of the sample and the boundary conditions. Other than the results discussed here only a small number of analytic results have been obtained so far, including linear stability analysis for a uniform magnetization distribution [91, 92].

Numerical modelling of dipolar interactions in real space is computationally intensive because of their non-local nature and the only results obtained previously were performed

on a small number of discrete spins [91]. It has been shown that the dipolar field can be represented by a local function of the magnetization in Fourier space [102] and efficient computational techniques using Fast Fourier Transforms have been developed [103].

Here we use classical Bloch equation formalism to describe the behavior of the magnetization. Xenon has two nonzero spin isotopes: ^{129}Xe ($I = 1/2, 26\%$) and ^{131}Xe($I = 3/2, 21\%$). Local electric field gradients from neighboring atoms interact strongly with the electric quadrupole moment of the latter leading to rapid spin relaxation and hence we may ignore effects of the $I = 3/2$ isotope. The modified Bloch equations are

$$\begin{aligned} \frac{\partial \mathbf{M}}{\partial t} = \gamma \mathbf{M} \times (\mathbf{B}_{ext} &+ \mathbf{B}_d) + D\nabla^2 \mathbf{M} \\ &- \frac{M_x \hat{\mathbf{x}} + M_y \hat{\mathbf{y}}}{T_2} - \frac{M_z \hat{\mathbf{z}}}{T_1} \end{aligned} \tag{3.1}$$

where $\mathbf{B}_{ext}$ is the external magnetic field, $\mathbf{B}_d$ is the dipolar field, D is the coefficient of diffusion, and T_1 and T_2 are the longitudinal and transverse relaxation times. For evolution of the system on short time scales (10-20 seconds) the first term dominates for parameters describing our experiment. At time scales on the order of several hundred seconds, diffusion and relaxation become important. Typically included in Eq. (3.1) is the field created by a resonant RF pickup coil leading to radiation damping. Because SQUID magnetometers do not rely on a resonant circuit, this term is absent here. The feedback coil in the SQUID magnetometer can create substantial magnetic fields (we discuss a method for suppressing these unwanted fields in chapter 5), however these fields are in phase with the precessing magnetization and thus we do not consider them here as they do not have a substantial effect on the transverse component of the magnetization. In Chapter 5 we will discuss this issue further. A full treatment would also include the effects of convection due to temperature gradients, however, we find that for a sufficiently small convection occurs on time scales slow compared to dipolar interactions, and under these conditions, our experimental results agree well with the predictions of Eq. 3.1. Presumably, for an inverted temperature gradient, where the cell is warmer on the top, convection will not occur at all.

In addition to the simplifications mentioned above, for most of what follows, we assume a spherical cell for which, in the absence of applied magnetic field gradients or initial mag-

netization inhomogeneities, the dipolar field seen by the spins is equal to zero. We only briefly address the magnetic field due to various cell deformations and discuss experimentally some of these effects in the next chapter. Finally, in most models we use the rotating wave approximation where we ignore fields that rotate in the opposite direction relative to the magnetization, which is generally very accurate in high field NMR experiments. However, in our low-field experiments the accuracy of this approximation is not obvious, since the magnetic field of 10 mG along the z direction is only 10-100 times greater than the dipolar magnetic fields. To understand possible deviations from this approximation, we have also performed simulations in the lab frame. This also permits the study of the effects of transverse gradients.

The chapter is organized as follows: In Section 3.2 we discuss the "linear model" where we consider the evolution in the presence of a longitudinal linear magnetic field gradient $\mathbf{H} = (H_0 + gz)\hat{\mathbf{z}}$ and keep terms of the magnetization linear in z. In Section 3.3 we discuss a series of analytical and numerical models that can address the effects of higher order magnetic field and magnetization gradients. In Section 3.4 we discuss the solution to these models for a variety of different parameters.

3.2 Linear Model

We are primarily interested in the first order longitudinal gradient of the magnetic field g, $\mathbf{H} = (H_0 + gz)\hat{\mathbf{z}}$. Assuming azimuthal symmetry of the magnetization, it may be expanded in a Taylor series

$$\mathbf{M}(\mathbf{r}, \mathbf{t}) = M_0 \sum_{i,k} \mathbf{m}^{(i,k)}(t) \frac{z^i (x^2 + y^2)^k}{R^{i+2k}}. \tag{3.2}$$

The motivation behind such an expansion is discussed further in the Appendix. When only a small linear gradient is present, for small deviations of the sample from uniformity, the magnetization will be well described by a linear profile $\mathbf{m}^{(1,0)} z/R$. This case has a particularly simple analytic solution that describes many of the features of our data and provides substantial insight into the dynamics of the magnetization. Therefore we will

elaborate in detail on this "linear model".

The magnetic field created by a magnetized sample in a current free region may be found from the magnetic potential $\mathbf{H}_d = -\nabla\Phi_M$ [104], where the magnetic potential is

$$\Phi_M(\mathbf{x}) = -\frac{1}{4\pi}\int_V \frac{\nabla\cdot\mathbf{M}(\mathbf{x}')}{\mid \mathbf{x}-\mathbf{x}' \mid} d^3x' + \frac{1}{4\pi}\int_S \frac{\mathbf{n}'\cdot\mathbf{M}(\mathbf{x}')}{\mid \mathbf{x}-\mathbf{x}' \mid} da'. \tag{3.3}$$

The magnetic field felt by the spins is $\mathbf{B} = \mathbf{H}_{ext} + \mathbf{H}_d + 4\pi/3\mathbf{M}$. The final term differs from the classical result $4\pi\mathbf{M}$, because of the Pauli exclusion principle: Two fermions cannot occupy the same position in space, so the δ function part of the classical dipolar field does not contribute. Expanding the denominator in the integral in terms of spherical harmonics [104]

$$\frac{1}{|\mathbf{r}-\mathbf{r}'|} = \sum_{l=0}^{\infty}\sum_{m=-l}^{m=l}\frac{4\pi}{2l+1}\frac{r_<^l}{r_>^{l+1}}Y_{lm}(\theta,\varphi)Y_{lm}^*(\theta',\varphi') \tag{3.4}$$

we can write

$$\Phi_M = \sum_{l=0}^{\infty}\phi_l^{(s)} + \phi_l^{(v)} \tag{3.5}$$

where

$$\phi_l^{(s)} = \frac{4\pi}{2l+1}\frac{r^l}{R^{l+1}}\sum_{m=-l}^{l}Y_{lm}(\theta,\phi)\int_S \hat{\mathbf{n}}'\cdot\mathbf{M}(\mathbf{x}')Y_{lm}^*(\theta',\phi') \tag{3.6}$$

and

$$\begin{aligned}\phi_l^{(v)} = \frac{4\pi}{2l+1}\sum_{m=-l}^{l} Y_{lm}(\theta,\phi) \quad \Big(&\int_\Omega d\Omega\int_0^r \frac{r'^l}{r^{l+1}}\nabla'\cdot\mathbf{M}(\mathbf{x}')Y_{lm}^*(\theta',\phi')r'^2dr' \\ &+\int_\Omega d\Omega\int_r^R \frac{r^l}{r'^{l+1}}\nabla'\cdot\mathbf{M}(\mathbf{x}')Y_{lm}^*(\theta',\phi')r'^2dr'\Big)\end{aligned} \tag{3.7}$$

are the terms arising from the surface and volume integration respectively. For a magnetization profile well described by linear gradients, the nonzero terms, in cartesian coordinates are,

$$\begin{aligned}
\phi_0^{(s)} &= \frac{4\pi R}{3}M_0 m_z^{(1,0)}(t) \\
\phi_1^{(s)} &= \frac{4\pi}{3}M_0\sin(\alpha)x + \frac{4\pi}{3}M_0\cos(\alpha)z \\
\phi_2^{(s)} &= \frac{4\pi}{5R}M_0\Big[m_x^{(1,0)}(t)xz + m_y^{(1,0)}(t)yz \\
&\quad + m_z^{(1,0)}(t)z^2 - m_z^{(1,0)}(t)(x^2+y^2+z^2)/3\Big] \\
\phi_0^{(v)} &= \frac{2\pi}{3R}M_0 m_z^{(1,0)}(t)\left[3R^2 - x^2 - y^2 - z^2\right]
\end{aligned} \tag{3.8}$$

Ignoring terms with any transverse dependence because they average to zero in the rotating frame one finds that

$$\mathbf{B}_d = \mathbf{H}_d + 4\pi/3\mathbf{M} = \frac{8\pi M_0 z}{15R}\left\{m_x, m_y, -2m_z\right\}. \tag{3.9}$$

The time evolution of the magnetization is determined using the Bloch equations $d\mathbf{M}/dt = \gamma\mathbf{M}\times\mathbf{B}$, neglecting diffusion and spin relaxation. We assume an initial uniform magnetization M_0 along the $\hat{\mathbf{z}}$ axis and consider the evolution after an RF pulse that tips it by an angle α into the $\hat{\mathbf{x}}$ direction of the rotating frame. Keeping only terms linear in z, the Bloch equations are

$$\begin{aligned}
\frac{dm_x^{(1,0)}(t)}{dt} &= -\frac{8\pi\gamma}{15}M_0\cos(\alpha)m_y^{(1,0)}(t) \\
\frac{dm_y^{(1,0)}(t)}{dt} &= \gamma\left(\frac{16\pi}{15}m_z^{(1,0)}(t) - gR\right)M_0\sin(\alpha) \\
&\quad +\gamma\frac{8\pi}{15}M_0\cos(\alpha)m_x^{(1,0)}(t) \\
\frac{dm_z^{(1,0)}(t)}{dt} &= \frac{8\pi\gamma}{15}M_0\cos(\alpha)m_y^{(1,0)}(t)
\end{aligned} \tag{3.10}$$

The solution to these coupled first order differential equations takes the simple form

$$m_x^{(1,0)}(t) = \frac{4gR\pi}{15\beta^2}M_0\gamma^2\sin(2\alpha)\left(-1+\cosh(\beta t)\right), \tag{3.11}$$

$$m_y^{(1,0)}(t) = -\frac{\gamma gR}{\beta}\sin(\alpha)\sinh(\beta t), \tag{3.12}$$

$$m_z^{(1,0)}(t) = -\frac{16gR\pi}{15\beta^2}M_0\gamma^2\sin^2(\alpha)\sinh^2(\beta t/2) \tag{3.13}$$

$$\tag{3.14}$$

where

$$\beta = \frac{4\sqrt{2}\pi}{15}M_0\gamma\left(1-3\cos(2\alpha)\right)^{1/2}. \tag{3.15}$$

Here β is proportional to the strength of the long-range dipolar interactions. For $\alpha < 35^\circ$ *beta* is imaginary and the linear gradients oscillate at a frequency $\omega_{lin} = i\beta$ while for $\alpha > 35^\circ$ β is real and the gradients grow exponentially. These results are consistent with the conclusions of a linear stability analysis carried out by Jeener [91, 92]: spectral clustering for small tip angles and dynamic instability for large tip angles. In the case of large tip

angles we will find it convenient to compare the evolution of $m_y^{(1,0)}(t)$ in the interacting case to the evolution in the non-interacting case. The latter is simply the limit of Eq. 3.12 as $\beta \to 0$, $m_{y,NI}^{(1,0)}(t) = \gamma g R t$. Hence we define a gain parameter

$$G = \frac{m_y^{(1,0)}}{m_{y,NI}^{(1,0)}} = \frac{\sinh(\beta t)}{\beta t}. \tag{3.16}$$

Thus we see that in the large tip angle regime, the gradient $m_y^{(1,0)}$ grows exponentially relative to the noninteracting case.

For completeness we present the solution for nonzero initial gradients of the magnetization $m_y(0) = \delta m_y$ and $m_z(0) = \delta m_z$. The solution to Eqns. 3.10 with $\alpha = \pi/2$ and $g = 0$ takes the form

$$m_y(t) = \delta m_y \cosh(\beta t) + \delta m_z \sqrt{2} \sinh(\beta t) \tag{3.17}$$

$$m_z(t) = \delta m_y \sinh(\beta t)/\sqrt{2} + \delta m_z \cosh(\beta t). \tag{3.18}$$

where $\beta = \frac{8\pi\sqrt{2}}{15}\gamma M_0$. Initial magnetization inhomogeneities grow at the same rate as inhomogeneities arising from applied field gradients. This represents a source of noise in an EDM measurement and will be discussed further in Chapter 5.

The signal in each SQUID is a convolution of the spatial configuration of the magnetization with the sensitivity of the SQUIDs to sources of magnetic fields. For our geometry the SQUIDs are preferentially sensitive to the magnetization on either side of the xy plane, so that for small gradients of the magnetization in the longitudinal direction, the phase difference in the SQUIDs is directly proportional to the first order gradient of the magnetization. For a 90° tip angle, the phase difference between the SQUIDs is

$$\Delta\phi = \xi m_y^{(1,0)} = \xi \frac{\gamma g R}{\beta} \sinh(\beta t), \tag{3.19}$$

where ξ is a numerical factor that depends on geometry and for our setup is about 0.5. This can be calculated using the method described in Section 3.3.6.

3.3 Higher Order Models

Our experimental measurements of the oscillation frequency $\omega_{\text{lin}} = i\beta$ and the exponential growth time constant were in good agreement with these predictions for $gR/M_0 \ll 1$. However, the linear model failed to account for several features of the data, such as the observed asymmetry in the SQUID signals or the decay of the gradient oscillations in Fig. 1.11, nor did it accurately predict the frequency of the gradient oscillations when $gR/M_0 \approx 1$.[101] Furthermore, by definition, the linear model cannot take into account the effect of higher order magnetization or applied field gradients. To perform an EDM experiment in the large tip angle regime it is important to understand the effects of higher order gradients, for, as we shall see shortly, high order gradients of the magnetization also grow exponentially in response to any small high order applied field gradient.

In this section we discuss three distinct numerical techniques developed to address these issues and the effects of spin diffusion. The first is based on a direct calculation of the magnetic field produced by a lattice of spins and employs several techniques to improve its computational efficiency. This calculation is performed both with and without making the rotating wave approximation (RWA), since for some of our data the holding magnetic field is comparable to the magnetization, unlike high field NMR experiments. This method also simplifies the treatment of transverse magnetic field gradients. The second method is an extension of the Fourier transform technique [103] where methods are introduced to eliminate the artifacts caused by periodicity assumed in Fourier transforms and distortions on sharp boundaries of the cell. The linear model described in the previous section is also extended in a Taylor series expansion of the magnetization to include up to 40 terms in the expansion. The solutions to these models are compared in Section 3.4, demonstrating good agreement with each other.

3.3.1 Numerical problems in modelling of dipolar interaction

The simplest possible general numerical model of dipolar interactions involves a discrete lattice of spins and direct summation of their magnetic fields [91]. However, since the

interaction is non-local, the time of such calculations grows as N^6, where N is the number of grid points in each dimension. To speed up the calculation we use the symmetry of the magnetization and the dipolar field for purely longitudinal magnetic field gradients. We find that grids with $N \leq 40$ in the rotating frame, and $N \leq 20$ in the lab frame can be analyzed in a reasonable time on a modern PC. We find however that the solution converges fairly quickly and grids with $N \geq 10$ give accurate results. We also developed a method for reducing the effect of the grid edges, which is very important for small size grids.

Two other methods that are more computationally efficient are also considered here. One, discussed previously in Ref. [103], transforms the magnetization into the Fourier space, where the magnetic field $\tilde{\mathbf{B}}(\mathbf{k})$ is a local function of $\tilde{\mathbf{M}}(\mathbf{k})$, reducing the computation time to $N^3 logN$. We discuss a method to reduce edge effects and the "ghost" cells that result from the periodicity of the Fourier transform

We further develop the model based on the Taylor series expansion of the magnetization discussed above. The dipolar magnetic fields created by each term in the expansion can be calculated analytically. We obtain a system of non-linear ordinary differential equations for the coefficients of the Taylor expansion, which can be easily solved numerically. This method is very computationally efficient but has a limited range of convergence for large magnetic field gradients and is non-trivial to adapt to other geometries.

3.3.2 Discrete lattice of spins in the rotating frame

In the rotating frame, the only part of the dipolar field that survives averaging over the Zeeman interaction with the holding field is [105]

$$\mathbf{B}_d(\mathbf{r}) = \int_V \frac{1 - 3\cos\theta_{rr'}}{2|\mathbf{r} - \mathbf{r}'|^3} [3M_z(\mathbf{r}')\hat{z} - \mathbf{M}(\mathbf{r}')] d\mathbf{r}' \tag{3.20}$$

where $\cos\theta_{rr'} = (z - z')/|\mathbf{r} - \mathbf{r}'|$. Here we consider evolution only in the presence of magnetic field configurations with azimuthal symmetry and it seems natural to use a cylindrical coordinate system, reducing the number of space dimensions from 3 to 2. However, we found that at small scales the dipolar magnetic field from a uniform magnetization distribution does not average to zero in a cylindrical coordinate system. For example, while the

contribution to the magnetic field from equal dipoles positioned at (0,a,0), (0,-a,0), (a,0,0), (-a,0,0), (0,0,a), and (0,0,-a) adds up to zero at the center (0,0,0), this is not the case for other spin lattice arrangements. Therefore, we find that only in Cartesian grids with uniform positioning of dipoles the $1/r^3$ singularity in the integral is exactly cancelled by contributions from all dipoles located on neighboring lattice sites.

However, this cancellation breaks down near the boundary and, if no measures are taken, the edge magnetic fields will be large and can affect the evolution of all dipoles, propagating inside the volume. To cancel edge effects we make use of the fact that the dipolar magnetic field inside a sphere of uniform magnetization $\mathbf{M}(\mathbf{r})$ is zero

$$\int_V \frac{1-3\cos^2\theta_{rr'}}{2|\mathbf{r}-\mathbf{r}'|^3}\mathbf{M}(\mathbf{r})d\mathbf{r}' = 0 \tag{3.21}$$

and hence

$$\begin{aligned} B_{dz}(\mathbf{r}) &= \int_V d\mathbf{r}' \frac{1-3\cos^2\theta_{rr'}}{|\mathbf{r}-\mathbf{r}'|^3} M_z(\mathbf{r}') \\ &= \int_V d\mathbf{r}' \frac{1-3\cos^2\theta_{rr'}}{|\mathbf{r}-\mathbf{r}'|^3} [M_z(\mathbf{r}') - M_z(\mathbf{r})] \end{aligned} \tag{3.22}$$

and similar equations for B_{dx} and B_{dy} components. After this subtraction the edge effects become much smaller, proportional to $a\nabla\mathbf{M}$, where a is the grid spacing rather than to the large uniform component M_0, allowing calculations with smaller grids.

It is important to note that the average magnetic field produced by any configuration of magnetization in a spherical cell is zero. For concreteness, we examine the average of the z component of the dipolar magnetic field:

$$\langle B_{dz}\rangle = \frac{1}{4\pi R^3/3}\int_V d^3\mathbf{r}\int_V d^3\mathbf{r}' \frac{M_z(\mathbf{r}')(1-3\cos^2\theta_{rr'})}{|\ \mathbf{r}-\mathbf{r}'\ |^3}. \tag{3.23}$$

Reversing the order of integration we have

$$\langle B_{dz}\rangle = \frac{1}{4\pi R^3/3}\int_V d^3\mathbf{r}'\int_V d^3\mathbf{r} \frac{M_z(\mathbf{r}')(1-3\cos^2\theta_{rr'})}{|\ \mathbf{r}-\mathbf{r}'\ |^3} = 0. \tag{3.24}$$

by Eq. 3.21. This means that for spherical geometry, magnetization gradients will not produce an average precession frequency shift, an important point for an EDM experiment

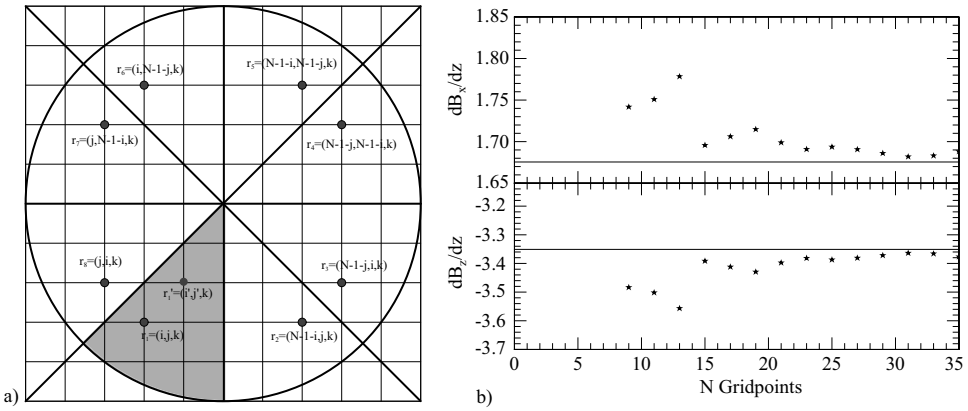

Figure 3.1: a) Schematic showing the 8-fold symmetry of the grid model configuration in the rotating frame. b) Numerically calculated magnetic field gradients per unit gradient of magnetization as a function of the number of grid points N in each dimension. The solid line represents the analytic result $8\pi/15$ and $-16\pi/15$ for transverse and longitudinal gradients respectively.

performed in the small tip angle regime. The scheme for performing an EDM measurement in this regime is discussed further in Chapter 5.

To test the accuracy of the dipolar field calculated with the grid method we compare the results with the analytical solution for a linear gradient of the magnetization, $\mathbf{M} = \mathbf{m}z/R$, for which the dipolar magnetic field is given by Eq. 3.9. In Figure 3.1b) we plot the numerically calculated gradient of the magnetic field near the origin produced by a linear gradient of the magnetization ($m_x^{(1,0)}, m_z^{(1,0)} = 1$), as a function of the number of grid points. Solid lines in the top and bottom panels of this figure are $8\pi/15$ and $-16\pi/15$. We find that for $N = 15$ the gradient calculated by the grid method agrees with the analytic result to better than one percent.

Several steps may be taken to increase the speed of evaluation of the magnetic field. By calculating an array of the dipolar weighting factors

$$w(|\mathbf{r} - \mathbf{r}'|) = \frac{1 - 3\cos^2\theta_{rr'}}{2|\mathbf{r} - \mathbf{r}'|} \tag{3.25}$$

in advance, instead of for each new configuration of the magnetization, we realize an improvement in speed by a factor of approximately 6 in our code. One can realize another

factor of 64 improvement by taking advantage of the azimuthal symmetry of the magnetization and the dipolar fields in the rotating frame for purely longitudinal gradients. Figure 3.1a) shows a slice of the numerical grid. Because of azimuthal symmetry,

$$\mathbf{M}(\mathbf{r}_1) = \mathbf{M}(\mathbf{r}_2) = ... = \mathbf{M}(\mathbf{r}_8) \tag{3.26}$$

and thus

$$\mathbf{B}(\mathbf{r}_1) = \mathbf{B}(\mathbf{r}_2) = ... = \mathbf{B}(\mathbf{r}_8) \tag{3.27}$$

Hence we need only calculate the magnetic field in the shaded piece of the pie, yielding a factor of 8 in speed. Furthermore, because of Eq. (3.26), the contribution to $\mathbf{B}(\mathbf{r}'_1)$ from dipoles located at $\mathbf{r}_i, i = 1...8$ may be written

$$\sum_{i=1}^{8} \mathbf{M}(\mathbf{r}_i) w(|\mathbf{r}'_1 - \mathbf{r}_i|) = \mathbf{M}(\mathbf{r}_1) \sum_{i=1}^{8} w(|\mathbf{r}'_1 - \mathbf{r}_i|) \tag{3.28}$$

reducing the number of multiplication operations by a factor of 8. In addition, the above sum of w factors can be calculated before the start of iterations, but because it depends separately on $\mathbf{r}_1$ and $\mathbf{r}'_1$ instead of only their difference, the memory requirements ($\sim N^6/64$) are significant for grids larger than about 40. Calculating the RHS of Eq. (3.28) from the stored values of $w(|\mathbf{r} - \mathbf{r}'|)$ each time it is needed yields a factor of 3-4 increase in speed instead of a factor of 8.

The largest computational cost is the evaluation of the derivative $d\mathbf{M}/dt$. We use a 3rd order predictor-corrector algorithm for solving the differential equation to minimize the number of derivative evaluations [106]. In the small tip angle regime, we find that approximately 35 time steps per period of gradient oscillation are needed to ensure convergence of the solution.

The subtraction procedure discussed above reduces the error in the calculation of the magnetic field at the edge of the cell from $a\mathbf{M}_0$ to $a\frac{\partial \mathbf{M}}{\partial z}$. We find that this is satisfactory in the small tip angle regime, where the system is inherently stable to small perturbations such as edge effects. However, in the large tip angle regime, small perturbations due to edge effects rapidly grow and spread inward, as a result of dynamical instability. To further

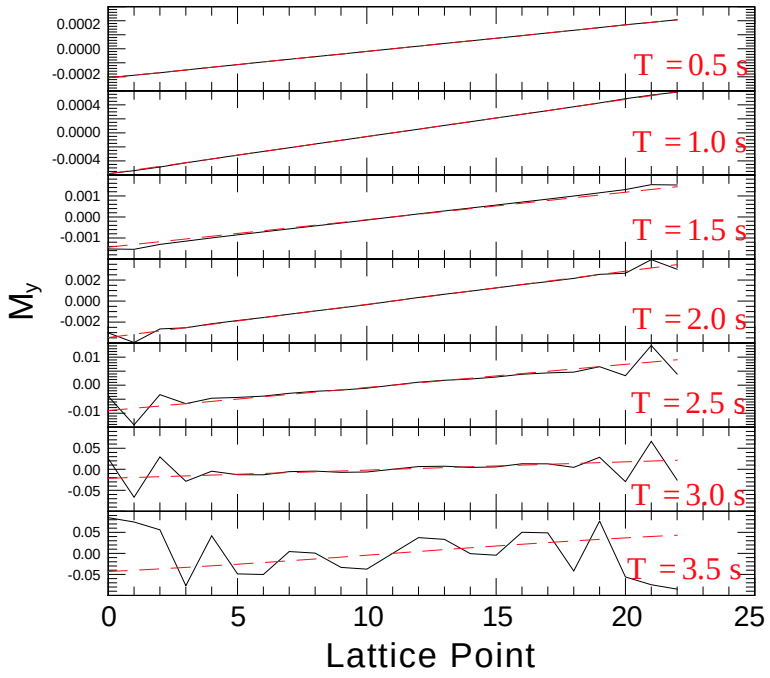

Figure 3.2: Evolution of M_y for a 90° tip angle, with subtraction of a linear gradient of the magnetization (dashed red) and without (solid black). In the latter case, edge effects propagate inward causing the magnetization to crumple prematurely.

improve the accuracy of our numerical solutions, we employ a second subtraction procedure which reduces the errors from truncation effects at the boundary of the cell by reducing the gradient of **M**. Since the contribution to the magnetic field from a linear gradient of the magnetization can be calculated analytically, we fit a linear profile to the magnetization and subtract it before calculating the dipolar field numerically. We then add the contribution from a linear profile to the magnetic field analytically and add the linear profile back to the magnetization. The utility of this procedure is shown in Fig. 3.2 where we compare the solutions to M_y with (dashed line) and without (solid line) the subtraction procedure for a 90° tip angle.

3.3.3 Discrete lattice of spins in the lab frame

This model does not rely on the rotating wave approximation, and hence may be used to test the validity of such assumptions for magnetization comparable to the static B_z field.

Further, it allows us to easily explore the effects of transverse magnetic field gradients, which are crucial to understanding the behavior of the magnetization following a 90° pulse [73].

The model in the lab frame is identical to the rotating frame model except that the dipolar field takes the following form:

$$\mathbf{B_d}(\mathbf{r}) = \sum_{\mathbf{r}' \neq \mathbf{r}} \frac{3\mathbf{n}(\mathbf{n} \cdot \mathbf{M}'(\mathbf{r}')) - \mathbf{M}'(\mathbf{r}')}{|\mathbf{r} - \mathbf{r}'|^3} d\mathbf{r}' \tag{3.29}$$

where $\mathbf{n} = (\mathbf{r} - \mathbf{r}')/|\mathbf{r} - \mathbf{r}'|$ and to cancel edge effects, we make the substitution

$$\mathbf{M}'(\mathbf{r}') = \mathbf{M}(\mathbf{r}') - \mathbf{M}(\mathbf{r}), \tag{3.30}$$

as discussed in the previous section.

In this method we cannot make use of azimuthal symmetry of the magnetization distribution and have to significantly reduce the step size of the time evolution to follow the Larmor precession frequency of the spins. However, the calculations can still be performed in a reasonable time (< 24 h on a 1 GHz Pentium 4) for sufficiently large grids to obtain results in agreement with other models.

3.3.4 Fourier transform technique.

Deville *et al.* [102] noted that the integral operator in Eq. (3.20) is a convolution that can be expressed as a local product in Fourier space:

$$\mathbf{B}_d(\mathbf{k}) = 2\pi/3 \left[\hat{\mathbf{k}} \cdot \hat{\mathbf{z}} - 1\right] \{3M_z(\mathbf{k})\hat{\mathbf{z}} - \mathbf{M}(\mathbf{k})\} \tag{3.31}$$

Following Ref. 16 we transform the magnetization distribution into Fourier space using an FFT, calculate the dipolar magnetic field using Eq. (3.31), transform the field back into real space and advance the magnetization according to Eq. (3.1) using the predictor-corrector algorithm discussed above. The numerical model is run on a grid of N^3 points where N is a power of 2. We typically run the model with N=64 or 128.

Here we investigate evolution of magnetization profiles with large average values, which are not represented accurately by a discrete Fourier transform on a finite grid. Repeated

Fourier transforms can introduce two types of artifacts: distortions at cell boundaries where the magnetization abruptly drops to zero and spurious magnetic fields from "ghost" cells that appear due to implicit periodicity of the Fourier transform. In our calculations the magnetization can be represented to first order by a combination of a constant term and a linear gradient in the $\hat{z}$ direction. Since the dipolar field (3.20) is linear in the magnetization, we can separate the effects of linear magnetization gradients from higher order deviations. Prior to calculating the Fourier transform we subtract from the magnetization profile a constant and linear gradient terms. The remaining magnetization distribution is much smaller and close to zero near the edges, which reduces both the edge and ghost cell effects. To further reduce "ghost" cell effects we use a cell radius R that is smaller than the total grid size N, typically by about 10 points. After calculating the dipolar field created by this distribution in Fourier space we add the magnetic fields created by the linear magnetization gradient using Eq. (3.9).

We also consider the effects of diffusion in this model. Since $\nabla^2\mathbf{M}$ is a local operator there is no speed advantage in calculating it in Fourier space where the boundary conditions cannot be easily applied. To calculate the diffusion contribution in the presence of the boundary conditions we first calculate $\nabla\mathbf{M}$, then set $\mathbf{n}\cdot\nabla M_i = 0$ on the boundary points and then take another derivative to obtain $\nabla^2 M_i$.

3.3.5 Analytical expansion of magnetization

The dipolar interactions can be calculated in a numerically efficient way by expanding the magnetization into a set of basis functions and calculating analytically the dipolar field produced by each of them. In the absence of diffusion the basis functions do not need to satisfy any boundary conditions on the surface. As discussed further in the Appendix, it is convenient to use a Taylor series

$$\mathbf{M} = M_0 \sum_{\alpha,\beta} \mathbf{m}_{\alpha\beta}(t) z^\alpha \rho^{2\beta} / R^{\alpha+2\beta} \tag{3.32}$$

where $\rho = \sqrt{x^2+y^2}$ which is applicable for an azimuthally-symmetric distribution that develops in the presence of longitudinal magnetic field gradients. Then one can symbolically

evaluate the dipolar field integrals for each term and write the dipolar field as

$$B_{d,i} = \sum_{n,m,n',m'} m_i^{nm}(t) b_{nm,i}^{n'm'} z^{n'} \rho^{2m'} / R^{n'+2m'}. \tag{3.33}$$

where $b_{nm,i}^{n'm'}$ are constant coefficients whose evaluation is discussed in the Appendix. It is convenient to note that because of Eq. 3.20

$$b_{nm,x}^{n'm'} = b_{nm,y}^{n'm'} = (-1/2) b_{nm,z}^{n'm'} = b_{nm}^{n'm'}. \tag{3.34}$$

After obtaining all coefficients $b_{nm}^{n'm'}$, for $n + 2m < 40$ and $n' + 2m' < 40$, the expansion for the magnetization and dipolar magnetic field are inserted into the Bloch equations:

$$\begin{aligned} \sum_{\alpha\beta} \frac{dm_i^{\alpha\beta}}{dt} z^\alpha \rho^{2\beta} / R^{\alpha+2\beta} &= \epsilon_{ijk}\gamma \sum_{rs} m_j^{rs} z^r \rho^{2s} / R^{r+2s} \times \\ &\quad \sum_{n'm'} \left[g^{n'm'} \delta_{k3} + \sum_{nm} m_k^{nm} b_{nm,k}^{n'm'} \right] \times \\ &\quad z^{n'} \rho^{2m'} / R^{n'+2m'} \end{aligned} \tag{3.35}$$

where $g^{n'm'}$ are the coefficients in the Taylor expansion of of the z component of the externally applied magnetic field. Equating coefficients of equal powers of $z^\alpha \rho^{2\beta}$ for $n' = \alpha - r$, $m' = \beta - s$ we arrive at the following set of coupled differential equations

$$\frac{dm_i^{\alpha\beta}(t)}{dt} = \gamma \sum_{n,m,r,s} m_j^{rs}(t) (b_{nm,k}^{\alpha-r,\beta-s} m_k^{nm}(t) + g^{\alpha-r,\beta-s}) \epsilon_{ijk}. \tag{3.36}$$

one for each basis function $z^\alpha \rho^{2\beta}$ and each vector index. We numerically solve this large set of equations using either Mathematica or a homegrown differential equation solver in FORTRAN.

The case $n = 1$ and $m = 0$ is discussed at length in Section 3.2, The expansion $n+2m \leq 4$ was also investigated in Ref [101]. This model could explain an asymmetry in the signals between the two SQUIDs, discussed further in Chapter 4, but the significance of the higher order terms grew rapidly so that only one or two periods of oscillation could be followed in the small tip angle regime. Including higher-order gradients, up to z^{40}, improves the accuracy of the solution and allows us to observe the evolution for many oscillations. In addition, the extra terms in the series rapidly improve the convergence to the behavior

predicted by the linear model when $gR/M_0 \ll 1$. However, we find that the solution eventually diverges due to rapid growth of highest-order terms. While the Taylor series expansion is conceptually simple and allows us to obtain the coupling coefficients b_{nm}^{kl} in closed form, it is not necessarily an ideal basis for this problem when $gR/M_0 \approx 1$ and is somewhat akin to expanding $\sin(x)$ in a Taylor series. Increasing the number of terms in the expansion merely delays the onset of the divergence.

3.3.6 Extraction of data from numerical calculations

In order to compare the results of our calculations with the experiment it is necessary to accurately model the measurement of the magnetization gradients using two SQUID detectors. The inset of Fig. 2.1 shows a schematic of the relative orientation between the SQUID detectors, cell, magnetization and applied field. The signal in each SQUID is proportional to the flux through a square pickup coil. To calculate the amount of flux going through the pick-up coils we use the equality of mutual inductances and integrate the magnetic field produced by a current flowing through the pick-up coil over the volume of the cell. This technique is convenient because the magnetic field produced by a square loop of current can be calculated in closed form, rather than numerically calculating the magnetic field produced by a complicated magnetization distribution. The magnetic flux through the SQUID pickup coil due to a dipole $\mathbf{m} = I_d \mathbf{A}_d/c$ where I_d is the effective current flowing through a loop of area $\mathbf{A}_d$ can be written

$$\Phi_c = L I_d \tag{3.37}$$

where L is the mutual inductance between the SQUID pickup coil and the dipole moment. Likewise, the flux through the dipole from a current I_c flowing through the pickup coil can be written $\Phi_d = L I_c = \mathbf{B}_c \cdot \mathbf{A_d}$. Thus we can express the mutual inductance as $L = \mathbf{B}_c \cdot \mathbf{A_d}/I_c = \frac{\mathbf{B}_c}{I_c} \cdot \frac{\mathbf{m}c}{I_d}$ and write the total flux through the SQUID pickup coil

$$\Phi_c = c \int_V \frac{\mathbf{B}_c(\mathbf{r}) \cdot \mathbf{M}(\mathbf{r})}{I_c} d^3\mathbf{r}. \tag{3.38}$$

The magnetization in the lab frame, written in terms of the rotating frame components is

$$\mathbf{M}_{lab} = (M_x \cos\omega t - M_y \sin\omega t, M_x \sin\omega t + M_y \cos\omega t, M_z). \tag{3.39}$$

Inserting Eq. 3.39 into Eq. 3.38 we see that the flux through each SQUID can be separated into AC and DC components. The AC flux in each SQUID has in-phase and out-of-phase components $\Phi_{in}^{(i)}$ and $\Phi_{out}^{(i)}$ given by

$$\Phi_{in}^{(i)} = \int_V (M_x(\mathbf{r})B_x^{(i)}(\mathbf{r}) + M_y(\mathbf{r})B_y^{(i)}(\mathbf{r}))d^3\mathbf{r} \tag{3.40}$$

$$\Phi_{out}^{(i)} = \int_V (M_x(\mathbf{r})B_y^{(i)}(\mathbf{r}) - M_y(\mathbf{r})B_x^{(i)}(\mathbf{r}))d^3\mathbf{r} \tag{3.41}$$

$$\tag{3.42}$$

where $\mathbf{B}^{(i)}(\mathbf{r})$ is the magnetic field produced by each SQUID pick-up coil with one unit of current flowing through it. The amplitude of the total AC signal $\Phi_{tot}^{(i)}$ is

$$\Phi_{tot}^{(i)} = \sqrt{\Phi_{in}^{(i)\,2} + \Phi_{out}^{(i)\,2}} \tag{3.43}$$

while the phase difference between the SQUID signals is given by

$$\Delta\phi = \arctan(\Phi_{out}^{(1)}/\Phi_{in}^{(1)}) - \arctan(\Phi_{out}^{(2)}/\Phi_{in}^{(2)}). \tag{3.44}$$

We now address the linearity of the phase difference between the SQUID signals and the first order gradients of the magnetization. Assume that the magnetization configuration can be well described by $\mathbf{M} = M_0\{1, m_y\frac{z}{R}, m_z\frac{z}{R}\}$ and that $m_y, m_z \ll 1$. Referring to the coordinate system in the inset of Fig. 2.1, we note that the y component of the magnetic field $B_y^{(i)}$ produced by either pickup loop is asymmetric with respect to y. Since the above magnetization distribution is symmetric with respect to the y coordinate, the second term in Eq. 3.40 and the first term in Eq. 3.41 are both zero. Therefore, since $m_y \ll 1$, $\Phi_{out}^{(i)} \ll \Phi_{in}^{(i)}$ and we can approximate Eq. 3.44 as

$$\Delta\phi = \frac{\Phi_{out}^{(1)} - \Phi_{out}^{(2)}}{\Phi_{in}} \tag{3.45}$$

where by symmetry, $\Phi_{in}^{(1)} = \Phi_{in}^{(2)} = \Phi_{in} = \int_V M_0 B_x^{(i)}(\mathbf{r})d^3\mathbf{r}$, independent of m_y. Referring again to the coordinate system in Fig. 2.1 we focus on the magnetic field B_x produced by

the SQUID pickup coils. Note that the x and y dependence of this component is identical for each pickup coil, while the z dependence of B_x has the opposite sign for each coil. Thus to first order in a Taylor expansion we can write $B_x^{(1)} = p + q_x x + q_y y + q_z z + ...$ and $B_x^{(2)} = p + q_x + q_y y - q_z z ...$ Hence Eq. 3.41 becomes

$$\Phi_{out}^{(i)} = -m_y \int_V \frac{z}{R}(p + q_x x + q_y y \pm q_z z) d^3\mathbf{r}. \tag{3.46}$$

On taking the difference between the two phases in Eq. 3.46 the only term that survives is the term proportional to q_z. Hence, for small gradients of the magnetization, the phase difference is,

$$\Delta\phi = 2\frac{m_y}{\Phi_{in}} \int_V \frac{q_z z^2}{R} d^3\mathbf{r} = \xi m_y, \tag{3.47}$$

directly proportional to the magnetization. The dimensionless parameter ξ depends purely on geometry and for our setup, $\xi \simeq 0.5$. To verify these conclusions, we numerically calculate the phase difference between the SQUID signals as a function of m_y and plot the results in Fig. 3.3. We see that for $m_y < 0.3$, the phase difference is proportional to the gradient m_y.

3.4 Discussion of Simulations

Since the linear model suggests that the behavior in the small tip angle regime, ($\alpha < 35°$), is radically different from the large tip angle regime, we will discuss these two different areas of parameter space separately.

3.4.1 Small tip angles

Parameters of the Bloch equations

Our simulations depend on five parameters: the magnitude of the applied gradient g in G/cm, the magnetization density M in G, the radius of the cell R in cm, the diffusion constant D in cm^2/s and the tip angle α in radians. To understand the short term behavior (<20 sec) after the initial tipping pulse we can neglect the effects of diffusion and relaxation.

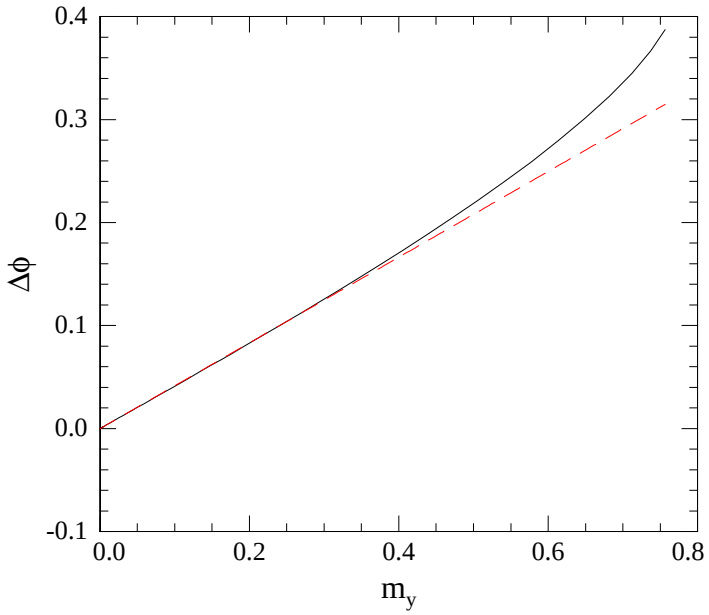

Figure 3.3: The solid line shows the numerically calculated phase difference between SQUID signals as a function of the gradient m_y and the dashed line shows a linear fit to the the region for which $m_y < 0.3$

We find that for small tip angles and $gR/M_0 \ll 1$ the phase oscillations are accurately described by a $\sin(\omega t)$ function and their frequency can be determined unambiguously. For $gR/M_0 \approx 1$ the oscillations are not quite sinusoidal, as shown in Figure 3.5. Even in that case we find that by performing a non-linear fit we can find the frequency of oscillations with a systematic uncertainty of less than 1-2% if the fitting range is greater than 2 oscillation periods.

It is not initially clear that the RWA is sufficiently accurate, since the ratio of dipolar fields to applied DC magnetic field can exceed 1/10. To check the validity of the RWA, we examine the frequency of phase oscillations as a function of the magnetization. We find that for $M_0 \leq B_0/10$ the changes in the frequency of the oscillations is only a few tenths of a percent, and hence the RWA is valid in our regime.

Within the RWA scaling arguments allow us to reduce the number of independent parameters by two for the short term behavior of the system. We use the tip angle and relative

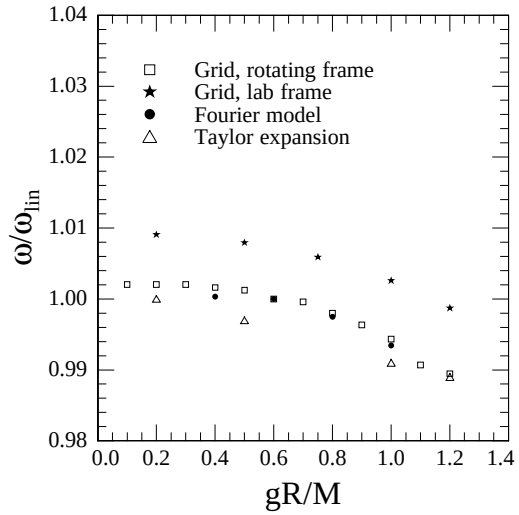

Figure 3.4: The ratio of frequency of phase oscillations to the predictions of the linear model obtained with different methods as a function of gR/M for a small tip angle of 0.05 rad.

gradient gR/M_0 as the two dimensionless parameters that define a family of solutions.

Short term evolution of the phase oscillations

To explore the effects of magnetization gradients higher than first order for small tip angles at large gR/M_0 we compare the frequency of simulated or experimental oscillations to the frequency of oscillations of the linear model given by $\omega = i\beta$. Since the linear model suggests that the frequency of the phase oscillations depends on the tip angle α only quadratically for small α, we set α to a small value $\alpha = 0.05$ and investigate the oscillation frequency as a function of gR/M_0 as shown in Figure 3.4. For small gradients, $gR/M_0 \ll 1$, all models agree with the linear model to within a couple tenths of a percent, except for the grid model in the lab frame which has a constant offset because it uses a relatively small number of grid points.

The case in which $gR/M_0 \approx 1$ is the most problematic because higher order gradients become important. The ratio of the second to first order gradient grows linearly with gR/M_0, $m_2/m_1 \approx 2 \times gR/M_0$, indicating the importance of higher order gradients of the magnetization at large gR/M_0. It is interesting to superimpose the solutions of the grid,

Fourier and analytic expansion models for this case. In Fig. 3.5 we show solutions from all models for $gR/M_0 = 1$. A close agreement for the first period of oscillation provides a verification of the correctness of our codes. Observed deviation for later times is due to numerical accuracy of implemented methods. We checked that as the number of terms in the Taylor expansion grows the numerical results are virtually unchanged until the point where the Taylor expansion breaks. Similarly, for the grid models we also find close agreement for $N = 25$ and $N = 41$ and the results of the Fourier model are unchanged for $N = 64$ or 128. Decreasing the time step by a factor of two produces imperceptible change in any of the models.

In Figure 3.6 we show the dependence of frequency on the tip angle for $gR/M_0 = 0.2$. The predictions of our models agree well with the linear model for small tip angles, but some deviation is observed for larger tip angles. The linear model predicts that the gradients should oscillate for tip angles smaller than $35^\circ \approx 0.6$ rad and grow exponentially for larger angles. However, in each of the higher order numerical models, the solution becomes unstable for tip angles greater than about 0.3 radians. Experimental observations indicate that instability can occur for tip angles as small as 0.15 rad. The tip angle corresponding to the onset of the instability is approximately inversely proportional to the magnetization. We leave a more detailed exploration of the onset of instability with respect to the tip angle for another study.

Long term evolution of the phase oscillations.

For time scales on the order of many hundreds of seconds diffusion and relaxation become relevant. In the limit of small tip angles and small gR/M_0, the magnetization profile is dominated by an oscillating first order gradient in the $\hat{z}$ direction of the $\hat{y}$ and $\hat{z}$ components of the magnetization. The longitudinal relaxation time in our experiment is close to $T_1 =$ 1800 seconds measured in other experiments, indicating that depolarization on the cell walls is very small. In the presence of diffusion and the non-relaxing cell walls, the boundary condition is $d\mathbf{M}/dr|_{r=R} = 0$, essentially "rounding off" the linear gradient at the cell walls.

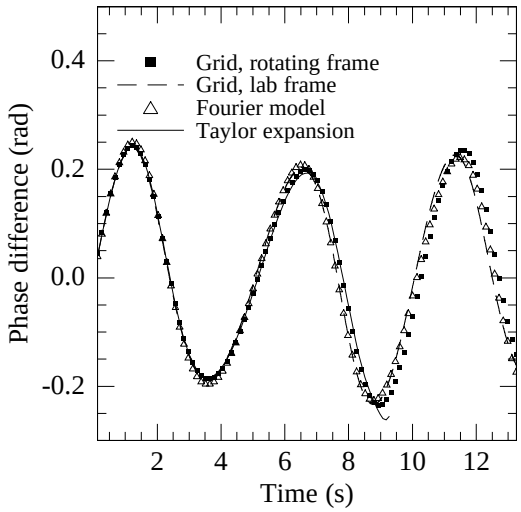

Figure 3.5: Comparison of the phase oscillations from all models for $gR/M = 1$ and tip angle $\alpha = 0.05$ rad. The models agree closely for the first period of oscillation, but start to deviate slightly for the second period. The analytical expansion model breaks down abruptly (a sharp turn down) right after the second minimum.

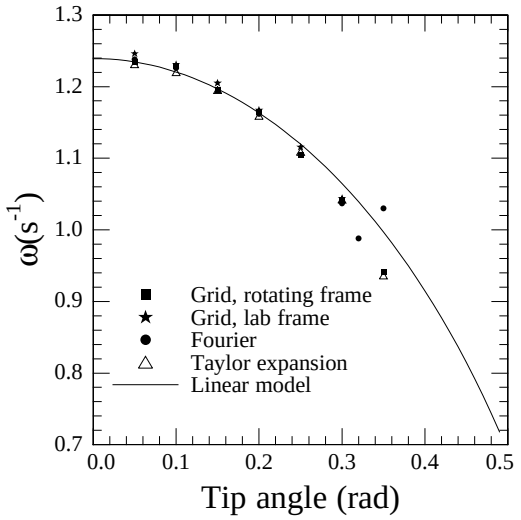

Figure 3.6: The dependence of the frequency of the phase oscillations obtained with different models compared with the prediction of the linear model as a function of the tip angle with $gR/M_0 = 0.2$ and $M_0 = 100\mu$G.

We solve the diffusion equation in the presence of an oscillating magnetization gradient using Laplace transform method and expanding the magnetization in terms of spherical Bessel functions and spherical harmonics. The length scale for the distortion of the linear magnetization gradient is given by $l_D = \sqrt{D/\omega_{lin}}$ and for our experimental conditions $l_D \sim 3 \times 10^{-3}$cm. Thus, only a very thin layer near the surface of the cell is affected by diffusion. The magnetic dipolar fields created by this distortion result in the decay of the phase oscillations.

The modelling of the diffusion effects is very numerically demanding. We are interested in the solution of the problem in the regime $l_D \ll R$. On the other hand, to accurately describe the effects of diffusion on a discrete grid we need the grid spacing to be much smaller than l_D. These requirements result in an inequality $R \gg l_D \gg R/N$ which cannot be easily satisfied unless N is large. We performed the calculations using the Fourier method with $N = 128$ and using artificially increased values of the diffusion constant so both inequalities are approximately satisfied. We found that the rate for the decay of the phase oscillations τ^{-1} scales approximately with D/R^2. Numerically, we obtain $\tau^{-1} \sim 7D/R^2$. This can be compared with the decay rate $\tau_1^{-1} = 4.33D/R^2$ of the first diffusion eigenmode with $l = 1$ spherical harmonic, which corresponds to an approximately linear magnetization gradient.

The measurements of the diffusion constant of liquid Xe are also somewhat uncertain, with numbers ranging from $D = 2 \times 10^{-5}$ cm^2/ sec to $D = 4 \times 10^{-5}$ cm^2/ sec, [46, 107, 108] at our temperature. We estimate that the decay of the phase oscillations due to diffusion has a time constant $\tau \sim 2000$ seconds with a factor of 2 uncertainty.

3.4.2 Large tip angles

As discussed in the introduction and earlier in the chapter, the large tip angle regime is particularly interesting for an EDM experiment. At large tip angles, the magnetization develops a dynamical instability, such that the response to any perturbation[91] grows exponentially. If the perturbation is a purely linear longitudinal magnetic field gradient, the instability leads to exponential growth of the linear gradients of the magnetization. In

principle, this can lead to enormous gains in the sensitivity to a small magnetic field gradient. For a magnetization of 100 μG, $\beta = 1.75$ s^{-1} so that the gain parameter $G = \sinh(\beta t)/\beta t)$ is 360 at 5 seconds. Since the timescale we are concerned with in this regime is so short, we do not consider the effects of diffusion or relaxation.

This almost seems too good to be true. Is it really possible to realize such spectacular amplification of first order gradients? In particular, will the growth of high order gradients spoil this amplification? In brief, the answer is yes, high order gradients will certainly have an impact on the amplification of first order longitudinal gradients, however, it is still possible to realize substantial improvements in sensitivity.

We first examine the full solution to the numerical models in the presence of an applied linear longitudinal gradient as well as other additional transverse or other higher order gradients. Since our goal is to achieve very high sensitivity to a small first order longitudinal magnetic field gradient g, we generally assume that it is smaller than other gradients that are not measured directly. We find that the presence of transverse gradients and higher order longitudinal gradients as well as initial magnetization inhomogeneities cause an abrupt non-linear decay of the overall magnetization. The time t_c until the collapse of the magnetization, which depends on the size of the inhomogeneities relative to M_0, limits the achievable gain to $\sinh(\beta t_c)/\beta t_c$. Inhomogeneities of the applied field symmetric with respect to the z direction, such as transverse linear gradients or second order longitudinal gradients, do not change the evolution of $\Delta\phi$, which remains proportional to g before the collapse of the magnetization, as shown in Figs. 3.7, 3.8, and 3.9. Thus, despite the rapid growth of higher order gradients, we find that it is still possible to achieve substantial gains in sensitivity to a small first order longitudinal gradient.

Higher order z-odd longitudinal gradients do generate a phase difference as shown (Fig. 3.10b). In this figure the squares represent the evolution of the phase difference in the presence of small linear longitudinal gradient g as well as a larger third order longitudinal gradient g_3. The squares represent the phase difference for evolution in the presence of a third order gradient g_3 and $g = 0$. The triangles represent the difference of these two, which

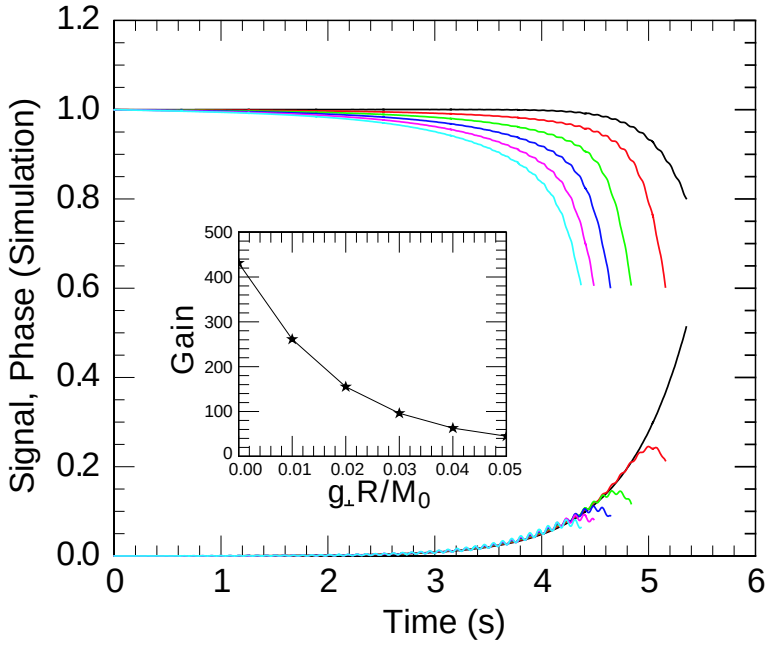

Figure 3.7: Results of simulations for $M_0 = 100\,\mu$G,a small longitudinal field gradient $g_\parallel = 0.1\,\mu$G/cm and a series of relatively large transverse $g_\perp = 0, 2, 4, 6, 8, 10\,\mu$G/cm. (black,red,green,dark blue,purple,light blue respectively). Despite the presence of substantially larger transverse gradients, a small longitudinal gradient leads to the exponential growth of the phase difference between the SQUIDs as predicted by Eq.3.12 until the overall SQUID signal begins to decay. Inset is the gain when the signal reaches 90% of its initial value as a function of $g_\perp R/M_0$

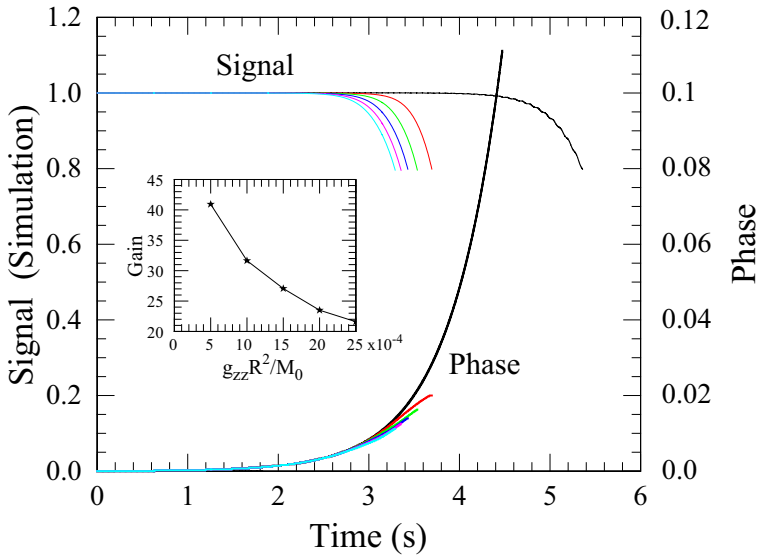

Figure 3.8: Impact of second order longitudinal gradients on growth of phase difference and signal. Inset is the gain function for longitudinal linear gradients at the time of the collapse of the signal

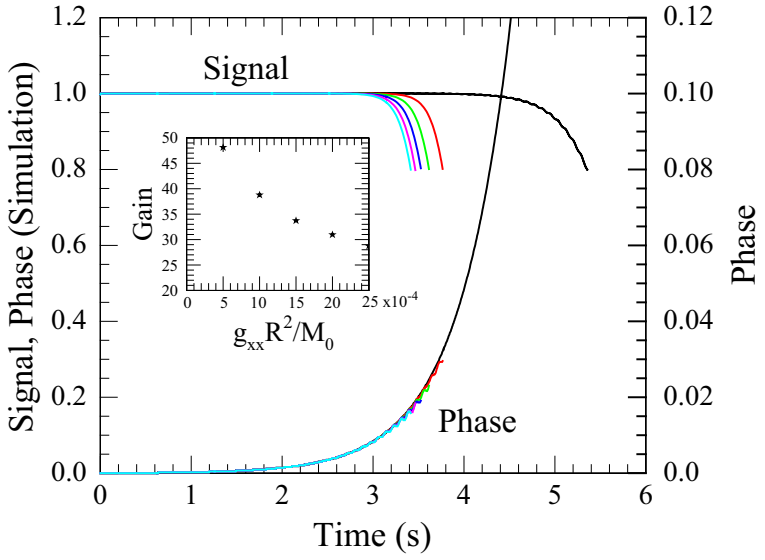

Figure 3.9: Impact of second order transverse gradients on growth of phase difference and signal. Inset is the gain function for longitudinal linear gradients at the time of the collapse of the signal

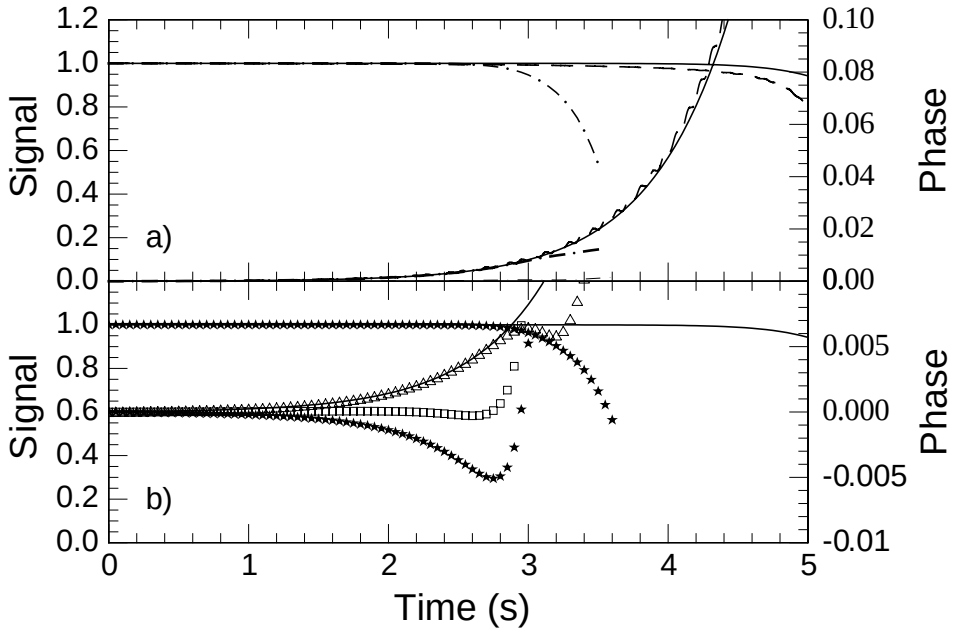

Figure 3.10: Numerical simulations of the SQUID signal (left axis) and the phase difference between SQUIDs (right axis) for $M_0 = 100\,\mu$G and a small longitudinal field gradient $g = 0.1\,\mu$G/cm (solid lines). a) An additional larger transverse gradient $g_\perp = 2\,\mu$G/cm (dashed line) or a second order longitudinal gradient $g_2 = 1\mu$G/cm^2 (dash-dot) do not affect the phase difference until the SQUID signal begins to decay. b): Effects of an additional third order longitudinal gradient $g_3 = 0.8\,\mu$G/cm^3 (squares). Stars show the phase evolution in the presence of g_3 but for $g = 0$. The difference between the phase for $g = 0.1\,\mu$G/cm and $g = 0$ (triangles) follows the solid line corresponding to the pure linear gradient g until the magnetization begins to collapse. Hence, the third order gradient generates a background phase signal that can be subtracted if one is looking for a small change in g between successive measurements.

evolves as predicted by the linear model. Hence, the contributions of different magnetic field gradients to the phase difference add linearly as long as $\mathbf{m}^{(i,k)} \ll 1$ and the effects of higher order odd gradients can be subtracted if they remain constant. This subtraction breaks down when the gradients of the magnetization become large, however until that time, the phase difference can be used as an accurate measure of the applied gradient g.

To understand the growth of high order magnetization gradients it is instructive to examine the analytic expansion in first order perturbation theory, where we assume all magnetization gradients are small and we neglect the coupling between high order gradients.

λ	$\sum_{ij} u_k^{ij} z^i \rho^{2j}$
0	0.488603
3.35103	$1.09255\, z$
-2.73628	$0.904082 - 1.99895\, \rho^2 - 0.522501\, z^2$
5.12987	$0.660289 - 0.42662\, \rho^2 - 2.4482\, z^2$
-0.545181	$2.3645\, z - 5.87619\, \rho^2\, z - 1.5997\, z^3$
6.13023	$2.79958\, z - 1.75235\, \rho^2\, z - 5.36412\, z^3$

Table 3.1: Eigenvalues and eigenmodes of the magnetic field operator in cylindrical coordinates.

In this case $M_x = M_0$ is constant and Eq. 3.36 reduces to

$$\begin{aligned} \frac{dm_y^{\mu\nu}(t)}{dt} &= -\gamma M_0 \sum_{ij} b_{ij}^{\mu\nu} m_z^{ij}(t) \\ \frac{dm_z^{\mu\nu}(t)}{dt} &= -\frac{1}{2}\gamma M_0 \sum_{ij} b_{ij}^{\mu\nu} m_y^{ij}(t) \end{aligned} \tag{3.48}$$

For convenience, we assume that M_0 and γ are both 1. A magnetization gradient m^{ij} generates magnetic field gradients only of equal or lower order, $b_{ij}^{\mu\nu} = 0$ for $\mu + 2\nu > i + 2j$. Hence if we include only (and all) terms in the Taylor expansion such that $\mu + 2\nu \leq N_{max}$, the system is closed in the sense that if we start with some configuration of the magnetization with terms limited by $\mu + 2\nu \leq N_{max}$, the system evolves within this subspace.

We now write Eqns. 3.48 in matrix form

$$\frac{d}{dt}\begin{pmatrix} m_y^{\mu\nu} \\ m_z^{\mu\nu} \end{pmatrix} = \begin{pmatrix} 0 & -b_{ij}^{\mu\nu} \\ -b_{ij}^{\mu\nu}/2 & 0 \end{pmatrix} \begin{pmatrix} m_y^{ij} \\ m_z^{ij} \end{pmatrix} \tag{3.49}$$

It is straightforward to show that the eigenvalues of the magnetic field operator in Eq. 3.49 are $\beta_{\pm k} = \pm\lambda_k/\sqrt{2}$ and the eigenvectors are $\{u_k^{ij}, \pm u_k^{ij}/\sqrt{2}\}$ where λ_k and u_k are the eigenvalues and eigenvectors of $-b_{ij}^{\mu\nu}$, $-bu_k = \lambda_k u_k$. We obtain the eigenvectors u_k and λ_k using Mathematica. For reference, we present the eigenvalues λ and the functions $\sum_{ij} u_k^{ij} z^i \rho^{2j}$ for $N_{max} = 3$ in Table 3.1. With the exception of the two lowest order eigenmodes which correspond to uniform or purely linear gradients of the magnetization, the eigenmodes are complicated combinations of the basis functions of the Taylor expansion $z^n \rho^{2m}$ for $n + 2m \leq N_{max}$. Before proceeding we note that with the appropriate normalization,

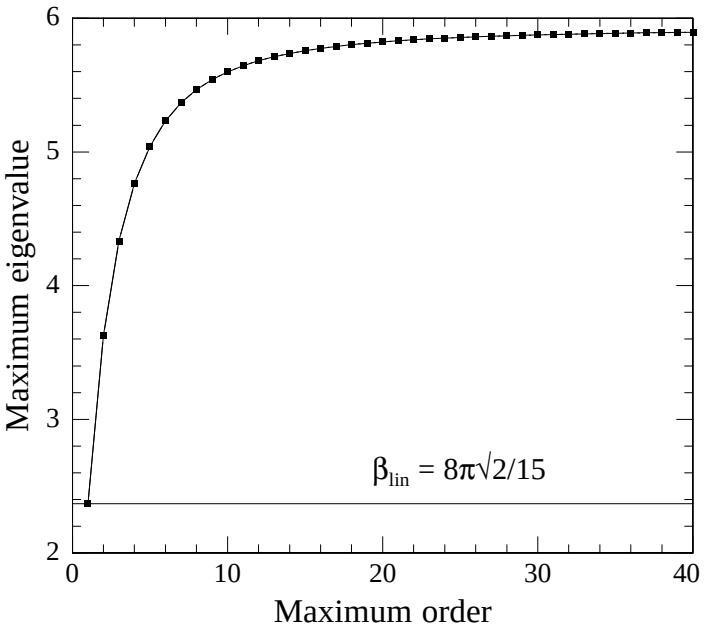

Figure 3.11: Maximum eigenvalue of the time evolution operator as a function of the maximum order of the Taylor expansion.

the functions $\sum_{ij} u_k^{ij} z^i \rho^{2j}$ are orthonormal when integrated over the unit sphere:

$$\int_V u_k^{ij} z^i \rho^{2j} u_l^{nm} z^n \rho^{2m} d^3\mathbf{x} = \delta_{kl}. \tag{3.50}$$

This fact can be verified numerically. Presumably, a better choice of basis functions would elucidate this result, however we will leave this for a later discussion.

In Fig. 3.11 we plot the maximum eigenvalue β_{max}, corresponding to the fastest growing mode, as a function of the maximum order of the Taylor expansion. For $N_{max} = 1$ corresponding to only linear terms in the Taylor expansion, we naturally recover the growth rate given by the linear model $8\pi\sqrt{2}/15$ for $M_0 = \gamma = 1$. We see that the growth rate of higher order gradients seems to approach an asymptote about 2.5 times greater than the growth rate of linear gradients.

Given the orthogonality condition 3.50, the time evolution of the system is particularly simple if we express the magnetization as a sum of the eigenmodes of the system

$$\mathbf{M} = \sum_k a_{\pm k}(t)\mathbf{v}_{\pm k} \tag{3.51}$$

where

$$\mathbf{v}_{\pm k} = (\hat{\mathbf{y}} + \hat{\mathbf{z}}/\sqrt{2}) \sum_{ij} u_k^{ij} z^i \rho^{2j}. \tag{3.52}$$

Here we neglect the x component of the magnetization because it is unchanged in this perturbative analysis. In this basis, the Bloch equations are simply

$$\frac{da_{\pm k}(t)}{dt} = \beta_{\pm k} a_{\pm k}(t) \tag{3.53}$$

If the initial condition is

$$\mathbf{M}(t=0) = \sum_{\pm k} a_{\pm k}(0) \mathbf{v}_{\pm k} \tag{3.54}$$

the magnetization at a later time is simply

$$\mathbf{M}(t) = \sum_{\pm k} a_{\pm k}(0) e^{\beta_{\pm k} t} \mathbf{v}_{\pm k}. \tag{3.55}$$

To make connection with experimental observables, we note that the SQUID signal is approximately equal to the first moment of the y component of the magnetization $p = \int_V z M_y(t) d^3\mathbf{x}$. Inserting the solution 3.55 into the expression for p

$$p(t) = \int_V z \left(\sum_{\pm j} a_{\pm j}(0) e^{\beta_{\pm j} t} (\mathbf{v}_{\pm j})_y \right) d^3\mathbf{x} \tag{3.56}$$

Since z is proportional to $v_{\pm 1}$ which are orthogonal to all other $v_{\pm k}$, the only terms that contribute are the lowest order terms $v_{\pm 1}$:

$$p(t) = \sum_{\pm 1} a_{\pm 1}(0) e^{\beta_{\pm 1} t} \int_V z (\mathbf{v}_{\pm 1})_y d^3\mathbf{x}. \tag{3.57}$$

This is an interesting result. Regardless of the initial condition of the magnetization, the first moment of the magnetization will always grow with a time constant $\beta_{\pm 1}$ given by the linear model.

Until now we have neglected any driving term such as an applied gradient of the magnetic field and addressed the behavior of the magnetization for some initial condition specified by Eq. 3.54. It should be noted that the solution for an applied gradient can obtained by supplying initial conditions on the derivatives

$$\frac{\mathbf{a}_{\pm \mathbf{k}}}{dt}\Big|_{t=0} = g_{\pm k} \tag{3.58}$$

where $g_{\pm k}$ are the coefficients in a Taylor expansion of the applied magnetic field in terms of the basis functions 3.52. The solution to Eq. 3.53 is

$$a_{\pm k}(t) = \frac{g_{\pm k}}{\beta_{\pm} k} e^{\beta_{\pm k} t}. \tag{3.59}$$

Hence we conclude that the first moment of the magnetization also grows exponentially in response to the first moment of the applied field with a time constant $\beta_{\pm 1}$. To recover the equations for the growth of gradients in response to a linear longitudinal applied field gradient given in Section 3.2, we note that a purely longitudinal linear field gradient is a linear combination of $\mathbf{v}_{+1}$ and $\mathbf{v}_{-1}$.

The SQUID signal is not exactly proportional to the first moment because the difference between the magnetic fields generated by the SQUID signals is not exactly a linear function of z. It turns out that it is a pretty good approximation for our geometry though. As discussed previously, the phase difference between the two SQUID signals is proportional to

$$\int_V M_y B_x^{SQUID} d^3\mathbf{x}. \tag{3.60}$$

In Fig. 3.12 we plot the numerically calculated contribution to the phase difference from each eigenmode $\int_V v_{k,y} B_x^{SQUID}$ as a function of the order of the eigenmode, the maximum of $n + 2m$ in the Taylor expansion. It is apparent that first eigenmode corresponding to linear gradients of the magnetization generates a phase difference 35 times greater than the next z-odd eigenmode. So, until the next z-odd mode becomes many times greater than the first eigenmode, the phase difference between the SQUID signals will grow with a time constant given by the linear model $\beta = M_0 \gamma 8\pi\sqrt{2}/15$. With a clever choice of geometry it may be possible to completely suppress the SQUID sensitivity to the higher order modes. A final point to make is that Eq. 3.60 is linear in the magnetization. If one is looking for a modulation of the SQUID phase difference in response to an oscillating linear gradient in the presence of other gradients, as long as the other gradients remain constant, their contribution to the SQUID phase difference may be subtracted off. This is in aggreement with the results of the full solutions of the numerical models discussed previously.

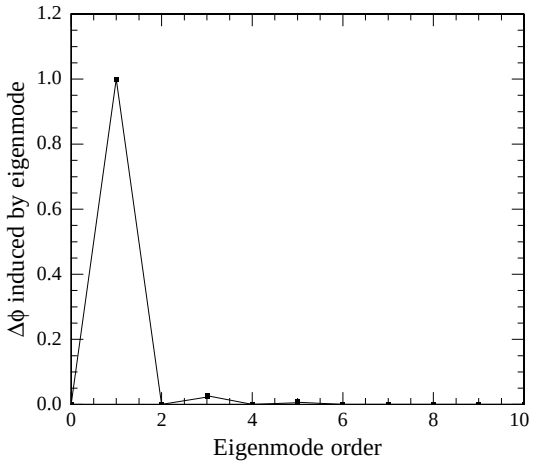

Figure 3.12: Magnitude of phase difference due to various eigenmodes as a function of the order of the eigenmode

Hence, the phase difference $\Delta\phi$ can be used to measure a very small linear gradient g in the presence of larger inhomogeneities as long as all magnetic field and magnetization inhomogeneities are much smaller than M_0. The ultimate sensitivity is limited by the fluctuations of the gradients between successive measurements. In addition to the fluctuations of g, which is the quantity being measured, the phase difference will be affected by the fluctuations in the initial magnetization gradients $m_y^{(1,0)}$ and $m_z^{(1,0)}$ and, to a smaller degree, higher order z-odd gradients of the magnetic field and the magnetization. In particular, fluctuations of $m_y^{(1,0)}$ and $m_z^{(1,0)}$, either due to spin-projection noise or experimental imperfections, set a limit on the magnetic field gradient sensitivity on the order of $\delta g = 8\sqrt{2}\pi M_0 \delta m_y^{(1,0)}/15R$ and similar for $\delta m_z^{(1,0)}$. Thus to achieve high gains in sensitivity to a small longitudinal linear magnetic field gradient, it will be necessary to reduce all magnetic field gradients and ensure that the initial magnetization of ^{129}Xe is uniform. The implications of the dynamic instability at large tip angles to the measurement of an EDM are discussed further in Chapter 5.

3.5 Cell deformations

Our studies did not focus on the effects of cell deformations, as this is not an easy parameter to vary experimentally, and hence we will discuss this only briefly. Treating the effects of cell deformations with the grid models that calculate the magnetic field directly is difficult because the subtraction procedure discussed in Section 3.3.2 cannot be employed for a non-spherical cell. Without the subtraction procedure, edge effects rapidly propagate inward, destroying the solution. The Fourier model seems to have less susceptibility to edge effects. However, the magnetic fields created by small deformations for a uniform polarization can be calculated analytically, and for certain types of deformations, the effects of the dipolar fields are easy to analyze.

We characterize cell deformations in terms of linear combinations of spherical harmonics $S_{lm}(\theta,\phi) = \frac{1}{2i}(Y_{lm}(\theta,\phi) \pm Y_{l-m}(\theta,\phi))$ since they form a complete basis on the surface of a sphere. The magnetic field can be calculated using Eq. 3.3. We assume here that the magnetization is uniform, and hence the first term may be neglected. We parameterize the surface as $R(\theta,\phi) = R(1+\epsilon S_{lm}(\theta,\phi))$. To calculate the magnetic field, we expand the integrand in the last term of Eq. 3.3 to first order in ϵ. We find that $l = 1$ deformations due not generate any magnetic field, as this corresponds to a simple offset of the spherical cell from the origin. $l = 2$ deformations generate only homogeneous magnetic fields. It is straightforward to show that for a $S_{2,0}$ deformation, the magnetic field is

$$\mathbf{B}_{20} = 2\epsilon\frac{\pi}{\sqrt{5}}\{-M_x, -M_y, 2M_z\}. \tag{3.61}$$

This produces a frequency shift $\delta\omega = \frac{6\gamma\epsilon\pi M_z}{\sqrt{5}}$. All other quadrupolar deformations produce magnetic fields that average to zero in the rotating frame and hence produce no frequency shifts.

$l = 3$ deformations generate only linear gradients of the magnetic field. For example, the magnetic field in the rotating frame generated by an $l = 3, m = 0$ deformation is

$$\mathbf{B}_{30} = \epsilon M_0\frac{z}{R}\sqrt{\frac{\pi}{7}}\{-6\sin\alpha, 0, 9\cos\alpha\}. \tag{3.62}$$

Neglecting the effects of other gradients of the magnetization, this will generate a small gradient of the y component of the magnetization

$$\frac{dm_y^{(1,0)}}{dt} = 15\gamma\epsilon\sqrt{\frac{5}{7}}M_0 \sin\alpha\cos\alpha \tag{3.63}$$

Conveniently, this is zero for $\alpha = \pi/2$ and to first order in small parameters, does not have an effect on the evolution of the gradients. For small tip angles, it will slightly modify the oscillation frequency of the gradients.

3.6 Conclusions

We have developed several new numerical tools to study the effects of long range dipolar fields. Most useful for other applications are: (1) A method for compensating for edge effects in a spherical geometry due to the finite grid size and the use of the azimuthal symmetry of the problem, decreasing computation time by up to a factor of 64 in a direct evaluation of the dipolar field. (2) A subtraction procedure in the Fourier method that both compensates for edge effects as well as reducing the effects of ghost cells.

Using these numerical tools we have developed four different models to explore the spin dynamics of a spherical cell of hyperpolarized liquid xenon. We verify using the lab frame model that the rotating wave approximation is valid even when the dipolar fields are only a factor of 10 smaller than the applied magnetic field.

In the small tip angle regime, the numerical models agree with the linear model to better than 1 percent in the frequency of phase oscillations for $gR/M_0 \ll 1$. For $gR/M_0 \approx 1$ the numerical models show that higher order gradients become important and their predictions deviate slightly from the linear model.

In the large tip angle regime, the numerical models are in agreement with the linear model on the exponential growth of linear gradients of the magnetization in response to a linear applied field gradient as long as high order gradients of the magnetization are small. The numerical models also indicate that high order gradients of the magnetization grow exponentially in response to high order gradients of the magnetic field. Gradients that

are even with respect to z cause an eventual collapse of the signal, ultimately limiting the achievable gain, but as long as the gradients are small compared to the magnetization, the phase difference can be used to measure the longitudinal gradient. High order, z odd gradients do generate a phase difference, however if such gradients remain constant, their effects can be subtracted from the phase difference to yield a measurement of the applied gradient.

Chapter 4

Experimental results and comparison with theory

In this chapter, I present our experimental results and compare them to the predictions of our models. As in the previous chapter, I discuss the data separately for the small and large tip angle regimes, as the behavior is dramatically different. We find good agreement, qualitatively and quantitatively, between theory and experiment.

For small tip angles we find that the magnetization gradients oscillate coherently, extending the free induction decay time by up to a factor of 100 compared to the non-interacting case, even for $gR/M > 1$. The frequency of the phase oscillations is in agreement with that predicted by the linear model within the accuracy to which we can measure significant parameters. The relaxation time of the phase oscillations scales approximately inversely with the magnetization and was over 1000 seconds for some data sets at high magnetization. We attribute this trend to the competing timescales associated with spectral narrowing and convection due to temperature gradients. The overall decay of the NMR signal following a small pulse, T_2^*, is affected by the degree of sphericity of the cell and the strength of the magnetic field gradient across the cell relative to the magnetization of ^{129}Xe. When all applied magnetic field gradients have been properly minimized we realized free induction decay times in excess of 1000 seconds.

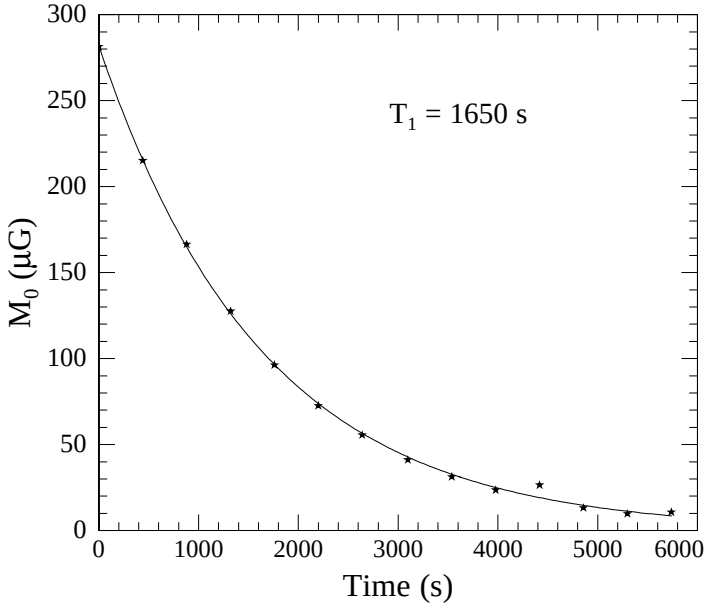

Figure 4.1: Longitudinal relaxation of hyperpolarized xenon in a low field environment.

In the large tip angle regime, we find that the phase difference between the two SQUID signals grows exponentially with a time constant predicted by the linear model. As discussed in the previous chapter, as long as all gradients of the magnetization remain small, $m_y^{(i,j)} \ll 1$, the phase difference is directly proportional to the linear longitudinal applied field gradient g, and therefore can be used to obtain a measurement of g. Since the phase difference grows exponentially in response to a small applied field gradient rather than linearly, we realize enhanced sensitivity to a small applied field gradient. Experimentally we have achieved amplification of small spin precession by a factor of up to 9.5 relative to the non-interacting case, limited by the time until collapse of the NMR signal.

4.1 Small tip angle regime

4.1.1 Longitudinal relaxation

All of the small tip angle data presented here was taken with cells that had no silicon membrane inside. We first verify that in the ultra low field environment, the longitudinal

relaxation time is still quite long. Fig 4.1 shows the longitudinal magnetization determined from the magnitude of the AC SQUID signal following a series of small angle pulses. For this data we find $T_1 = 1650$ seconds, close to the value obtained in other measurements at high magnetic field.[46, 65]

4.1.2 Transverse relaxation

The subject of the transverse relaxation time is substantially complicated by the presence of dipolar interactions. As discussed in the introduction, we verified using the method of spin echoes that the intrinsic transverse relaxation time is quite long, $T_2 \geq 1300$ s. When the magnetic field gradients are much smaller than the magnetization, spectral narrowing in the small tip angle regime reduces or eliminates the need to apply refocusing pulses. In our ultra-low field shielded environment, this condition is satisfied and for some data sets, we realized very long free induction decay times. Fig. 4.2 shows the oscillating transverse components of the magnetization following a 2° pulse, and for this data we find a free induction decay time $T_2^* = 1080$ s. The abrupt collapse of the signal was due to the deliberate application of a negative feedback from the output of the SQUIDs

We find that deviations of the cell from the spherical shape have a large effect on the transverse relaxation time T_2^* as shown in Figure 4.3. For large deviations of the cell from the spherical shape the transverse relaxation time is determined by magnetic field gradients created by the magnetization and the relaxation time increases as the magnetization decays. To illustrate this regime we plot the product $M_0 T_2^*$, which remains constant for a range of M_0 values in cells made from blown glass. On the other hand for machined glass cells we find that $M_0 T_2^*$ is approximately proportional to M_0, indicating that the transverse relaxation time is determined by gradients of the ambient magnetic field and the intrinsic transverse relaxation time of liquid ^{129}Xe.

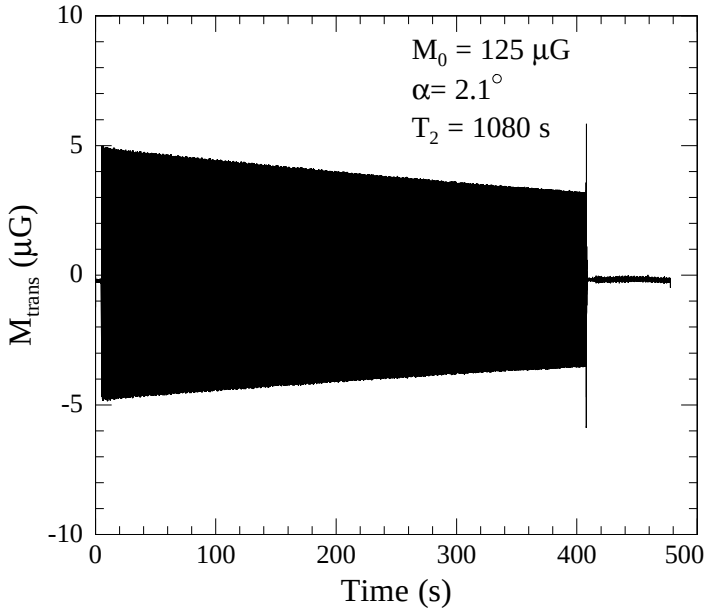

Figure 4.2: Free induction decay following a small tip angle pulse.

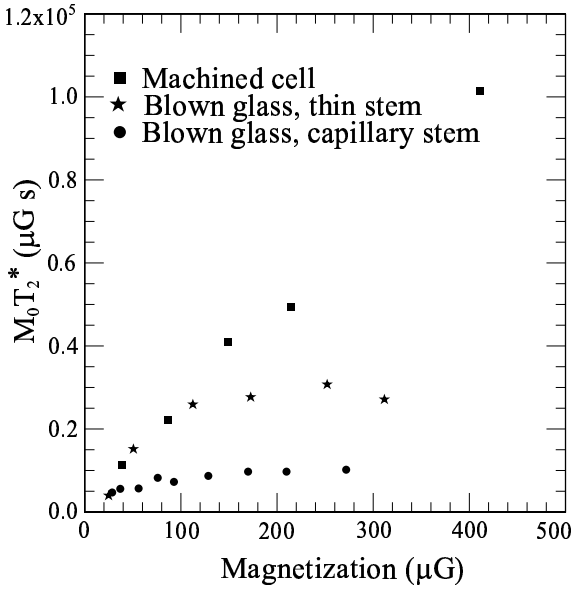

Figure 4.3: Deviations from spherical geometry have an effect on the transverse relaxation time T_2^*. The blown glass cell with a capillary stem is less spherical near the stem than the thin stem cell because the capillary has thick walls that distort the shape of the cell.

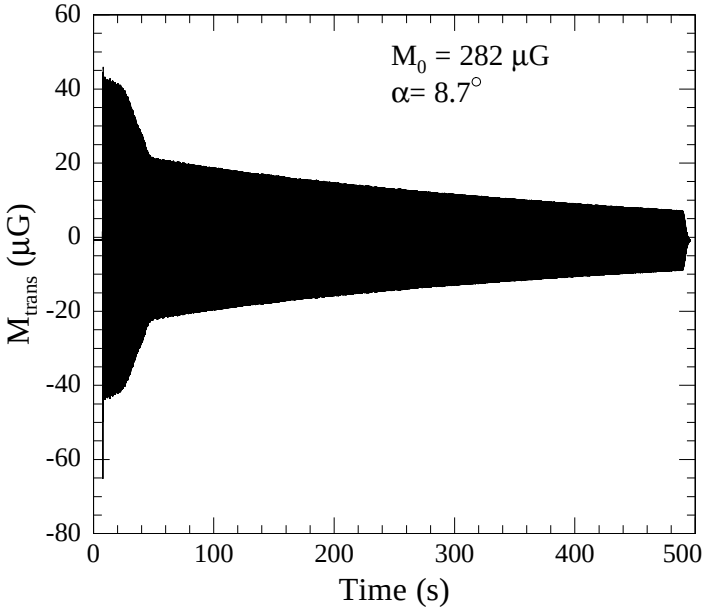

Figure 4.4: Transverse magnetization following an 8.7° tipping pulse. After a short time, the signal collapses due to some instability.

4.1.3 Dynamical instability

Though the linear model predicts that the system is stable for tip angles smaller than 35°, we find experimentally that an instability can arise for substantially smaller tip angles. To illustrate, in Fig. 4.4 we show data for a tip angle of 8.7° where the signal collapses after a short time. For smaller magnetizations, the angle at which the system became unstable tended to increase. We did not study the onset of this instability sufficiently to draw any general conclusions. Our models qualitatively reproduce this behavior for evolution in the presence of a small linear magnetic field gradient, though the instability seems to occur at tip angles closer to 15°. We suspect that the coupling of higher order gradients to each other is responsible for this behavior.

4.1.4 Frequency stability

For an electric dipole moment measurement in the small tip angle regime (this is discussed further in Chapter 5), a near uniform electric field would be applied to the entire sample.

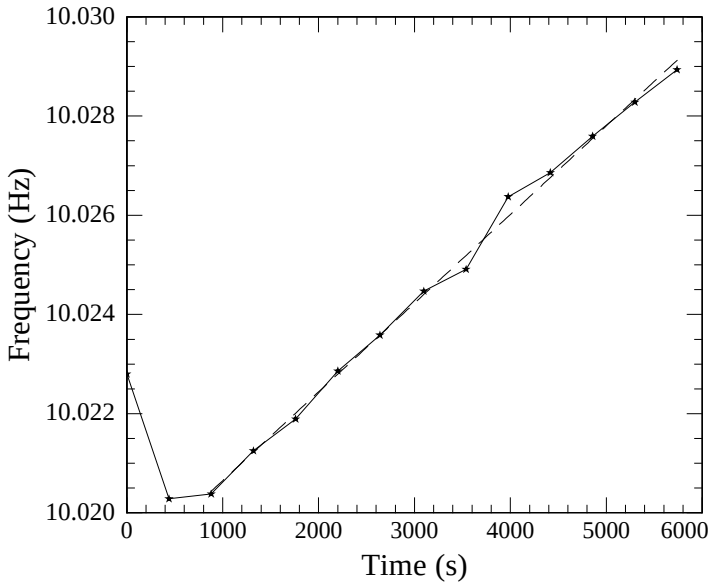

Figure 4.5: Frequency of FID following a series of small angle pulses. The dashed line is a linear fit to the data, resulting in a drift of about 1.5 nG/s

Thus, an EDM signal would be a shift in the average precession frequency, rather than a shift in the difference of the precession frequencies between either half of the cell. Since there would be no differential measurement, the frequency stability is of crucial importance. To investigate the frequency stability, we apply a series of small angle pulses and plot the precession frequency in Fig. 4.5. After the first two pulses, there appears to be a simple linear drift in the precession frequency, corresponding to a magnetic field drift of about 1.5 nG/s. The question then arises as to whether this drift is due to ambient magnetic field drifts or to dipolar magnetic fields. As discussed in Chapter 3, for a spherical cell, regardless of the magnetization profile, the average magnetic field in the cell is zero, and thus the frequency shift cannot arise from magnetization inhomogeneities. This does not rule out dipolar magnetic fields due to deformations of the cell. However as the frequency shift profile is dominated by a linear component, rather than a decaying exponential, we conclude that the largest source of frequency shifts must be due to real drifts of the magnetic field. A large source of possible drifts of the ambient magnetic field is due to changes in the temperature of the magnetic shields. Our experimental setup was not optimized for

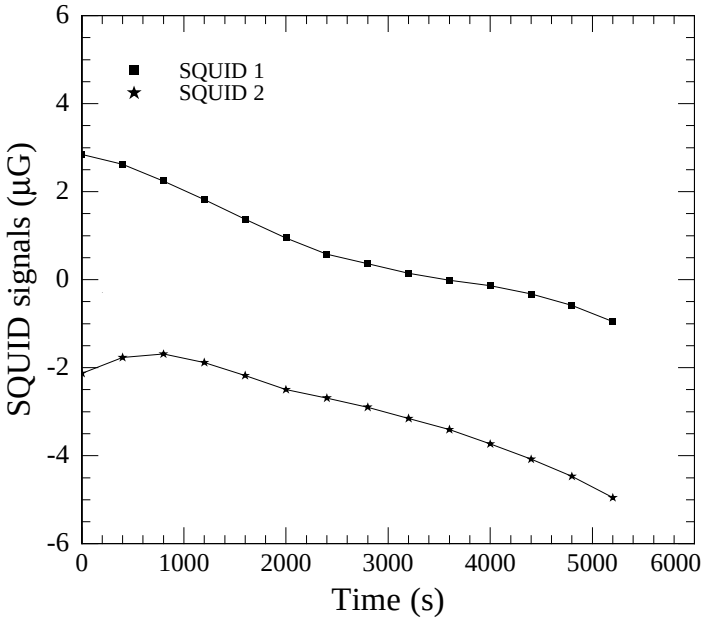

Figure 4.6: Magnetic field drift detected by SQUID magnetometers.

thermal stability (for example, the tubes that filled the dewar with liquid nitrogen were poorly insulated), and thus such an effect is highly probable.

To directly measure magnetic field drifts, we monitored the DC SQUID signal following the filling of the dewar with LN_2 when there was no xenon in the system, and plot the results in Fig. 4.6. These measurements should be taken with a grain of salt, as SQUID magnetometers have a substantial amount of $1/f$ drift. However, one would expect that drift in the two SQUID magnetometers would be uncorrelated. The drift in both SQUID signals is monotonic and has a similar slope of about 0.7 nG/s after the initial filling. If we attribute the drift to actual magnetic field drifts of the longitudinal component of the magnetic field, to compare to the magnetic field drift obtained from the xenon frequency shift, we must multiply this by a factor of $\sqrt{2}$ as the SQUID magnetometers are oriented at 45° relative to the main field. This yields a drift of B_z of about 1 nG/s, close to the drift obtained from the xenon precession frequency shift. It should be noted that this data was taken on the day following the data shown in Fig. 4.5 was taken, and is only representative of the frequency shift one might expect. These measurements indicate that good thermal

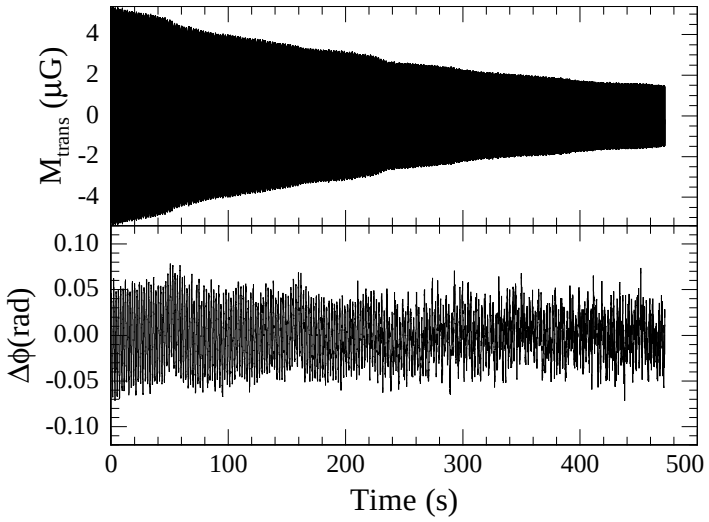

Figure 4.7: A SQUID signal (top panel) and the phase difference between two SQUIDs (bottom panel) for $M = 249\mu$G, $gR = 72\mu$G, and a tip angle of 0.0205 rad. The phase oscillations decay very slowly compared to older data at lower magnetizations shown in the introduction and discussed in Ref. [101].

insulation of the magnetic shields will be very important.

4.1.5 Phase oscillations

We determine the phase difference between the two AC SQUID signals by using the following simple algorithm. Suppose each signal is represented by

$$S_i(t) = A_i(t)\sin(\omega_0 t + \phi_i(t)). \tag{4.1}$$

We assume that changes in the amplitude and the relative phase are much slower than the Larmor precession frequency. We form two products of the signals, one with a relative phase shift of $\pi/2$ between them

$$\begin{aligned} f(t) &= S_1(t)S_2(t + \pi/2\omega_0) \\ &= A_1(t)A_2(t)/2 \times \\ &\quad [\sin\Delta\phi(t) + \sin(2\omega_0 t + \phi_1(t) + \phi_2(t))] \\ g(t) &= S_1(t)S_2(t) \end{aligned} \tag{4.2}$$

$$= \quad A_1(t)A_2(t)/2 \times$$
$$[\cos\Delta\phi(t) - \cos(2\omega_0 t + \phi_1(t) + \phi_2(t))].$$

After digitally filtering out the high frequency components of the two products and taking the ratio, one obtains the difference in phase

$$\tan\Delta\phi(t) = \frac{lowpass(f(t))}{lowpass(g(t))} \tag{4.3}$$

Figure 4.7 shows the SQUID NMR signal after a small tip angle pulse and the phase oscillations obtained in this manner. T_2^* is about 320 seconds, a factor of about 60 longer than what one would expect neglecting dipolar interactions. We fit the phase oscillations to the functional form $Ae^{-t/\tau}\sin(\omega t + \phi)$ to obtain the frequency of the phase oscillations ω and relaxation time of the phase oscillations τ. The high frequency modulations in the amplitude of the SQUID signal occur at the same frequency as the phase oscillations and are due to a slight reduction of the signal when the magnetization gradients are large.

In Figure 4.8 we plot the ratio of the phase oscillation frequency to the predictions of the linear model for both simulation and experiment without any free parameters. The frequency of phase oscillations is determined by a fit to several periods in both experiment and simulation as explained above. The scatter in the experimental data is probably due to small changes in the calibration of the magnetization due to relative motion of the SQUID and the cells caused by thermal stresses in the G10 plate to which the SQUIDs are attached. At low values of gR/M_0 the experimental data agree very well with the results of numerical calculations. The frequency is also in agreement with the results of the linear model ($\omega/\omega_{lin} = 1$). At high values of gR/M_0 we find a systematic deviation of the experimentally measured frequency from the numerical results. The results of the numerical calculations also have a systematic error of 1-2% because the phase oscillations are not perfectly sinusoidal. We also find that in this regime the frequency of the oscillations is very sensitive to other experimental parameters. For example, in our earlier study [101] with smaller values of M_0 and τ we found substantially larger increase in the frequency of the oscillations at large gR/M_0.

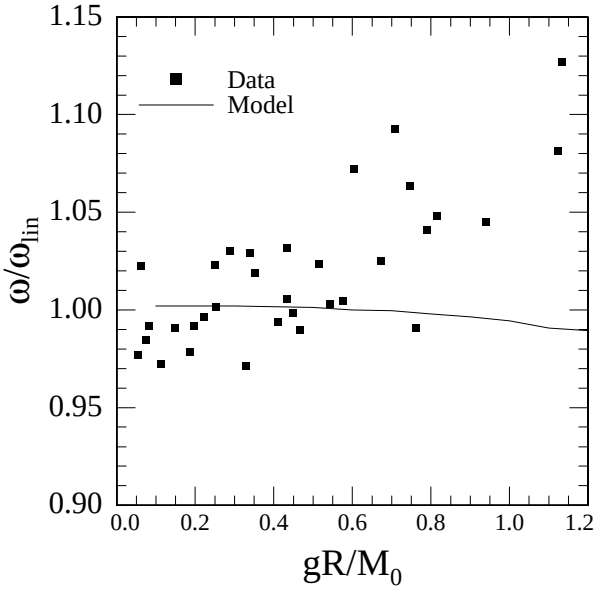

Figure 4.8: Measurements of the frequency of phase oscillations (squares) and the results of numerical simulations (solid line) plotted as a ratio to the predictions of the linear model as a function of the magnetization. Tip angles are small for all experimental data, $\alpha \leq 0.12$ rad.

Our numerical simulations also approximately reproduce the aharmonicity of the phase oscillations for large values of gR/M_0. To analyze these effects quantitatively we perform an FFT on the phase oscillation signals for both experimental data and simulation taking care that there is an integral number of periods in the sample to be transformed. The resulting spectrum is shown in Figure 4.9. The vertical scale of the simulation FFT has been adjusted to compensate for slight differences in the magnetization between the simulation and experimental data. The spectra of phase oscillations for both simulation and data exhibit a single narrow peak at $\omega = \omega_{lin}$ for small gR/M_0. For large gR/M_0, two extra peaks appear to the right of the main peak at approximately $\omega = 3\omega_{lin}/2$ and $\omega = 2\omega_{lin}$ in both simulation and experiment. These extra peaks are due to the different rates of oscillation of higher order gradients that mix in a non-trivial way.

In Figure 4.10 we show the observed relaxation time τ of the phase oscillations as a function of the magnetization. At low magnetization our data are consistent with earlier

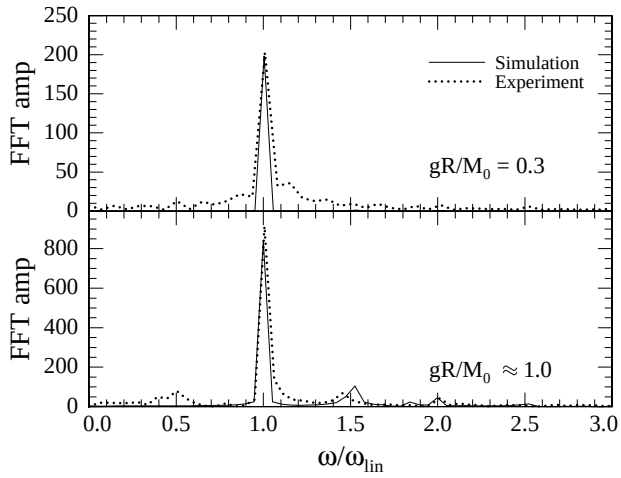

Figure 4.9: FFT of the phase oscillations for both simulation and experiment at small and large gR/M_0. Extra peaks appear to the right of the main peak at $\omega = 1.5\omega_{lin}$ and $2\omega_{lin}$ for large gR/M_0.

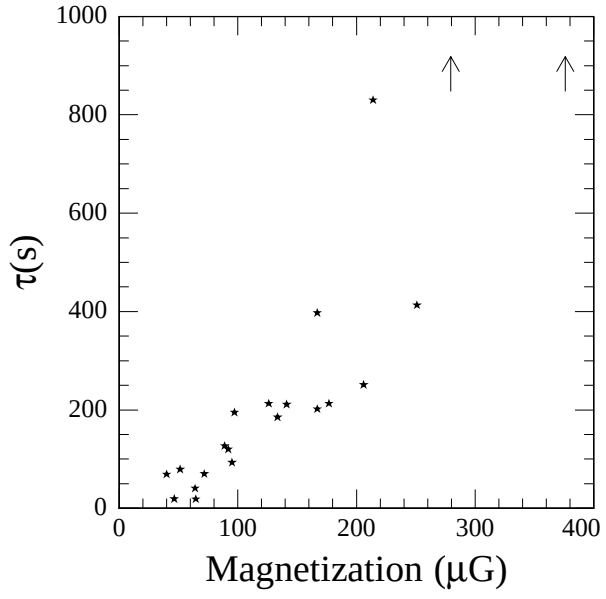

Figure 4.10: Relaxation time of phase oscillations as a function of the magnetization. Data were taken at $gR = 66\mu$G and tip angles ranging from 0.0205 to 0.123 rad. Arrows indicate data sets where the value of τ was too long to measure accurately.

results [101], but for higher magnetization ($M_0 > 100\mu$G) we observe much longer values of τ. In some data sets the decay time is even too long to be measured reliably. For large magnetization the values of τ are consistent with our estimates of relaxation due to diffusion on the order of 2000 sec. At low magnetization we believe the oscillations are more readily affected by convection effects. This behavior can be explained by the following scaling argument. When the frequency of phase oscillations is large (high magnetization) compared to the rate of convection, the magnetization will be transported through the cell adiabatically and follow the coherent behavior predicted by the dipolar interactions. At low magnetization, the frequency of phase oscillations is comparable to the rate of transport due to thermal gradients and the magnetization cannot follow the oscillations due to the dipolar fields hence smearing out the magnetization gradients. The scatter in the relaxation time data could be due to initial magnetization inhomogeneities or different convection patterns due to slight temperature gradients.

To explore the effects of temperature gradients, we deliberately applied a large temperature gradient (approximately 15 K/cm) by warming the bottom of the cell with a jet of warm nitrogen vapor flowing through a small teflon tube. We found that large temperature gradients can induce convection currents which significantly affect the evolution of the phase oscillations. To illustrate, in Fig 4.11 we show the evolution of the phase oscillations after applying a small tip angle pulse. At $\sim 50\,$sec we turned on the jet of nitrogen. Once the temperature gradients were established, the phase oscillations rapidly decayed.

4.2 Large tip angle regime

In the large tip angle regime, we first verified that the phase difference between the two SQUID signals grows exponentially with a time constant determined by the linear model. For the data shown in Fig. 1.10, the applied gradient was $g = 8.4 \pm 1\,\mu$G/cm the magnetization is $42 \pm 2\,\mu$G, yielding, via Eq. 3.15 $\beta = 0.74 \pm 0.04$ sec^{-1} for $\alpha = \pi/2$. Fitting the

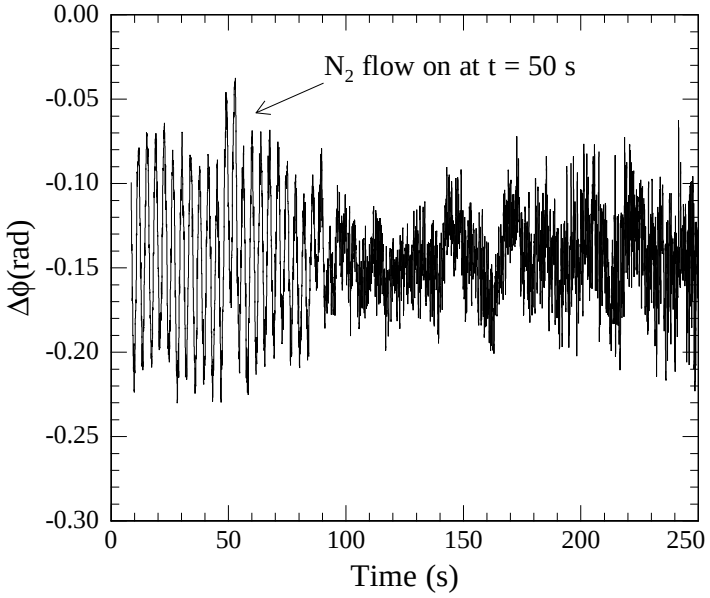

Figure 4.11: Demonstration of the effects of temperature gradients on the evolution of the phase oscillations. For this data, $M_0 = 60\,\mu$G, $\alpha = 4.7°$ and $g = 88\,\mu$G/cm.

phase difference to Eq. 3.19

$$\Delta(\phi) = \xi m_y^{(1,0)} = \xi \frac{\gamma g R}{\beta} \sinh(\beta t), \tag{4.4}$$

allowing both the gradient g and β to vary, we find $g = 8.0\,\mu$G and $\beta = 0.75$ sec^{-1}.

For the rest of the data presented here, the cell was divided by a 25 μm silicon membrane. This membrane served to inhibit convection due to small residual temperature gradients and provided the ability to mix the sample by rotating the membrane, as discussed in Chapter 2. Our algorithm for taking data was slightly different in the large tip angle regime. Following a $\pi/2$ pulse, the magnetization will rapidly collapse under the influence of its own dipolar magnetic fields. In order to make multiple measurements on a single sample of polarized xenon, data was taken with the following simple protocol: 1) A $\pi/2$ pulse was applied, tipping the magnetization into the x direction of the rotating frame. 2) The magnetization evolved under the influence of its own dipolar fields, and in real time we recorded the amplitude and the phase difference between the two SQUID signals. 3) When the NMR signal dropped to 90% of its initial value, a second $\pi/2$ pulse, 180° out

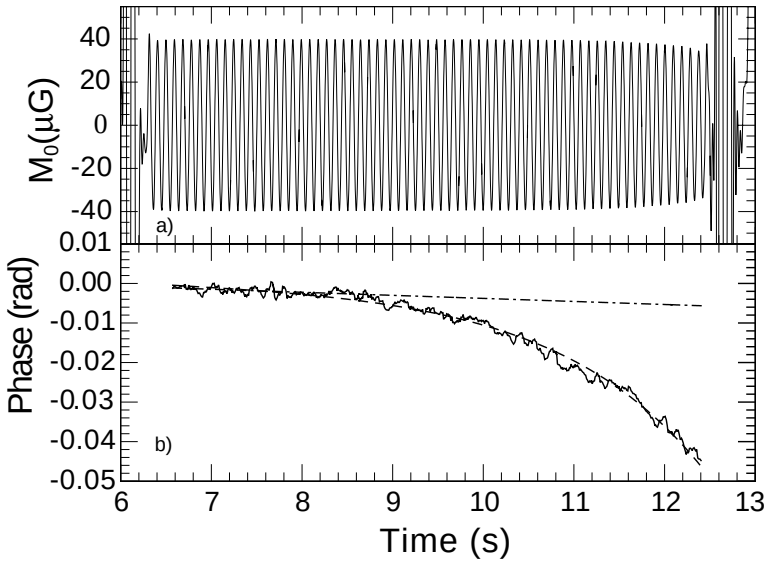

Figure 4.12: Top panel: SQUID NMR signal following a $\pi/2$ pulse. After the signal drops to 90% of its initial value a second pulse is applied to realign the magnetization with the longitudinal direction. Bottom panel: Phase difference between the SQUID signals.

of phase with the first was applied to realign the magnetization with the holding field. Small residual transverse components of the magnetization were then damped using the method described in Chapter 2. 4) We then oscillated the silicon membrane to mix the magnetization, returning the magnetization to its original homogeneous state.

In the top panel of Fig. 4.12 we plot one of the SQUID signals and the phase difference between the two SQUID signals in the bottom panel. To determine the phase in real time, we fit one period of each SQUID signal to $a_i \sin(\omega_0 t + \phi_i)$, varying only the amplitude and phase. The gradient g is determined by fitting the resulting phase difference to Eq. 4.4 where now the only free parameter is g; $\beta = \frac{8\pi}{15}\gamma M_0$ was determined from the initial amplitude of the NMR signal. The dash-dot line is a linear fit to the first half second of data, demonstrating that in the non-interacting case, the phase difference was barely above the noise level of the detection system. The gain over the non interacting system by the time the signal drops to 90% of its initial value was 9.5.

The numerical simulations discussed in the previous chapter indicate that the gain is likely limited by high order gradients of the magnetic field. According to the inset of

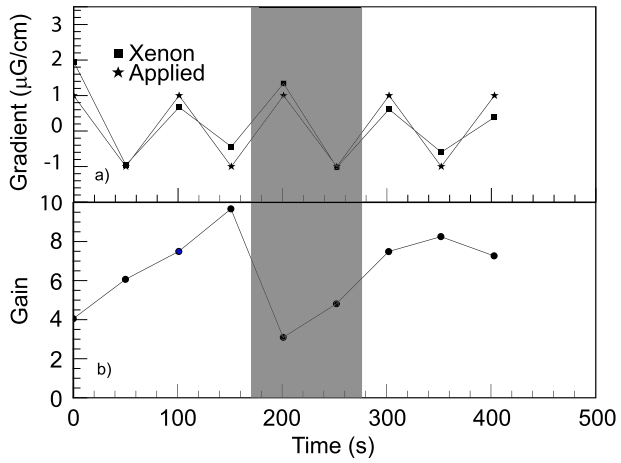

Figure 4.13: Top panel: Measurement of an oscillating gradient. Stars show the applied gradient and squares show the gradient measured using non-linear spin precession. Bottom panel: Amplification achieved using non-linear spin precession relative to the non-interacting case. The gain drops when the sample is not mixed in the shaded region

Fig. 3.8, the gain appears to scale roughly as $(g_{zz}R^2/M_0)^{-1}$. For $M_0 = 40\,\mu$G, and a second order gradient of 1 μG/cm^2, which cannot be excluded based on our mapping of the magnetic field, $g_{zz}R^2/M_0 = 0.00625$. Extrapolating the numerically calculated gain function to $g_{zz}R^2/M_0 = 0.00625$ yields a gain of 8.8, roughly consistent with our data. The presence of a large higher order gradient would explain why the phase difference for the data shown in Fig. 4.12 is still relatively small (though 10 times larger than in the non-interacting case!) by the time the signal starts to collapse. The collapse of the NMR signal is due to large high order gradients of the magnetization that do not generate a large phase difference in the SQUID signals.

By applying a series of double pulses we made repeated measurements of the magnetic field gradient. In the top panel of Fig. 4.13 we show data where the applied longitudinal gradient is oscillated with peak-to-peak amplitude of $2\,\mu$G/cm between each set of pulses. The stars represent the applied gradient and the squares represent the gradient measured by using non-linear spin precession. There is a strong correlation between the applied and measured gradient, indicating that non-linear spin precession faithfully reproduces the applied gradient.

The bottom panel of Fig. 4.13 shows the gain parameter for the same data set. We associate the rising gain at the beginning of the data set with a smearing out of initial magnetization inhomogeneities by diffusion. For the 5th and 6th points, the sample was not mixed and correspondingly, the gain parameter dropped. Resuming the mixing improved the gain parameter.

In the top panel of Fig. 4.14 we show the difference between the applied field gradient and the gradient measured using non-linear spin precession. There are several possible reasons for the differences between the measured and applied gradient in Fig. 4.13. The most obvious is that the ambient magnetic field gradient is drifting due to thermal fluctuations of the magnetic shields. Interpreting the noise in the measured gradient in this fashion, we see that fluctuations of the magnetic field gradients occur at the level of $0.5\,\mu$G/cm.

Another likely source of the deviation of the measured gradient from the applied gradient are initial gradients of the magnetization, $\delta m_y^{(1,0)}$ and $\delta m_z^{(1,0)}$. Interpreting the fluctuations of the measured gradient as due entirely to the fluctuations of the initial gradients, we can obtain an estimate of the initial homogeneity of the sample based on Eqs. 3.12 and 3.17. We plot this in the bottom panel of Fig. 4.14, and thus we can set a limit on the size of the initial gradients of the magnetization at the level of 0.5%. Since these fluctuations start out smaller and seem to grow larger as time grows on, it may simply be that gradients from the previous trial have not been completely erased through the mixing process. One possibility for obtaining a more uniformly polarized sample would be to turn the membrane sideways so that the magnetic field is parallel to the plane of the membrane to allow diffusion and convection to mix the sample. However, as discussed earlier, the relaxation of the first order gradient of the magnetization due to diffusion occurs at timescales on the order of 1000's of seconds. Utilizing diffusion to smooth out gradients would thus take so long as to negate any benefits of spin precession amplification. Active mixing will be necessary.

A third source of noise in the measurements presented in Fig. 4.13 is that due to currents in the feedback coil of the SQUID magnetometers. If the SQUID magnetometers lock to a point such that the average signal (directly proportional to the current in the

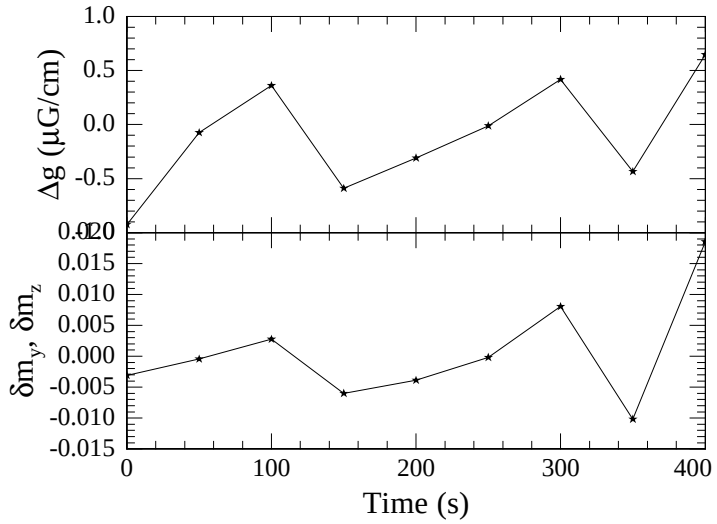

Figure 4.14: Top panel: difference between the measured magnetic field and the applied magnetic field gradient. Bottom panel: extraction of residual magnetization gradients $\delta m_y, \delta m_z$ based on Eq. 5.15 and the differences between the measured and applied gradients.

feedback coil) is nonzero, there will be a DC gradient in the longitudinal direction. In Fig. 4.15 we plot the average gradient across the cell due to the SQUIDs determined from the average SQUID signals and the calibrations in Chapter 2. The magnitude of the gradients due to the SQUIDs is consistent with the magnitude of the measured fluctuations. There also appears to be some (admittedly rough) correlation between the gradients due to the SQUIDs and the measured gradients. In light of the other sources of noise, perfect correlation cannot be expected. We briefly discuss a modification of the typical SQUID magnetometer configuration that will help to suppress the back reaction of the SQUIDs on the spins in Chapter 5.

Finally convection due to residual temperature gradients could effect the outcome of a measurement. While the presence of the membrane should largely inhibit convection across the cell, convection in either half of the cell could have an influence on the nonlinear evolution of the spins. As in the small tip angle regime, the effects of convection will become more important when the time scale of dipolar interactions becomes comparable to the time scale associated with convection at low magnetization. We do not have a clear

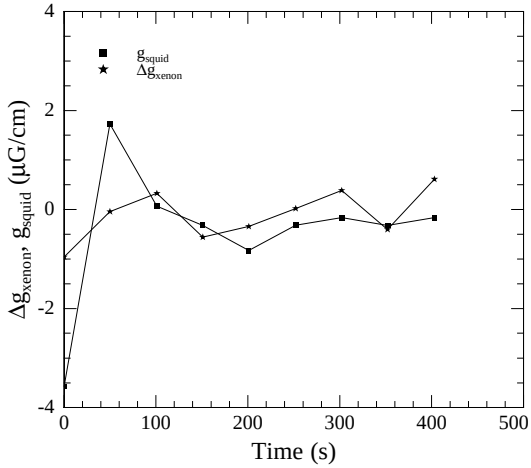

Figure 4.15: Stars represent the difference between the gradient measured with xenon and the applied gradient. There appears to be some (rough) correlation between gradients due to the DC offset of the SQUID magnetometers (squares) and the fluctuations of the measured magnetic field gradient

understanding of these effects yet, but it seems plausible that convection could lead to a smearing out of the gradients, which would reduce the measured gradient relative to the applied gradient. The amplitude of the measured gradient in Fig. 4.13 appears to be slightly reduced towards the end of the data set where the magnetization and hence the time scale associated with dipolar interactions is smaller.

4.3 Summary

In the small tip angle regime we have observed coherent oscillations of the magnetization gradients corresponding to spectral narrowing by up to a factor of 100. Using the Fourier model we have estimated the effects of diffusion and found that they are consistent with the longest values of τ obtained. We believe that convection generated by residual temperature gradients also plays an important role in the decay of the phase oscillations especially at low magnetization. We have also shown experimentally that deviations of the sample from perfectly spherical have a substantial effect on the transverse relaxation time.

In the large tip angle regime, we have shown that the phase difference between the two

SQUID signals grows exponentially, and under sufficiently well controlled conditions, the phase difference can be used to measure the first order longitudinal magnetic field gradient. This results in improved sensitivity to magnetic field gradients. Our data is in agreement with numerical models to the extent that we can determine high order gradients of the magnetic field. Experimentally we have achieved a gain over the non-interacting case by a factor of almost 10. Our setup was not optimized for magnetic field stability and we anticipate substantial improvements in the gain function with further optimization.

Chapter 5

Prospects for an EDM experiment

In this chapter, we will evaluate the feasibility of an EDM experiment in liquid xenon. We will estimate the expected statistical sensitivity from a measurement based on non-linear spin precession in the large tip angle regime and compare it to estimates in the small tip angle regime. We will also examine likely sources of systematic effects and methods for suppressing them in the two different regimes.

5.1 Statistical Sensitivity - Large Tip Angle Regime

An EDM produces a shift in the precession frequency

$$\Delta\omega = 4dE/\hbar. \tag{5.1}$$

between either half of the cell. For an EDM of 10^{-29} $e$cm in an electric field of 50 kV/cm this is $\Delta\omega = 3 \times 10^{-9}$ rad/s. The difference in precession frequency between spins separated by a distance Δz in a magnetic field gradient g is $\Delta\omega = g\Delta z\gamma$ and hence we relate the effects of spurious magnetic field gradients to electric dipole moments by

$$d = \frac{\hbar g \Delta z \gamma}{4E}. \tag{5.2}$$

Thus for a baseline $\Delta z = R = 0.5$ cm, a sensitivity to an EDM of $\delta d = 10^{-29}$ e-cm corresponds to a magnetic field gradient sensitivity of $\delta g = 8.3 \times 10^{-7}\,\mu$G/cm.

5.1.1 Single shot sensitivity

We first determine the accuracy with which we can measure the gradient from a single measurement taking advantage of non-linear spin precession. The precessing magnetization generates an oscillating signal in the SQUID magnetometers. If we transform into the rotating frame by use of a lock in detection scheme (experimentally, this can be accomplished by multiplying the signal with a reference signal of near the same frequency and filtering out the resulting high frequency component), the in phase signal is $A_x = B_M$, the average of the magnetic field produced by the sample at the SQUID pickup coil. The out of phase signal A_y is nominally zero, but can only be constrained to within the noise of the SQUID magnetometer, hence $\delta A_y = \delta B$ for unit bandwidth. The accuracy with which we can determine the phase of the precession during measurement time Δt is then

$$\sigma_\phi = \frac{\delta A_y}{A_x} = \frac{\delta B}{B_M \sqrt{\Delta t}}. \tag{5.3}$$

Here we assume that the signal does not decay substantially over the course of these measurements so that B_M and consequently σ_ϕ are constant. As derived in Section 3.2, under the influence of dipolar interactions and a small gradient g, the phase difference between the two SQUID signals takes the form

$$\Delta\phi = a \sinh(\beta t) \tag{5.4}$$

where $a = \xi\gamma g R/\beta$. A measurement of the gradient is then determined by a fit to the difference in phase of the two SQUID signals to the curve $a\sinh(\beta t)$ with a as the only free parameter; β is determined from the initial amplitude of the NMR signal. Since this fit is linear in $\sinh(\beta t)$, the precision with which we can determine a is $\sigma_a = \left(\frac{1}{2}\frac{d^2S}{da^2}\right)^{-1/2}$ where

$$S = \sum_i \left(\frac{\Delta\phi_i - a\sinh(\beta t_i)}{\sigma_{\Delta\phi}} \right)^2. \tag{5.5}$$

Here $\sigma_{\Delta\phi} = \sqrt{2}\sigma_\phi$ since the errors in the phases of the individual SQUID signals add quadratically to determine the error in the phase difference between the two signals and each measurement $\Delta\phi_i$ is taken at multiples of Δt. Doing a bit of algebra, we obtain

$$\frac{d^2S}{da^2} = \frac{1}{\sigma_\phi^2} \sum_i \sinh^2(\beta t_i) \tag{5.6}$$

$$= \frac{1}{\sigma_\phi^2}\frac{1}{\Delta t}\int_0^{t_c}\sinh^2(2\beta t)dt \tag{5.7}$$

$$= \frac{1}{\sigma_\phi^2}\frac{1}{\Delta t}\left(-\frac{t_c}{2}+\frac{\sinh(\beta t_c)}{4\beta}\right). \tag{5.8}$$

And finally, we arrive at

$$\sigma_a = \frac{\sigma_\phi 2\sqrt{2\beta}\sqrt{\Delta t}}{\sqrt{-2\beta t_c+\sinh(2\beta t_c)}}. \tag{5.9}$$

The amplitude $a = \xi\gamma g R/\beta$ so that the precision with which we can determine g is

$$\sigma_g = \frac{\delta B}{B_M \xi\gamma R}\frac{2\sqrt{2}\beta^{3/2}}{\sqrt{-2\beta t_c+\sinh(2\beta t_c)}}, \tag{5.10}$$

where we have made use of Eq. 5.3. In the limit $\beta t_c \gg 1$ this becomes

$$\sigma_g = \frac{\delta B}{B_M \xi\gamma R}\frac{4\beta^{3/2}}{e^{\beta t_c}}. \tag{5.11}$$

As a check, we take the limit $\beta \to 0$ to obtain the sensitivity in the noninteracting case yielding

$$\sigma_g^{(NI)} = \frac{\delta B}{B_M \xi\gamma R}\frac{\sqrt{6}}{t_c^{3/2}} \tag{5.12}$$

which can be obtained through other means.

For a sample with 1% polarization, the magnetization is $M_0 = 0.01 \times 0.25 \times n\mu_{xe} = 136\,\mu$G, where the factor of 0.25 takes into account the natural abundance of ^{129}Xe, $n = 1.4 \times 10^{22}/\text{cm}^3$ is the number density of liquid xenon and the nuclear magnetic moment is $\mu_{xe} = 0.77 \times \mu_N = 3.88 \times 10^{-24}$ erg/G. This corresponds to $\beta = \frac{8\pi\sqrt{2}}{15}\gamma M_0 = 2.37\ \text{s}^{-1}$. We choose this value of the polarization because we found it difficult to control the non-linear evolution of the spins for higher magnetization. It is possible that with further optimization it would be easier to control the non-linear evolution of the sample at higher magnetization. The magnetic moment of the entire sample is

$$m = \frac{4\pi}{3}R^3 M = 9.46 \times 10^{-5}\,\text{erg/G} \tag{5.13}$$

for a cell of radius $R = 0.55$ cm. The magnetic field detected by the SQUID (refer to the inset of Fig. 2.1 for a coordinate system) is the projection of the magnetic field produced by the sample onto the vector normal to the SQUID pickup coil

$$B_M = \hat{\mathbf{n}}\cdot\mathbf{B}_m = \hat{\mathbf{n}}\cdot\frac{3(\hat{\mathbf{n}}\cdot\mathbf{m})\hat{\mathbf{n}}-\mathbf{m}}{r^3}, \tag{5.14}$$

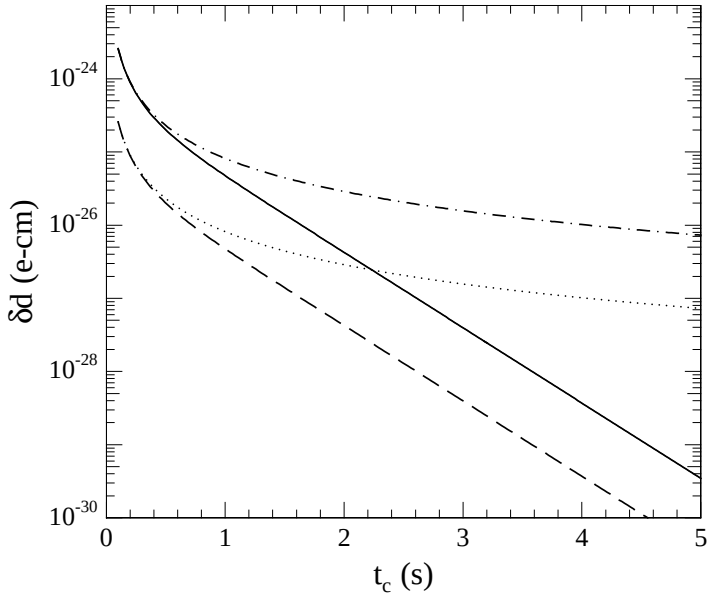

Figure 5.1: Single shot sensitivity to an EDM in a 50 kV electric field as a function of the time over which we can make a measurement (i.e. until the signal collapses due to ambient magnetic field gradients). The solid and dashed lines show the sensitivity using nonlinear spin precession given by Eqs. 5.2 and 5.10 for high and low T_c SQUIDs, respectively. For comparison, the dash-dot and dotted lines show the sensitivity for the case of linear spin precession given by Eqs. 5.2 and 5.12 for high and low T_c SQUIDs.

where r is the distance from the center of the SQUIDs to the center of the cell. For SQUIDs oriented at $\pm 45^\circ$ to the $\hat{\mathbf{z}}$ axis, this reduces to $B_M = \sqrt{2}m/r^3 = 39.6\,\mu$G for $r = 1.5$cm.

For high T_c SQUID magnetometers, the sensitivity under optimal conditions is about $\delta B = 2 \times 10^{-4}\,\mu\text{G}/\sqrt{\text{Hz}}$, and for low T_c SQUIDs it is possible to realize a sensitivity of $\delta B = 2 \times 10^{-5}\,\mu\text{G}/\sqrt{\text{Hz}}$. In Fig. 5.1 we show the sensitivity to an EDM that can be obtained in a single measurement. This plot assumes an electric field of 50 kV/cm. For the case of high T_c SQUIDs and a collapse time $t_c = 2$ s corresponding to a dimensionless gain parameter $G = \sinh(\beta t_c)/\beta t_c = 11$, we achieve a single shot sensitivity $\delta d = 4.2 \times 10^{-27}$ e-cm. To achieve sensitivity at the level of 10^{-29} e-cm requires the average of 173000 such measurements, or about 4 days assuming there is no dead time. If the ambient magnetic field gradients can be made sufficiently small so that the collapse time is extended to 3 seconds ($G = 77$), we achieve a single shot sensitivity of 3.8×10^{-28} e-cm, requiring only

about 1500 measurements or 4500 seconds to achieve the same sensitivity. For comparison, in the non-interacting case, single shot measurements of 3 seconds would require a total of 81 days to achieve sensitivity at the level of 10^{-29} e-cm. Non-linear spin precession amplification appears very attractive under ideal conditions!

In principle, the use of non-linear spin precession amplification allows sensitive measurements to be made without the use of sensitive detectors. However it is likely that a real EDM experiment will use low T_c SQUID detectors, which would allow a factor of 10 improvement in single shot sensitivity, reducing the total integration time by a factor of 100.

5.1.2 Sources of noise

The above estimates assume that the ambient magnetic field gradients are perfectly constant and fluctuations of the measured gradient in a single shot measurement are due solely to noise in the SQUID magnetometers. There are of course a number of other possible sources of noise. We summarize many of these possible sources of noise in Fig. 5.2. The solid line represents the resolution capabilities based solely on the signal to noise ratio of high T_c SQUIDs for non-linear precession. The dashed lines represent various sources of noise as discussed below.

Magnetization gradient noise

We expect the biggest source of noise to be fluctuations in the homogeneity of the sample. Equating the solution for non-zero initial gradients Eq. 3.17 with the solution for a small applied gradient Eq. 3.12, we find that noise in the initial magnetization inhomogeneities generate noise in the measured gradient at the level of

$$\delta g = \xi \frac{(\delta m_y + \sqrt{2}\delta m_z) M_0}{R} \frac{8\pi\sqrt{2}}{15}. \tag{5.15}$$

The maximum acceptable level of initial inhomogeneities is determined by asking what degree of inhomogeneity would generate noise that could be measured in a single shot based on non-linear spin precession. Assuming we can achieve a gain $G = 20$ for a measurement

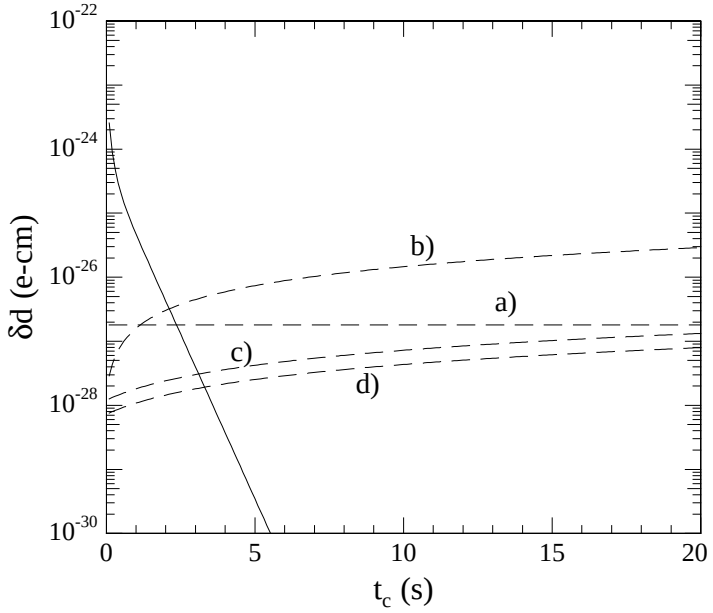

Figure 5.2: Dashed lines represent various sources of noise. a) represents the noise due to fluctuations of initial gradients of the magnetization at the level of a part in 10^6. b) represents fluctuations of the gradient due to magnetic noise generated by the SQUID magnetometers. c) represents the gradient noise due to Johnson currents and thermal drifts of the magnetic shields. d) shows the gradient noise due to coupling of the drifts in the homogenous part of the field with the SQUID magnetometers. The solid lines represent the sensitivity of a single shot measurement of the magnetic field gradient for non-linear spin precession.

time of 2.3 seconds and $M_0 = 136\,\mu$G, using high T_c SQUIDs, the single shot measurement sensitivity is 1.8×10^{-27} e-cm, corresponding to magnetization inhomogeneities at the level of 0.5×10^{-6}. This level of noise is represented by the flat line, curve a), in Fig. 5.2, requiring about 32400 measurements or $\sim$ 1 day of integration to achieve a sensitivity of $10^{-29}\,e$cm. Realizing such initial magnetization uniformity is expected to be a major challenge. Achieving homogeneity better than this will not improve the measurement if other factors, such as the time until collapse of the signal or ambient magnetic field gradient noise, are limiting the sensitivity.

Is it possible to achieve such uniformity? For the parameters that describe our experiment, dipolar magnetic fields generate very small forces in the fluid compared to the force

exerted by the mixing membrane, and hence we treat the magnetization as a *passive* property of the fluid, one that does not influence its motion. Since the mixing process does not generate rotations of the magnetization, the three components of the magnetization may be treated as independent scalar fields. The decay of gradients of a passive scalar in a turbulent flow is a long standing problem of considerable interest. For example, the pharmaceutical industry would be interested in achieving a high degree of uniformity of chemicals in mixing tanks. For a recent review of this problem see, Ref. [110]. In the case of periodic velocity flows in two dimensional systems with low Reynolds number, persistent scalar patterns have been observed in the concentration of the passive scalar, while for higher Reynolds numbers, the probability distribution function for the variance of the scalar decays exponentially.[111]

As a starting point, we estimate the time required to achieve the desired level of uniformity based on Taylor's theory of scalar transport in turbulent flow, where the effective diffusion constant at length scales of the cell radius R is

$$D_{eff} = \delta u R. \tag{5.16}$$

If we assume that the membrane is oscillated back and forth with an angular velocity $\Omega = \pm 2\pi \times 3$ Hz the variation in the velocity at $R/2$ is $\delta u = 2\Omega(R/2) = 9.42\,\mathrm{cm/s}$, yielding an effective diffusion constant $D_{eff} = 4.71\,\mathrm{cm}^2/\,\mathrm{sec}$. The Reynolds number is $\mathrm{R} = \delta u R/\nu = 2770$ where $\nu = 0.0015\,\mathrm{cm}^2/\,\mathrm{sec}$ is the dynamic viscosity of liquid xenon. Flow becomes unstable for Reynolds numbers in the range of 10 to 100 and turbulence is fully developed (with eddies at all length scales) for Reynolds numbers over 2000.[113] As discussed in Chapter 3, the decay time of the first diffusion eigenmode with $l = 1$ spherical harmonic, corresponding approximately to a first order gradient, is $\tau = (4.33D/R^2)^{-1} = 0.012$ sec, requiring very little time to smear out first order gradients to the level of 10^{-6} relative to their initial value. This is admittedly a very crude estimate, and does not have much to say about the smearing out of small scale inhomogeneities.

Numerical calculations were reported in Ref. [112] on the effectiveness of mixing in stirred tanks at moderate Reynolds numbers of ~ 100. These calculations demonstrate that the striation thickness of adjacent portions of a fluid steadily decreases with the number

of revolutions of the agitator, indicating that large scale inhomogeneities will be rapidly transferred to small spatial scales where molecular diffusion rapidly leads to uniformity. All of the above arguments indicate that it should be possible to achieve a high degree of spatial homogeneity.

Magnetic field noise from the shields

We first consider noise due to Johnson currents in the magnetic shields. Such currents produce magnetic fields and magnetic field gradients that are flat in frequency space. Based on work in Ref. [109] we estimate the fluctuations of the magnetic field $\delta H_{Johnson} = 10^{-4}\,\mu$G and $\delta g_{Johnson} = 10^{-5}\,\mu$G/cm. These estimates are in agreement with measurements performed in a similar set of magnetic shields.[62] The homogenous component of this noise will not directly effect our measurements (however, through coupling to the SQUIDs it can generate gradient noise, as discussed below). Magnetic field gradient noise due to Johnson currents will limit the sensitivity to an EDM at the level of about $\delta d = 1.2 \times 10^{-28}$ e-cm, requiring only about 100 measurements to reach 10^{-29} e-cm.

In addition to Johnson noise, magnetic shields typically have 1/f noise due to, for example, slow variations of the temperature causing small mechanical stresses. These effects will have to be measured more carefully, but for now we estimate a drift of the homogeneous component of the magnetic field of $\delta H_{shields} = 5 \times 10^{-5}\,\mu\text{G} - \text{Hz}$ and drift of the magnetic field gradient $\delta g_{shields} = 0.5 \times 10^{-5}\,\mu\text{G} - \text{Hz}$. The sum of the gradient noise generated by Johnson currents and thermal drifts of the magnetic shields is represented by the curve c) in Fig. 5.2.

Noise associated with SQUID magnetometers

The SQUID magnetometers can produce fluctuations of the magnetic field gradients in two ways. Noise in the output of the SQUIDs corresponds directly to noise in the current through the feedback coil. Tristan's high T_c SQUIDs have a sensitivity of $\delta B = 2 \times 10^{-4}\,\mu\text{G}/\sqrt{\text{Hz}}$ and a $1/f$ knee at 10 Hz. In Chapter 2 we saw that the output of the SQUIDs generates

magnetic field gradients at the level of

$$g^{(sq)} = 0.044(\mathrm{cm}^{-1})B_{sq}. \tag{5.17}$$

Hence, for the noise figures given above, the SQUID magnetometers generate noise at the level of

$$\delta g = 8.8 \times 10^{-6}\,\mu\mathrm{G}/\sqrt{\mathrm{Hz}} + 8.8 \times 10^{-5}\,\mu\mathrm{G\,Hz} \tag{5.18}$$

This source of noise, in EDM units is represented by curve b) in Fig. 5.2. It should be noted that this is not a fundamental source of noise, and could be reduced considerably by using low-T_c SQUID magnetometers with better low frequency noise characteristics.

Magnetic fields from the feedback coil due to compensation for drifts of the ambient homogenous magnetic field can also generate magnetic field gradient noise. Noise generated via this mechanism is represented by curve d) in Fig. 5.2, where we have used the above noise figures for the homogeneous field and Eq. 5.17.

5.2 Leakage and charging currents

5.2.1 Leakage currents

One of the most obvious sources of systematic effects are magnetic fields associated with a small current leaking across the insulating parts of the cell. Typical resistivities of pyrex or fused silica at room temperatures are on the order of 10^{14} to 10^{17} Ω-cm. The resistivity of insulators generally increases as the temperature decreases, so we take $\rho = 10^{17}$ Ω-cm as a conservative estimate. Typically, the effects of leakage currents are estimated by assuming the worst (and rather unlikely): a helical path of current around the cell wall, from one electrode to the other. Current flowing in a straight path from one electrode to another would produce only magnetic fields transverse to the main field, creating frequency shifts only quadratic in the leakage current and are considered no further. The thinnest part of our cells across which current could flow is $t = 1$ mm, and the radius is $R = 0.5$ cm so we estimate conservatively the cross section to be $a = 2 \times 2\pi Rt = 0.628\,\mathrm{cm}^2$. The length of

the path around which current would flow is approximately $l = 2\pi R = 3.14$ cm and hence the resistance of the helical path is estimated to be $R_h = \rho l/a = 5 \times 10^{17}\,\Omega$. For an electric field $E = 50$kV/cm, we need to apply approximately 25 kV to the electrodes. This would result in a leakage current $I_{leak} = 5 \times 10^{-14}$ Amps. The magnetic field in the center of a loop of current is

$$B_{leak} = \mu_0 I/2R = 6.3 \times 10^{-14}\,\mathrm{G}. \tag{5.19}$$

The Larmor precession frequency associated with this field is $\omega_{leak} = \gamma B_{leak} = 4.6 \times 10^{-10}$ rad/s, corresponding to an EDM $d_{leak} = \hbar\omega_{leak}/2E = 3 \times 10^{-30} e$-cm, well beyond our expected sensitivity for a first generation experiment.

This analysis may well be overly simplified. Leakage currents on the surface of the cell walls tend to be larger than in the bulk [11] and will have to be directly monitored. Leakage currents through the liquid xenon will also have to be considered. However, it is unlikely that such currents would tend to be azimuthal in nature.

5.2.2 Charging currents

The concern with charging currents is that they could generate magnetic fields large enough so that the spins would not be able to follow the local magnetic field adiabatically as the electric field is reversed. In this case, even when the transient magnetic field decayed to zero, the magnetization could be left in some non-uniform initial state. As a crude estimate of the currents required to charge the electrodes, we approximate the cell as a parallel plate capacitor of area $A = 1\,\mathrm{cm}^2$ and spacing $d = 0.5\,\mathrm{cm}$. For a potential of 25 kV between the electrodes, the charge on each electrode is approximately $Q = -VA\epsilon_0/d \approx 4 \times 10^{-9}$ Coulombs. For electric field reversal time of 1 second, the current is $I_{charge} = 8 \times 10^{-9}$ Amps in the longitudinal direction resulting in an azimuthal field of about 10^{-8} G. If we assume that it takes 0.1 seconds for the charging current to reach the above value, the derivative of the azimuthal magnetic field is on the order of $dH_1(t)/dt = 10^{-7}\,\mathrm{G/sec}$. The condition to be met in order for the spins to adiabatically follow the magnetic field is $\frac{dH_1(t)/dt}{H_0} \ll \gamma H_0$. For holding fields of 10 mG, this condition is easily met. To verify this, the Bloch equations were

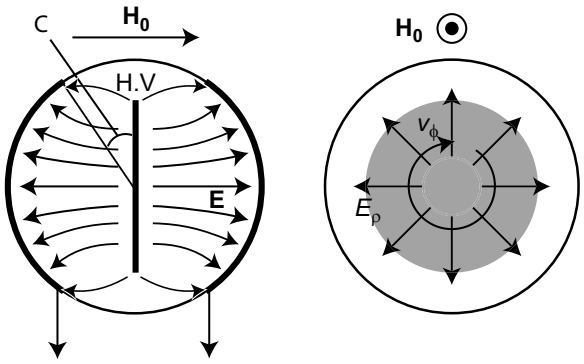

Figure 5.3: Electrodes and electric field configuration. Curved electrodes inside the cell will generate a radial component of the electric field which can lead to large $\mathbf{v} \times \mathbf{E}/c$ fields.

solved numerically for a small pulse of transverse magnetic field. The transverse excitations of the magnetization following the pulse were less than one part in 10^{12}.

5.3 Quadrupolar effects

^{129}Xe owes its long spin coherence time to the fact that the nucleus is spin 1/2 and possesses no electric quadrupole moment. An electric quadrupole moment interacts with electric field gradients and could potentially cause spurious frequency shifts. Happily, there are no such effects to contend with in this system. It should be noted that ^{131}Xe has a natural abundance of 21% and a nuclear spin $I = 3/2$ and thus can interact with electric field gradients. This should not be an issue, as the polarization of ^{131}Xe is very small on account of its fast relaxation. Furthermore, the precession frequency is a factor of 3 smaller than ^{129}Xe and hence it should not be difficult to filter any such effects out of the signal.

5.4 Motional fields

5.4.1 The v×E/c effect

If the electrodes are outside of the cell and there is a small amount of mobile charge on the inside of the cell, the charge carriers will arrange themselves in such a way as to reduce the electric field inside the cell. Therefore, EDM experiments are typically performed with

the electrodes directly inside the cell so that there is no ambiguity as to the size of the electric field inside the sample. One possible configuration is shown in Fig. 5.3. The curved electrodes generate a large radial component of the electric field, in addition to the desired longitudinal field. Consider a particle with a large azimuthal velocity component, traversing the cell on the path shown in the right side of Fig. 5.3. In the rest frame of the particle, the magnetic field is

$$\mathbf{B}' = \gamma(\mathbf{B} - \mathbf{v} \times \mathbf{E}/c) - \frac{\gamma^2}{\gamma + 1}\mathbf{v}(\mathbf{v} \cdot \mathbf{B})/c^2. \tag{5.20}$$

To lowest order in $\mathbf{v}$, the particle experiences a magnetic field

$$\mathbf{B}_{v\times E} = (\hat{\rho} v_\phi E_z - \hat{\mathbf{z}} v_\phi E_\rho)/c. \tag{5.21}$$

Two effects must be considered here, both linear in $\mathbf{E}$. The second term is responsible for the standard $\mathbf{v} \times \mathbf{E}/c$ effect. Using a 2 dimensional electrostatics program, we find for an angle $C = \pi/4$ an average radial field of approximately 1kV/cm. For a velocity of 10^{-3}cm/s and a radial field of 1 kV/cm, the z component of Eq. 5.21 field is about $10^{-7}\,\mu$G. To compare this to the signal from an EDM in units of magnetic field, we compare $4dE_z$ to $\gamma\hbar g R$. An EDM of $10^{-29}\,e$-cm corresponds to a gradient of about $8 \times 10^{-7}\mu\,$G/cm. Hence, the azimuthal component of the fluid motion must be highly suppressed to avoid such systematic effects.

The first term in Eq. 5.21 by itself cannot produce a shift in the precession frequency linear in $\mathbf{E}$. However, as was recently pointed out, [114] in conjunction with gradients of the magnetic field, the first term can lead to a shift in the precession frequency linear in $\mathbf{E}$. The analysis in Ref. [115] can be directly applied to our geometry. A small (unavoidable) gradient of the longitudinal component of the applied magnetic field gives rise to a small gradient of the radial component of the magnetic field in the radial direction: $\mathbf{B} = (B_0 + gz)\hat{\mathbf{z}} + a\rho\hat{\rho}$ where $(a = g/2)$. By transforming into the frame rotating with the trajectory of the particle, it is straightforward to show that for $v/R \ll \gamma B_0$, the combination of the radial gradient of the magnetic field and the first term in Eq. 5.21 leads to a magnetic field

$$\delta B = -\frac{a v_\phi^2 E_z}{\gamma c B_0^2} \;\text{ or }\; \delta g = -\frac{a v_\phi^2 E_z}{\gamma c R B_0^2}. \tag{5.22}$$

Note that this is suppressed by a factor of av/B_0^2 relative to the standard $\mathbf{v} \times \mathbf{E}/c$ effect. For $a = 0.1\,\mu$G/cm, $v_\phi = 10^{-3}$ cm/s, $E = 50$ kV/cm, and $B_0 = 10^4\mu$G, this evaluates to $\delta g = 1.5 \times 10^{-15}\,\mu$G/cm, far beyond the projected sensitivity of the experiment in the near term. This effect is known as the geometric effect and was a significant issue in the search for an electron EDM in thallium [6] because the velocity was about a factor 10^7 greater.

A possible method for reducing the standard $\mathbf{v} \times \mathbf{E}/c$ effect is to simply reduce the size of the radial component of the electric field by finding a different configuration for the electrodes. One possibility is that shown in Fig. 5.4. The electrodes would be three conductive parallel plates. In between the electrodes would be a dielectric material with a dielectric constant similar to that of liquid xenon. Liquid xenon would fill a spherical cavity centered between the outer electrodes. The inner electrode would have a hole cut out for the cavity. As before, there would be a circular membrane inside the cavity, in electrical contact with the middle parallel plate. As discussed above, this configuration is less desirable in that there would be some ambiguity as to the size of the electric field due to charge mobility on the inner surface of the cell. The electric field could potentially be measured via the Kerr effect, an induced birefringence due to the polarizability of the medium. The Kerr effect has been observed previously in xenon [116]. Another alternative is to choose an angle C in Fig. 5.3 such that the radial component of the field, averaged over the cell is 0.

5.4.2 Motional effect quadratic in E

We now discuss an effect due to motional fields that is quadratic in E. If the electric field reversal is not perfect this could lead to a false EDM signal. It turns out that this effect is quite small, but for the sake of pedagogy, we will derive it in some detail here. Consider a spin 1/2 particle moving in a circle where the local magnetic field traces out a cone. As the spin moves, each component of the spinor picks up an extra phase. Here we are not concerned with radial components of the applied magnetic field as they do not reverse with electric field reversals as does the radial component of the motional field 5.21. In the case

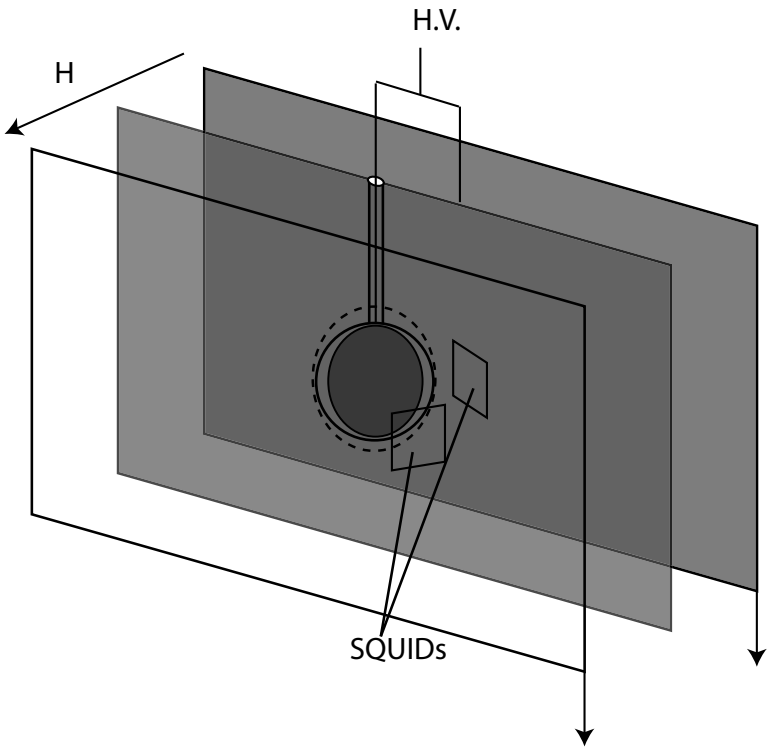

Figure 5.4: Possible configuration for electrodes to improve magnetic field homogeneity. In between electrodes would be a material with a similar dielectric constant

of motion described above, ignoring the small contribution to the longitudinal component of the field, the total magnetic field is

$$H_0\hat{\mathbf{z}} + \frac{E_z v_\phi}{c}\hat{\rho}. \tag{5.23}$$

Thus, the local magnetic field forms an angle θ with the z axis where

$$\tan\theta = \frac{E_z v_\phi}{B_0 c}. \tag{5.24}$$

Following Ref. [118], we define a set of basis vectors that are local eigenvectors of the Hamiltonian $-\mu\mathbf{s}/s \cdot \mathbf{B}(\mathbf{x})$

$$u_+ = \begin{pmatrix} \cos(\theta/2) \\ \sin(\theta/2)e^{i\phi} \end{pmatrix}, u_- = \begin{pmatrix} -\sin(\theta/2)e^{-i\phi} \\ \cos(\theta/2) \end{pmatrix} \tag{5.25}$$

where $Hu_+ = E_+u_+$ and $Hu_- = E_-u_-$. Separating the evolution of the wavefunction due

to the local hamiltonian and due to geometrical effects, we write

$$\psi = a_+(t)u_+ \exp\left\{-\frac{i}{\hbar}\int_0^t E_+(\tau)d\tau\right\} + a_-(t)u_- \exp\left\{-\frac{i}{\hbar}\int_0^t E_-(\tau)d\tau\right\}. \tag{5.26}$$

Substituting this into the Schrodinger equation $H\psi = i\hbar d\psi/dt$ we obtain

$$(\dot{a_+}u_+ + a_+\dot{u_+})e^{\frac{-i}{\hbar}\int_0^t E_+(\tau)dt} + (\dot{a_-}u_- + a_-\dot{u_-})e^{\frac{-i}{\hbar}\int_0^t E_-(\tau)dt} = 0. \tag{5.27}$$

Multiplying by $u_+\dagger$, we arrive at

$$\dot{a_+} + a_+ i\dot{\phi}\sin^2(\theta/2) = 0 \tag{5.28}$$

which has the solution

$$a_+(t) = a_+(0)e^{i\dot{\phi}\sin^2(\theta/2)t}. \tag{5.29}$$

In a similar manner, we find

$$a_-(t) = a_-(0)e^{-i\dot{\phi}\sin^2(\theta/2)t}. \tag{5.30}$$

Conveniently, the solid angle subtended by the magnetic field in a complete circuit is $\Omega = 4\pi\sin^2(\theta/2)$, so that each component acquires an extra phase $m\Omega$. Thus in a complete circuit described above, the difference in phase between each component is simply Ω, yielding a frequency shift

$$\Delta\omega = \Omega/T = 4\pi\sin^2(\theta/2)/T \approx \frac{\pi}{T}\left(\frac{Ev_\phi}{B_0 c}\right)^2 \tag{5.31}$$

where T is the time required to make a complete circuit. This is quadratic in the electric field and is only an issue if the electric field reversals are asymmetric. However, any possible shift is very small: for an electric field of 50 kV/cm, a characteristic azimuthal velocity of 10^{-3}cm/sec we find a frequency shift on the order of 2×10^{-22}Hz, far too small to cause any systematic error in the measurement of an EDM.

5.5 Sources of fluid motion

Since it appears that a major source of systematic effects are due to the motion of the fluid in the cell, we now consider how such motion could arise, and how long it will take for viscous effects to damp the fluid flow.

5.5.1 Motion due to mixing

The most obvious source of motion is the mixing process. The motion of the fluid during and following mixing is non trivial to account for because of the complicated geometry. Ideally, during the mixing process the fluid motion should be turbulent to help insure uniformity. Here we will estimate the time required for viscous effects to damp the motion of the fluid after it has slowed down into the laminar flow regime. Ignoring the presence of the membrane we can obtain some analytical results for the time required for the fluid to slow to a halt. We assume for the sake of simplification that for $t < 0$, the entire spherical cell is being rotated at constant angular velocity Ω_0 about its vertical diameter. At $t = 0$, the containing vessel is halted and we ask what the decay time of the fluid is. Assuming that the velocity profile is purely azimuthal, $\mathbf{v} = v\hat{\phi}$ and symmetric about the vertical axis, we note that $\mathbf{v} \cdot \nabla \mathbf{v} = 0$ since $\partial \mathbf{v}/\partial \phi = 0$. We also note that the assumption of azimuthal symmetry implies that the $\nabla p = 0$ and hence the Navier-Stokes equation becomes

$$\frac{\partial \mathbf{v}}{\partial t} = \nu \nabla^2 \mathbf{v}. \tag{5.32}$$

If we postulate a velocity profile $\mathbf{v} = \nabla \times f \mathbf{\Omega}_0 e^{-t/T}$ it is easy to show that Eq. 5.32 reduces to

$$\nabla^2 f \frac{1}{\nu T} f = 0. \tag{5.33}$$

The solution to this is $f = \frac{a}{r} \sin kr$, where $k = \frac{1}{\sqrt{\nu T}}$ leading to

$$\mathbf{v} = -\mathbf{\Omega}_0 \times \hat{\mathbf{r}} \left(-\frac{a}{r^2} \sin kr + \frac{ak}{r} \cos kr \right). \tag{5.34}$$

We determine k by the boundary condition for $t > 0$ $\mathbf{v}(r = R) = 0$ arriving at the condition $\tan kR - kR = 0$ The first zero of this equation occurs at $kR = 4.49$ and hence the decay time for the slowest mode is

$$T = \frac{R^2}{4.49^2 \nu}. \tag{5.35}$$

For a cell with $R = 0.5\,\mathrm{cm}$ and the kinematic viscosity of xenon $\nu = 0.0015\,\mathrm{cm^2 s}$, $T = 7.5\,\mathrm{s}$.

To determine how long we must wait between measurements, we assume that the velocity flow during the mixing process is turbulent and that it rapidly approaches laminar

flow following the mixing. The conditions for turbulent flow depend on the geometry, but generally occur if the Reynolds number R = $\Omega_0 R^2/\nu$ is greater than about 1000, so that for our model system, the flow is laminar for $\Omega_0 < 6$ rad/s. The maximum of the slowest decaying velocity profile occurs at about $r = R/2$ for which the velocity is $v = r\Omega = 1.5$ cm/s and hence we must wait about 7 e-folding times or about 50 s to reach a velocity of 10^{-3} cm/s. Having to wait this long negates any benefits we might hope to reap from using spin precession amplification, as slow drifts in the shields will become large.

Fortunately, these estimates are an absolute worst case scenario. The presence of the membrane will slow the flow down and decrease the damping time. As a *rough* estimate of the damping time of the fluid motion in the presence of the membrane, we proceed as follows. We assume that following mixing, the fluid motion is largely confined to either half of the cell and characterize the dimension of either half of the cell as that corresponding to a sphere with half the volume of the entire cell so that $R' = \frac{R}{2^{1/3}}$. For our dimensions and according to Eq. 5.35 $T = 5.2$ s and hence we must wait about 36 seconds for the velocity to reach the desired level of 10^{-3} cm/s. It should be noted that this is merely an estimate and assumes geometry similar to the original calculation. Measurements will have to be performed to obtain more realistic estimates.

5.5.2 Flow due to convection

Another possible source of fluid motion is convection due to residual temperature gradients. In general, convection will occur if there is a negative temperature gradient such that the Rayleigh number $\mathcal{R}$ is greater than some critical value $\mathcal{R}_{cr}$. For a sphere with a temperature gradient dT/dz in the vertical direction, the Rayleigh number is

$$\mathcal{R} = \frac{dT}{dz}\frac{\beta' g R^4}{\nu\chi} \tag{5.36}$$

where β' is the coefficient of thermal expansion, $\nu = \eta/\rho$ is the kinematic viscosity, λ is the thermal conductivity c_p is the heat capacity at constant pressure and $\chi = \lambda/\rho c_p$.

The critical Rayleigh number depends on the geometry. For a long right circular cylinder with a negative temperature gradient dT/dz in the vertical direction, $\mathcal{R}_{cr} = 216$.[113]

While approximating a sphere as a long right circular cylinder is not terribly accurate, it gives an order of magnitude estimate on the allowable temperature gradient. From data compiled in Ref. [119] we find for liquid xenon at approximately 170 K, $\beta' = 0.0023\,\mathrm{K}^{-1}$, $\nu = 0.0015\,\mathrm{cm}^2/\mathrm{s}$, $\lambda = 7000\,\mathrm{erg}/(\mathrm{cm\,s\,K})$, $\rho = 2.907\,\mathrm{g}/\mathrm{cm}^3$, and $c_p = 3.5 \times 10^6\,\mathrm{erg}/(\mathrm{gK})$. For these parameters, $\beta' g h^3/\nu\chi = 2.2 \times 10^6\,\mathrm{K}^{-1}$. For these numbers $\frac{\beta' g R^4}{\nu\chi} = 140000$ and hence, the biggest negative temperature gradient allowable is $dT/dz_{max} = 0.0015$ K/cm. In principle this is not really a problem as we can always insure that the cell is warmer on the top than the bottom.

Since there is no buoyancy in the horizontal direction ($\hat{\mathbf{x}}$ for concreteness), a constant temperature gradient in the transverse direction will lead to an equilibrium density configuration $\rho(x)/\rho_0 = 1 + \beta' dT/dx$. At present, the applied magnetic field is in the horizontal direction and hence fluctuating temperature gradients in the horizontal direction will generate fluctuating magnetization gradients also in the horizontal direction. Thus to achieve a density profile uniform to one part in 10^6 will require temperature uniformity in the transverse direction at the level of 4.3×10^{-4} K. For such temperature uniformity it would be well advised to use a material with as high a conductivity as possible, such as sapphire, also convenient for its excellent electrical properties.

5.5.3 Membrane Flexing

The requirement that the membrane be able to rotate necessitates that it be held somewhat loosely and from only one point, or at most two diametrically opposed points. A concern is that the membrane may flex under application of the strong electric field, causing fluid motion or asymmetries of the electric field. To understand these effects, we first calculate the forces on the membrane for a potential difference of 25 kV between the outer electrodes and the silicon membrane using a 2D numerical electrostatic analysis program (Maxwell by Ansoft). In these calculations, the cell is 10 mm in diameter and the HV membrane is 8 mm in diameter. The angle defining the edges of the ground planes is 50° relative to the symmetry axis (see Fig. 5.3 for geometry). These calculations indicate that the electrostatic

force is approximately linear over a region several mm in width about the symmetry plane, with an effective spring constant $k_E = 0.017$ N/mm.

We now estimate the degree to which the electrostatic forces will deform the high voltage electrode. For simplicity, we consider a rod of thickness a, width b, and length l, supported by one end. The restoring force due to a deflection x of the unsupported end is

$$F = \frac{xMa^3b}{4l^3} = -k_1(x - x_0) \tag{5.37}$$

where M is Young's modulus and x_0 is the equilibrium point when there is no electric field. For silicon, $M = 1.3 \times 10^{11}$ Pa. This is somewhat of a simplification, as our membrane has a circular profile with radius $R = 0.5$ cm and is thinner near the support point, however it will allow us to make an order of magnitude estimate. It is easy to show that for $k < k_E$, the symmetry plane is a point of unstable equilibrium and the membrane will find equilibrium only by smashing into the nearest ground electrode or until the spring constant of the material becomes nonlinear. For $k > k_E$ the membrane will find a new equilibrium at $x = -x_0k/(k_E - k)$, moving a distance $\Delta x = x - x_0 = -x_0(1 + k/(k_E - k)$ from its equilibrium point when the electric field is 0. We take $l = 2R$, $b = R$ and $a = 25\,\mu$m to find the restoring spring constant $k_1 = Ma^3b/4l^3 = 0.0051$ N/mm, insufficient to balance the electrostatic force.

The spring constant for a similar bar supported by two ends is $k_2 = 4Ma^3b/l^3 = 0.081$ N/mm, sufficient to balance the electrostatic forces, so that $1 + k/(k_E - k) = 0.27$mm/mm. For an initial offset of 0.1 mm, the membrane will move an additional 0.027 mm. So, if the potential across the electrodes is swept at a rate of 10 kV/s, from -25 kV to +25 kV there will result motion of the fluid with a characteristic velocity of about 0.01 mm/s, large enough to cause substantial $v \times E/c$ fields. However, assuming near perfect symmetry, motion due to flexing of the membrane will be in the form of a radial flow pattern, rather than azimuthal, and in principle should not cause substantial systematic effects. Furthermore, the electric field reversals will presumably take place following the mixing procedure, so that the motion considered here will be given time to decay along with the motion induced by mixing.

5.5.4 Non-linear dielectric effect

We consider a final source of fluid motion, the non-linear dielectric effect, which is essentially a change in the density of the dielectric with the application of an electric field. A change in the density would cause residual amounts of xenon in the stem to get sucked into the cell, causing motion of the sample in the strong electric field. In the event that the electric field strength is asymmetric, this effect could also generate magnetization gradients. There is some disagreement in the literature about the magnitude of the non-linear dielectric effect[120, 121]. The discrepancy is likely due to deformation of the parallel plates used to form the capacitors. Here we interpret these values as an upper limit on the change of the dielectric constant $dK/dE^2 < 2 \times 10^{-19}$. To find the change in density we employ the Clausius-Mossotti relationship which relates the atomic polarizability α to the dielectric constant K

$$\alpha = \frac{3\epsilon_0}{\rho}\frac{K-1}{K+2} \tag{5.38}$$

The atomic polarizability can be found in the CRC and is $\alpha = 4.4 \times 10^{-40}\,\mathrm{C-m^2/V}$ and the dielectric constant of xenon is about 1.5 [121]. The variation of the density with respect to the electric field is then

$$\frac{d\rho}{dE^2} = \frac{d\rho}{dK}\frac{dK}{dE^2} = \frac{3\epsilon_0}{\alpha}\frac{3}{(K+2)^2}\frac{dK}{dE^2} = 2.9 \times 10^9 \mathrm{m^{-3}m^2/V^2}. \tag{5.39}$$

For an applied electric field $E = 50\mathrm{kV/cm}$ we find that the density changes by $\Delta\rho = 7.2 \times 10^{16}\ \mathrm{cm^{-3}}$ or $\Delta\rho/\rho = 5 \times 10^{-6}$. Let us assume that the cell is 1 cm in diameter, with a volume $V = 0.52\ \mathrm{cm^3}$, and that the stem, 1 mm in a diameter with cross section $A = 0.0314$ $\mathrm{cm^2}$ is filled with liquid xenon. As the electric field is applied, a total of $\Delta N = V\Delta\rho$ atoms flow into the cell. The flux of atoms through the stem is then

$$F = \frac{\Delta N}{A\Delta t} = v\rho \tag{5.40}$$

where Δt is the time required to sweep the electric field and v is the fluid velocity. We find that for a sweep time of $\Delta t = 1$ s, the fluid velocity through the stem is $v \approx 8 \times 10^{-5}$ cm/s, too small to cause any serious systematic effects.

It should be noted that density changes associated with the electric field could lead to systematic effects by directly generating magnetization gradients if the electric field is asymmetric between either half of the cell. For a large asymmetry of 10% out of 50 kV/cm, the change in density is

$$\Delta\rho = \frac{d\rho}{dE^2} 2E\Delta E = 1.45 \times 10^{16}\,\mathrm{cm}^{-3} \tag{5.41}$$

or about 1 part in 10^6. Before the $\pi/2$ pulse, this would be a gradient of M_z in the $\hat{\mathbf{z}}$ direction, however the $\pi/2$ pulse, transforms this into a gradient of M_x in the $\hat{\mathbf{z}}$ direction, which does not in first order affect our measurement of g. Coupling to an applied gradient however could generate gradients of M_y at the level of $g\Delta\rho/\rho$, introducing a false EDM signal. Hence if $g\Delta\rho/\rho < 8.3 \times 10^{-7}\,\mu$G/cm, this effect should not be a serious source of systematic errors at the level of 10^{-29} e-cm. Operating in feedback mode, the longitudinal gradient g will be much smaller than 0.83μG, and hence this effect should not be an issue.

5.5.5 Measuring the velocity?

It would be helpful to have a method of measuring the velocity of the fluid without disturbing its flow to confirm that it is below the desired level of about 10^{-3} cm/s. One possible method employs the Fizeau effect [122] where the propagation velocity of light changes in a moving medium. It can be shown that the wave number is

$$k = \frac{\omega n}{c} + \frac{v\omega}{c^2}\left(1 - n\frac{d(n\omega)}{d\omega}\right) \tag{5.42}$$

for propagation in the direction of the motion of the fluid. Shifts in the phase of the light are given by $\Delta\phi = kL$ where L is the length of the path. The index of refraction is about 1.4 [124] and varies slowly over the the visible spectrum and hence the last term in parenthesis is about 2. Thus we find that the minimum resolvable velocity using this method is $\delta v = \frac{\delta\phi c^2}{L\omega}$. For an interferometer sensitivity of 10^{-3} rad/$\sqrt{\mathrm{Hz}}$ we can thus detect velocities on the order of about 3 m/s, unfortunately not sensitive enough for our requirements.

An alternative is to construct a mock EDM cell with μm size polystyrene spheres suspended in a fluid. One can then measure the velocity of the beads by detecting the Rayleigh

scattered radiation from the beads, as demonstrated in Ref. [123]. This of course has the disadvantage that it cannot be used to measure the velocity in the actual EDM cell, however, it will allow the determination of a characteristic decay time for the motion following the mixing procedure. It can be shown that the frequency shift of the Rayleigh scattered light is

$$\Delta\nu = -2\nu_0 \sin^2(\theta/2)\frac{nv}{c} \tag{5.43}$$

where the direction of motion of the particle and the propagation of the light are assumed to be parallel and θ is the angle that the scattered radiation forms with the incident light. For incident He-Ne radiation $\nu_0 \approx 2 \times 10^{15}$ Hz, and for $\theta = 30°$, the frequency shift of the scattered radiation is about 12 Hz for a particle velocity of 10^{-3} cm/s. This shift could be measured by mixing the scattered and incident radiation together and detecting the beat frequency with a photodiode. It may also be possible to simply use the atoms of the fluid as scattering centers, allowing a direct measurement of the velocity in the real EDM cell.

5.6 Alternative: Small tip angle regime?

Here we examine the possibility of performing an EDM search in the regime of small tip angles. A brief sketch of the geometry involved in this variation of the experiment is shown in Fig. 5.5. Electrically isolated conducting films in opposite hemispheres create a roughly uniform electric field. A low T_c SQUID magnetometer whose normal is oriented at 90° relative to the magnetic field detects the oscillating field created by the precessing magnetization. Spectral narrowing prevents the growth gradients of the magnetization due to the interaction of an EDM with an electric field gradient, in contrast with the large tip angle regime. Hence a search for an EDM in the low tip angle regime would rely on detecting a shift in the average precession frequency, rather than a reversal of the difference of the precession frequency associated with electric field reversals. This represents a major drawback because noise of the homogeneous component of the electric field introduces noise into the EDM signal, rather than noise of the gradient of the magnetic field which is typically suppressed by about a factor of 10 in conventional magnetic shields. To distinguish between

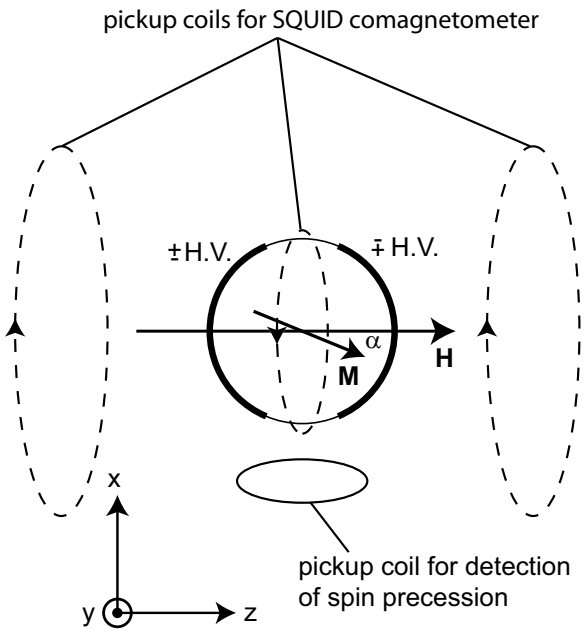

Figure 5.5: Sketch of the geometry for an EDM experiment performed in the small tip angle regime.

magnetic field noise and an frequency shifts due to an EDM, we would employ a second SQUID that would act as a comagnetometer, sensitive to H_z. The pickup coils for the second SQUID are shown as dashed lines in Fig. 5.5 where the three coils are connected in series and the inner coil has the opposite sense relative to the outer coils. This configuration would be useful to reduce the signal in the comagnetometer due to the decaying xenon polarization, but retain sensitivity to drifts in the applied field H_z. Another drawback is that spin precession due to the interaction of an EDM with an electric field would grow linearly in time rather than exponentially, necessitating the use of low-noise low T_c SQUID magnetometers.

There are, however, several features that make this scheme attractive. A major source of noise in the large tip angle regime, initial magnetization gradients, are no longer an issue in the small tip angle regime, because as noted in Chapter 3, for a spherical cell, the average dipolar field inside the cell is always zero, regardless of the magnetization configuration. This eliminates the requirement that the sample be mixed in between electric field reversals. A major systematic effect is expected to be due to $\mathbf{v} \times \mathbf{E}/c$ fields. Removing

the requirement that the sample be mixed in between measurements removes the biggest source of fluid motion, reducing this systematic effect. Furthermore, there would be less dead time associated with letting the fluid come to rest inside the cell. Less dead time in between measurements reduces the $1/f$ noise associated with the magnetic shields. The construction of the cell would also be simplified, because there would be no need to have a thin membrane inside the cell. Finally, as noted above, the small tip angle regime necessitates the use of low T_c SQUIDs, but the presence of liquid helium facilitates the use of superconducting shielding which would reduce magnetic field fluctuations considerably.

5.6.1 Initial sensitivity estimate

We have found that an instability arises for tip angles substantially less than the 35° predicted by the linear model. We did not study this in depth but suspect that it is due to the coupling of higher order gradients with each other. We have generally found that the magnetization is stable for tip angles less than about 8°. There is probably considerable opportunity to increase this figure, by optimization of higher order gradients and initial magnetization inhomogeneities, but for these initial estimates, we will assume a tip angle of 8°. The amplitude of the oscillating magnetic field produced by the sample at the center of the SQUID located a distance r from the center of the cell of radius R is

$$B_M = \frac{2\mathbf{m}_\perp}{r^3} = \frac{8\pi R^3 M_0 \sin\alpha}{3r^3} \tag{5.44}$$

For the sake of concreteness we assume a magnetization $M_0 = 300\,\mu$G, easily experimentally realizable, $R = 0.5$ cm, $r = 1.5$ cm, yielding $B_M = 13\,\mu$G. Here we assume low T_c SQUID magnetometers with a sensitivity of $\delta B = 2 \times 10^{-5}\,\mu\mathrm{G}/\sqrt{\mathrm{Hz}}$. For times short compared to the transverse relaxation time, we can measure the angular precession frequency with an accuracy

$$\delta\omega = \frac{\delta B}{B_M t^{3/2}} = 1.5 \times 10^{-6}\mathrm{Hz}^{-1/2} t^{-3/2} \tag{5.45}$$

assuming that the measurement process does not have a strong back reaction on the spins (we will address this shortly). We plot this sensitivity (solid line) as a function of mea-

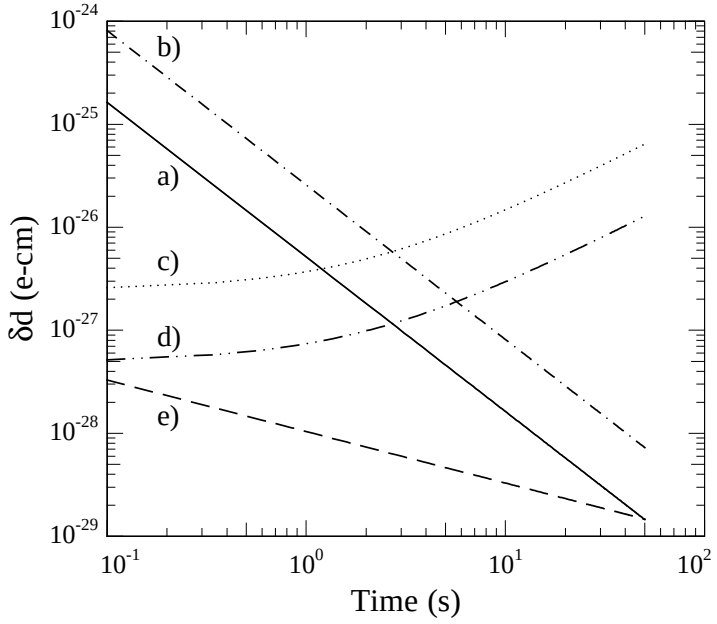

Figure 5.6: Estimates of sensitivity and sources of noise for an EDM experiment using spectral narrowing rather than non-linear spin precession amplification. Line a) represents the ability to measure frequency shifts based on the signal to noise ratio and improves as $t^{-3/2}$ for measurement times short compared to T_2^*. Line b) takes into account the extra noise in the SQUID magnetometers associated with the magnetic shields. Curve c) represents the noise in the precession frequency due to Johnson currents and 1/f noise associated with the magnetic shields. Curve d) represents our ability to subtract off magnetic field drifts with the use of a second low T_c SQUID magnetometer. Curve e) represents the back reaction of the SQUIDs on the precession of the spins, as discussed in the the section titled "Out of phase noise". For large enough times, this back reaction limits the sensitivity to scale as $t^{-1/2}$.

surement time for a single measurement on a log-log scale as a function of time in Fig. 5.6.

The preceding analysis does not take into account magnetic field noise associated with the shields in the direction normal to the SQUID pickup coil; at 10 Hz we estimate this to be primarily Johnson noise with an amplitude of about $10^{-4}\,\mu$G. Taking into account this noise we realize a sensitivity represented by the dash-dot line in Fig 5.6.

Using a single low T_c SQUID magnetometer in the small tip angle regime, a single shot measurement should achieve a sensitivity given by the intersection of curves b) and c) in Fig. 5.6, 7×10^{-27} e-cm for 3 seconds of integration. To reach the level of $10^{-29}\,e$-cm requires

about 490000 measurements, or about 17 days of total integration time. Introducing a second SQUID magnetometer, we can subtract off small variations in the magnetic field. A single shot measurement could then achieve a sensitivity given by the intersection of curves b) and d) in Fig. 5.6, 2×10^{-27} e-cm in about 6 seconds of measurement, requiring about 3 days of integration to reach the desired sensitivity of $10^{-29}\,e$-cm.

5.6.2 Back reaction of SQUIDs on spins

As discussed above, the feedback loop used to keep the flux through the SQUID constant creates its own magnetic fields. This can have two different effects on the spin precession: 1) in phase magnetic fields proportional to M_z cause a slow rotation of M_z into the $\hat{\mathbf{y}}$ direction of the rotating frame resulting in a frequency shift and 2) out of phase magnetic field noise from the SQUID can create noise in the precession angle ϕ.

Frequency shifts associated with coupling to SQUIDs

The magnetic moment of the SQUID feedback coil is proportional to the average magnetic field over the pickup coil $m_{sq} = -\eta B_M$, where we found in Chapter 2 that for our SQUIDs $\eta = 0.06\,\mathrm{erg/G/G} = 0.06\,\mathrm{cm}^3$. The average magnetic field over the pickup coil due to the sample is $B_M = 2\frac{4\pi R^3 M_0}{3r^3}\sin\alpha\cos\omega t$ and the average magnetic field across the cell due to the dipole moment of the feedback coil is $\langle \mathbf{B}_{sq}^{lab} \rangle = -\frac{2\mathbf{m}_{sq}}{r^3}$. Thus the average magnetic field in the cell created by the SQUID feedback loop is

$$\langle \mathbf{B}_{sq}^{lab} \rangle = \frac{2\mathbf{m}_{sq}}{r^3} = -\frac{2\eta B_M}{r^3} = -\eta\frac{16\pi R^3}{3r^6} M_0 \sin\alpha\cos(\omega t)\hat{\mathbf{x}} \tag{5.46}$$

In the rotating frame the magnetic field is simply half this value

$$\langle \mathbf{B}_{sq}^{rot} \rangle = -\eta\frac{8\pi R^3}{3r^6} M_0 \sin\alpha\hat{\mathbf{x}}. \tag{5.47}$$

This magnetic field rotates the $\hat{\mathbf{z}}$ component of the magnetization into the $\hat{\mathbf{y}}$ direction of the rotating frame, essentially creating a small frequency shift. The rate of change of M_y is given by one of Bloch's equations

$$\frac{dM_y}{dt} = \gamma M_z B_x = \gamma\eta M_0^2 \cos\alpha\sin\alpha\frac{8\pi R^3}{3r^6}. \tag{5.48}$$

This corresponds to a shift in the precession frequency

$$\Delta\omega = \frac{1}{M_x}\frac{dM_y}{dt} = \gamma\eta M_0 \cos\alpha \frac{8\pi R^3}{3r^6}. \tag{5.49}$$

For $M_0 = 300\,\mu$ G and $\alpha = 8°$, $\Delta\omega = 0.0126$ s^{-1}. In principle this should not be a problem in the measurement of an EDM because it scales linearly with the magnetization rather than linearly with the electric field. However, in conjunction with effects quadratic in the electric field this can give rise to a substantial systematic effect. We will discuss this shortly.

Out of phase noise

We now address the noise in the spin precession angle due to out of phase noise from the SQUID magnetometers. Noise in the SQUID magnetometers corresponds to noise in the current of the feedback loop and thus noise of the magnetic moment of the feedback loop $\delta m_{sq} = \eta\delta B$. The average magnetic field across the cell in the $\hat{\mathbf{x}}$ direction of the rotating frame is $\langle \delta B_{sq}^{rot} \rangle = \eta\delta B/r^3$. This generates noise in the y component of the magnetization by rotating M_z into the $\hat{\mathbf{y}}$ direction

$$\delta M_y = \gamma\eta\delta B/r^3 M_0 \cos\alpha \tag{5.50}$$

The noise in the phase is then

$$\delta\phi = \delta M_y/M_x = \frac{\gamma\eta\delta B}{r^3 \tan\alpha}\sqrt{t}. \tag{5.51}$$

This results in noise in the precession frequency

$$\delta\omega = \delta\phi/t = \frac{\gamma\eta\delta B}{r^3\sqrt{t}\tan\alpha}. \tag{5.52}$$

For low T_c SQUID magnetometers with sensitivity $\delta B = 2\times10^{-5}\,\mu\text{G}/\sqrt{\text{Hz}}$ we find $\delta\omega = 3.1\times10^{-8}\,t^{-1/2}$. This level of noise is represented by the curve e) in Fig 5.6. For relatively short measurement times this is not a limiting source of noise. It should be noted that these noise figures assume the geometry used in our current SQUIDs. In Section 5.7 we discuss a method for reducing this source of noise with a novel new SQUID magnetometer configuration.

5.6.3 Systematic effects

Motional effects

The standard $\mathbf{v} \times \mathbf{E}/c$ is still expected to be a major systematic effect. As mentioned above, the most obvious source of fluid motion, mixing, is eliminated, so this effect is expected to be greatly reduced.

Frequency shifts due to dipolar fields

Frequency shifts due to dipolar fields can only arise from deformations of the cell and not magnetization inhomogeneities. For an azimuthally symmetric quadrupolar deformation characterized by $R = R(1 + \epsilon S_{20}(\theta, \phi))$ (the functions S_{lm} are linear combinations of spherical harmonics discussed in Chapter 3), the resulting frequency shift is

$$\delta\omega = \frac{6\gamma\epsilon\pi M_z}{\sqrt{5}} \tag{5.53}$$

For $\epsilon = 10^{-3}$ and $M_z = 300\,\mu$G this is 5.9×10^{-3} rad/sec. In conjunction with the longitudinal relaxation of the magnetization, this will cause an exponentially decaying frequency shift. In principle, this is not a problem as this drift could be well characterized and subtracted.

Along with density changes due to the non-linear dielectric effect, frequency shifts due to deformations of the cell are a source of systematic effects. As discussed above, for electric field reversals that have an asymmetry of 10% at 50 kV, the upper limit on density shifts is about a part in 10^6, yielding a frequency shift upon reversal of the electric field at the level of 5.9×10^{-9} rad/sec, slightly larger than the frequency shift expected for an EDM at the level of $10^{-29} e$ cm. It should be noted that this assumes the upper limit for the density shifts due to the non-linear dielectric effect. At any rate, it should be possible to insure that electric field reversals are symmetric to better than 10%.

SQUID back reaction and the nonlinear dielectric effect

One systematic effect not present in the large tip angle regime is due to the back reaction of the SQUIDs on the sample in conjunction with shifts in the density of the sample quadratic in the electric field. The magnetization scales linearly with the density and the frequency shift given by Eq. 5.49 scales linearly with the magnetization and thus small asymmetries in the electric field reversal could lead to asymmetries in the magnetization. Additionally, the relaxation depends on the density, potentially leading to small frequency shifts. We take both of these into account by writing $M = M_0(1 + \delta\rho/\rho)e^{-\frac{t}{T_1}(1+\delta\rho/\rho)}$. Inserting this in Eq. 5.49 and expanding, keeping only terms linear in $\delta\rho/\rho$ we find

$$\Delta\omega = \gamma\eta M_0 \cos\alpha \frac{8\pi R^3}{3r^6}[1 - t/T_1 + \frac{\delta\rho}{\rho}(1 - 2t/T_1)]. \tag{5.54}$$

We ignore the first two terms, as they correspond to the magnetization and its monotonic, exponential decay. Furthermore, we assume that the measurement time is short compared to T_1 so that the second term in parenthesis is small compared to the first. Using Eq. 5.41, an electric field of 50 kV and an asymmetry upon reversal of the electric field of 1% we realize a frequency shift of $\delta\omega = 0.0126\,\mathrm{rad/s} \times 10^{-7} = 2.1 \times 10^{-9}$. This corresponds to an EDM of just under 10^{-29} e-cm and hence the electric field reversals must be symmetric to 1% in this scheme. These frequency shifts could be eliminated by moving the feedback coil far from the sample, as discussed in the next section.

5.6.4 Small tip angle summary

We estimate that it should be possible to achieve a sensitivity of $10^{-29}\,e$-cm in about 3 days of integration in the small tip angle regime, about a factor of $\sqrt{3}$ less sensitive than our estimates for the large tip angle regime. However, the experimental challenges are substantially different and may prove easier to overcome. One advantage is the elimination of the strict requirement that the sample be mixed in between each electric field reversal, reducing systematic effects due to motion of the fluid, namely the $\mathbf{v} \times \mathbf{E}/c$ effect. Furthermore, as discussed in Chapter 3, gradients of the magnetization do not introduce any noise into the

EDM signal through unwanted frequency shifts. In contrast, initial magnetization gradients in the large tip angle regime will likely be completely random, appearing as an additional source of noise. Frequency shifts due to deformations of the cell are possible, however any such shift will be proportional to the magnetization and decay exponentially. Such shifts could be well characterized and subtracted accordingly. The major disadvantage of performing the experiment in the small tip angle regime is the requirement that we use low T_c SQUIDs, however the low temperatures would also allow the use of superconducting shields which would reduce the magnetic field noise considerably.

5.7 A new configuration for SQUID magnetometers

To the best of the author's knowledge, most SQUID magnetometers are constructed as depicted by the schematic in Fig. 1.7, where the feedback coil couples directly to the SQUID loop. This is convenient for the sake of compactness, however there are two problems associated with this configuration. **1**) Since the flux through the input coil is conserved, the action of the feedback coil induces a supercurrent in the input coil and pickup coil which can influence the evolution of the spins, even if the feedback coil, input coil and SQUID are separated from the pickup coil by a great distance. **2**) Even in open loop mode, the pickup coil will have some back reaction on the spins because the flux through the pickup coil is conserved. The precessing spins induce an AC flux in the pickup coil and to conserve the total flux through the pickup coil, an AC supercurrent flows through the pickup coil, generating an AC magnetic field. This field is in phase with the precessing magnetization which can lead to a small frequency shift if there is a longitudinal component of the magnetization, as discussed in previous sections.

To eliminate both of these problems we propose a modification of the standard SQUID magnetometer, depicted in Fig. 5.7. As in the standard SQUID magnetometer, feedback keeps the flux through the SQUID constant. The flux through the pickup coil is $\Phi_p = L_p I_p = n\Phi_0$, where L_p is the inductance of the pickup coil, I_p is the supercurrent in the pickup coil Φ_0 is the flux quantum. The flux through the SQUID is $\Phi_S = MI_p$ where M

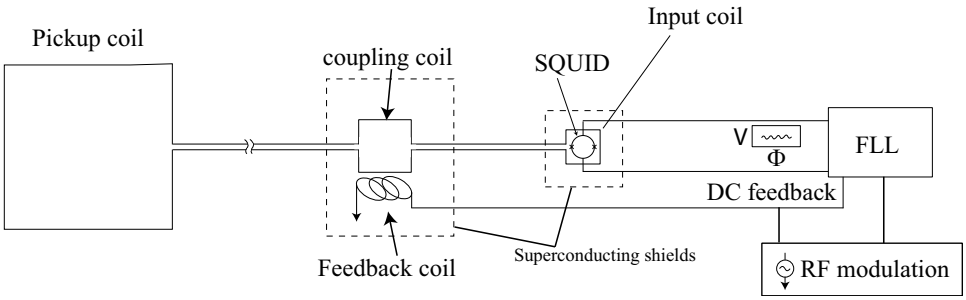

Figure 5.7: Modification of the standard SQUID magnetometer that eliminates any back reaction of the SQUID magnetometer on the spins. Both the feedback coil/coupling coil pair and the SQUID/input coil pair would have their own superconducting shields to isolate them from each other and the pickup coil.

is the mutual inductance between the SQUID and the input coil and of course the current flowing through the input coil and the pickup coil is the same. The action of the feedback coil is to keep the flux through the SQUID loop constant which means that the current I_p through input coil and pickup coil is kept constant, eliminating both problems mentioned above.

Chapter 6

Conclusions

In preparation for performing a search for an electric dipole moment in liquid xenon, we have performed a detailed series of experimental and theoretical studies of long range dipolar interactions in a hyperpolarized liquid. In liquid state NMR experiments the time scale associated with diffusion $\tau_{dif} \sim R^2/D$, where R is the characteristic size of the sample and D is the coefficient of diffusion, can be much longer than the timescale associated with magnetic field inhomogeneities $\tau_{inh} = (\gamma \Delta B)^{-1}$, so that there is no motional narrowing of the applied field. For a sufficiently polarized sample, the time scale associated with dipolar fields $\tau_d \sim (\gamma M)^{-1}$ can be much shorter than either transverse relaxation time or τ_{dif}. Under these conditions, dipolar interaction dictate the spin dynamics of the system.

The behavior of a spin polarized liquid interacting via long range dipolar interactions exhibits a remarkable bifurcation dependent on the tip angle away from the magnetic field. For "small" tip angles, the magnetization is incredibly stable with respect to perturbations. In the absence of dipolar interactions and in the presence of a very large applied field gradient, one would expect the magnetization to wind itself up into a very tight helical pattern, causing a rapid collapse of the overall NMR signal. Instead, we observe both experimentally and through our various models, that the free induction decay time is extended considerably, up to a factor of 100 relative to the non-interacting case in some data sets. Rather than growing linearly in response to a gradient of the applied field, gradients of the

magnetization oscillate coherently, preventing the collapse of the NMR signal. For applied gradients in the longitudinal direction, the gradients of the magnetization are also in the longitudinal direction and generate an oscillating phase difference between the two SQUID signals. For a small ratio of the applied gradients to the magnetization gR/M, the oscillations of the phase difference are quite sinusoidal, in both the data and the simulations. For large gR/M, the phase oscillations become somewhat irregular due to the growth of higher order gradients. The irregularities in the data can be reproduced by the high order models. The dominant mechanism contributing to the decay of the phase oscillations appears to be convection due to small residual thermal gradients. Diffusion plays a very small role in the decay of the phase oscillations.

In the large tip angle regime, dipolar interactions generate a dynamical instability leading to non-linear evolution of the spins. In general, gradients of the magnetization grow exponentially in response to any gradient of the applied magnetic field. In the context of an EDM experiment, we are particularly interested in the response to a linear, longitudinal gradient of the applied field. We have shown that, compared to the non-interacting case, the first order gradients of the magnetization are amplified exponentially with a time constant that can be less than one second for easily achieved parameters. As long as all gradients of the magnetic field and the magnetization are small compared to the magnetization, the phase difference between the SQUID signals can be used to faithfully reproduce the applied field gradient.

6.1 Schemes for measuring an EDM

Given the behavior reviewed above, there are two possible scenarios for conducting a search for search for an EDM.

6.1.1 Large tip angle regime

The dynamical instability that appears at large tip angles presents a very attractive method for measuring an electric dipole moment. Dipolar interactions would amplify spin precession

due to the very small interaction of an electric dipole moment with an electric field gradient, raising it above the noise level of the detectors. This means that measurements can be performed on a much faster time scale, so that the electric field can be reversed more rapidly, thereby avoiding some of the 1/f noise associated with thermal drifts of the magnetic shields. Furthermore, this amplification mechanism reduces both the requirements on the dynamic range and the sensitivity of the SQUID magnetometers.

Precise estimates of the sensitivity based on this method are given in Chapter 5, but to reiterate, for a sample of liquid xenon 1 cm in diameter, with a polarization of 1% ($M_0 = 136\,\mu$G), high T_c SQUID detectors and a collapse time of about 2.3 seconds yielding amplification by a factor of approximately 20 relative to the non-interacting case, a single shot measurement can yield a sensitivity to an EDM at the level of about 1.8×10^{-27} e-cm. To achieve a sensitivity of $10^{-29}\,e\,$cm, this requires about 32400 such measurements, or for 100% duty cycle about 1 day of integration.

We expect that the biggest sources of noise are initial magnetization gradients. Initial gradients of the magnetization grow exponentially, introducing significant noise into the measurement. For the above parameters, initial magnetization gradients at the level of 5×10^{-7} generate noise at the level of about $1.8 \times 10^{-27}\,e\,$cm, on par with the single shot sensitivity. Based on measurements in a similar set of magnetic shields, we estimate the magnetic field gradient noise at the level of $2-3\times10^{-27}\,e\,$cm at time scales of several seconds. Hence, achieving higher sensitivity in a single shot measurement or further reducing initial magnetization gradients does not lead to substantial improvements in sensitivity to an EDM.

The large tip angle regime presents several other technical challenges. To achieve such high initial homogeneity will require active mechanical mixing, introducing a large source of fluid motion. In the presence of any transverse electric fields, motion of the fluid can generate large $\mathbf{v} \times \mathbf{E}/c$ magnetic fields, a serious source of systematic effects. To reduce ambiguity in the size of the electric field, it is desirable to have the electrodes on the inside of the cell which generate large radial fields, exacerbating this effect. Other sources of fluid motion are considered in Chapter 5. In-situ measurement of the fluid motion at the level of

10^{-3} cm/s appears difficult, however, it should be possible to characterize the fluid motion at this level in a mock cell by monitoring the frequency of Rayleigh scattered light from entrained micron sized scattering centers.

6.1.2 Small tip angle regime

Several features of the behavior in the small tip angle regime make it attractive for an EDM experiment. (1) Spectral narrowing allows for long measurement times. (2) Less care will have to be taken to minimize ambient field gradients. (3) The membrane in the center of the cell will be eliminated, greatly simplifying the construction of the cell. (4) There will be no need to mix the sample following each electric field reversal, reducing a major source of fluid motion in the cell. (5) A major source of noise in the large tip angle regime is the fluctuation of initial magnetization gradients. As noted in Chapter 3, for a spherical cell, regardless of the magnetization configuration, the average magnetic field in the cell is always zero. Hence, magnetization gradients do not introduce any frequency shifts. Frequency shifts can arise from a uniformly polarized sample in a cell that deviates from perfect sphericity. These frequency shifts will decay along with the magnetization and hence it should be possible to subtract them if the electric field is reversed on time scales much shorter than the relaxation time.

A major concern in the small tip angle regime is that the large longitudinal component of the magnetization can generate large frequency shifts, because of deformations of the cell or through coupling to the SQUID detectors via the feedback coil. A shift in the density of the sample associated with the electric field is a potential source of systematic errors not present in the large tip angle scheme.

By using two low T_c SQUIDs, one to monitor the nuclear spin precession and one acting as a comagnetometer, as discussed in Chapter 5, it should be possible to realize a sensitivity of $10^{-29}\, e\,$cm in about 3 days of integration. Ultimately this scheme cannot be as sensitive as the large tip angle scheme because the signal to noise ratio is smaller. Furthermore, the baseline of the gradiometer in the large tip angle regime is only about 0.5 cm. In the small

tip angle regime, the baseline formed by the comagnetometer SQUID and the sample is unlikely to be as small, and thus magnetic noise from the magnetic shields will limit the sensitivity.

6.2 Low T_c SQUIDs and superconducting shields

Regardless of which scheme is used to carry out an EDM experiment it is likely that low T_c SQUIDs will be employed. The drawback of low T_c SQUIDs is that they require the use of liquid helium and sophisticated dewars. However, the advantages of using low T_c SQUIDs are many. Most obviously, they have noise characteristics approximately a factor of 10 better than high T_c SQUIDs. Niobium is the most commonly used superconducting material at low temperatures which allows greater flexibility in the design and construction of the pickup coil as niobium is flexible and easy to work with. This point is especially noteworthy as the main difference in the construction of the experiment for the small and large tip angle regimes are the configuration of the SQUID pickup coils. Sheets of niobium or lead could also be used to form a superconducting shield, for which there are no Johnson currents generating magnetic field noise.

6.3 Novel magnetic resonance imaging techniques

An interesting practical application of these types of dynamical instabilities due to dipolar interactions may be found in the field of magnetic resonance imaging. In a 9 T magnet, the thermal polarization of protons is about 3×10^{-5} and for a proton density of about $6 \times 10^{22}\,\mathrm{cm}^{-3}$, this yields a characteristic time scale $\tau_d = (\gamma M)^{-1} \approx 1.5$ sec. The relaxation time in tissue varies, but can be as high as several seconds and thus dipolar interactions can influence spin precession in tissues. It has recently been shown that the combined effects of dipolar fields and radiation damping generate a dynamical instability leading to chaotic behavior, enhanced sensitivity to initial conditions and improved magnetic resonance imaging contrast.[86, 85] The effects discussed in this work do not require radiation damping

and offer another tool for certain types of imaging experiments.

One such possibility is the following: Magnetic source MRI is a technique that detects the response of proton spins to magnetic fields generated by small currents in the sample. It has recently been shown that this technique can be used to detect the magnetic fields generated by neuronal activity.[129] With an appropriate pulse sequence, dipolar interactions may lead to enhanced sensitivity these small magnetic fields. Other applications include the enhanced detection of small magnetization or magnetic field inhomogeneities due to different longitudinal relaxation times or chemical shifts in a tumor could produce exponential growth of magnetization gradients.

6.4 Spin precession and dynamical instabilities

It is worth reiterating some of the points made in the introduction about the sensitivity of spin precession measurements. In numerous experiments, particularly those based on the detection of nuclear spin, the sensitivity of the measurement is limited by the detectors, rather than spin-projection noise. In such cases, substantial improvements in sensitivity can be realized by using dynamical instabilities generated by collective particle interactions to amplify spin precession to a level detectable by sensors of finite sensitivity. In the studies reported here, long range dipolar interactions are responsible for the dynamical instability. Other types of particle interactions have also been shown to generate dynamical instabilities such as spin-exchange between alkali-metal atoms or between alkali-metal and noble-gas atoms. Further study of these types of dynamical instabilities could lead to enhancements in sensitivity of spin precession measurements in other systems.

Chapter 7

Appendix

7.1 Analytical expansion using a Taylor series.

In this method we expand the magnetization into a series of basis functions

$$\mathbf{M}(\mathbf{r},t) = \sum_n \mathbf{m}_i(t) f_i(\mathbf{r}), \tag{7.1}$$

calculate the dipolar field produced by each basis function in terms of other functions in the same basis,

$$\mathbf{B}_{dip}(\mathbf{r})(f_i) = \sum_j \mathbf{b}_j^i f_j(\mathbf{r}), \tag{7.2}$$

and substitute the result into Eq. (3.1). Assuming that products of the basis functions can be expanded into sums over basis functions, the Bloch equations can be reduced to a set coupled ordinary differential equations for the expansion coefficients $\mathbf{m}_i$, which can be easily solved numerically.

The basis function $f_i(\mathbf{r})$ have to satisfy the following requirements:

1. For magnetization given by $f_i(\mathbf{r})$ the resulting dipolar field should be expressible as a sum of $f_j(\mathbf{r})$.

2. A product of $f_i(\mathbf{r})f_j(\mathbf{r})$ should be expressible as a sum of $f_k(\mathbf{r})$.

3. If diffusion is neglected the functions $f_i(\mathbf{r})$ do not need to satisfy any boundary conditions other than being finite at the origin.

4. The functions $f_i(\mathbf{r})$ do not need to be orthogonal over any interval, however the coefficients $\mathbf{m}_i$ and $\mathbf{b}_j^i$ should fall sufficiently fast with i because the series has to be truncated at a finite i.

5. If the magnetization and the gradient are initially symmetric around the z axis, the functions $f_i(\mathbf{r})$ can be cylindrically symmetric as well.

One simple set of basis functions that satisfies all conditions above is a power expansion in z and $\rho = (x^2 + y^2)^{1/2}$. Another advantage of this basis is that it trivially reduces to the linear model with a single z term. Here we set $R = 1$ and consider z and ρ to be dimensionless. To decide which terms need to be included in the expansion, consider how the higher order terms appear during time evolution of the Bloch equations. Initially, only $\mathbf{B}_{ext}$ has a gradient in the z direction. That causes $\mathbf{M}$ to develop a linear gradient in the z direction. To next order a z^2 term appears on the right hand side of Eq. (3.1). If z^2 term is included in the expansion of $\mathbf{M}$ it generates $\mathbf{B}_{dip}$ with terms z^2 and ρ^2. That in turn generated such terms as z^3, z^4, $z\rho^2$, $z^2\rho^2$ and so on. Only even powers of ρ appear in the expansion.

To calculate the dipolar fields created by the magnetization in the form $f_{nm} = z^n(x^2 + y^2)^m$ it is convenient to introduce the scalar magnetic potential [104],

$$\Phi = -\int_V \frac{\nabla' \cdot \mathbf{M}(\mathbf{r}')}{|\mathbf{r} - \mathbf{r}'|} dV' + \oint_S \frac{\mathbf{n}' \cdot \mathbf{M}(\mathbf{r}')}{|\mathbf{r} - \mathbf{r}'|} dS' \tag{7.3}$$

$$\mathbf{H} = -\nabla\Phi \tag{7.4}$$

$$\mathbf{B} = \mathbf{H} + \frac{4\pi}{3}\mathbf{M} \tag{7.5}$$

In the rotating frame it is sufficient to calculate only the potential due to M_z component of magnetization, as can be seen from Eq. (3.20). The dipolar integral from the other two components can be trivially found by replacing in the final result M_z with M_x (M_y), changing B_z to B_x (B_y), and multiplying by $-1/2$. The scalar potential from the $\hat{\mathbf{z}}$ component of the magnetization is

$$\Phi_z = -\int_V \frac{1}{|\mathbf{r} - \mathbf{r}'|} \frac{\partial M_z(\mathbf{r}')}{\partial z'} dV' \tag{7.6}$$

$$+ \oint_S \frac{\hat{n}'_z \cdot M_z(\mathbf{r}')}{|\mathbf{r} - \mathbf{r}'|} dS' = \Phi_{sz} + \Phi_{vz} \tag{7.7}$$

$$\tag{7.8}$$

with $M_z = r^{n+2m} \cos^n(\theta) \sin^{2m}(\theta)$

We make use of the well-known expansion

$$\frac{1}{|\mathbf{r} - \mathbf{r}'|} = 4\pi \sum_{l=0}^{\infty} \sum_{q=-l}^{l} \frac{1}{2l+1} \frac{r_<^l}{r_>^{l+1}} Y_{lq}^*(\theta', \varphi') Y_{lq}(\theta, \varphi) \tag{7.9}$$

to write

$$\begin{aligned} \Phi_{sz} \quad = \quad & \sum_{l=0}^{\infty} \sum_{q=-l}^{l} \frac{4\pi Y_{lq}(\theta, \varphi) r^l}{(2l+1)} \times \\ & \int_{4\pi} \cos^{n+1} \theta' \sin^{2m} \theta' Y_{lq}(\theta', -\varphi') d\Omega' \end{aligned} \tag{7.10}$$

and

$$\begin{aligned} \Phi_{vz} \quad = & -\sum_{l=0}^{\infty} \sum_{q=-l}^{l} \frac{4\pi Y_{lq}(\theta, \varphi)}{(2l+1)} \times \\ & \int_{4\pi} n \cos^{n-1} \theta' \sin^{2m} \theta' Y_{lq}(\theta', -\varphi') d\Omega' \times \\ & \left[\frac{1}{r^{l+1}} \int_{r'=0}^{r} r'^{n+2m+l+1} dr' + r^l \int_{r'=r}^{1} r'^{n+2m-l} dr' \right] \end{aligned} \tag{7.11}$$

The radial integration involves only powers of r and can be done easily. Keeping only $q = 0$ terms because of azimuthal symmetry we can rewrite the potential

$$\Phi_{sz} = \sum_l \frac{4\pi Y_{l0}(\theta, 0) r^l}{(2l+1)} I_1(n+1, m, l) \tag{7.12}$$

and

$$\begin{aligned} \Phi_{vz} \quad = \quad & -4\pi n \sum_l \frac{Y_{l0}(\theta, 0)}{(2l+1)} I_1(n-1, m, l) \\ \times \quad & \left(\frac{r^{n+2m+1}}{(l+2+n+2m)} - \frac{(r^{n+2m+1} - r^l)}{(n+2m-l+1)} \right) \end{aligned} \tag{7.13}$$

where

$$I_1(n, m, l) = \int_{4\pi} \cos^n \theta' \sin^{2m} \theta' Y_{l0}(\theta', -\varphi') d\Omega' \tag{7.14}$$

The angular integration can also be done analytically resulting in:

$$I_1(n,m,l) = 2\sqrt{(2l+1)\pi}\times \\ \sum_{j=0}^{m} C_j^m (-1)^j \frac{(n+2j)!}{(n+2j+l+1)!!(n+2j-l)!!} \tag{7.15}$$

for $n+l$ even and $l \leq n+2m+1$ and 0 otherwise, where $C_j^m \frac{m!}{(m-j)!\,j!}$ are the binomial coefficients. We evaluate these expressions to obtain numerical coefficients for the expansion of the magnetic potential, Eqs. (7.12,7.13). The potential Φ_z is differentiated with respect to z to obtain the magnetic field $B_z(f_{nm})$ which is expressed as an expansion in terms of the basis functions,

$$B_z(f_{nm}) = \sum_{n',m'} b_{n'm'}^{nm} f_{n'm'} \tag{7.16}$$

In the derivation, the following identities are useful

$$(1-t^2)^n t^k = \sum_{m=0}^{n} C_m^n (-1)^m t^{k+2m} \tag{7.17}$$

$$P_n(z) = \frac{1}{2^n} \sum_{k=0}^{n/2} (-1)^k C_k^n C_n^{2n-2k} z^{n-2k} \tag{7.18}$$

and

$$\frac{\partial (r^l \cos^m\theta)}{\partial z} = \frac{\partial}{\partial z} \sum_{k=0}^{(l-m)/2} C_k^{(l-m)/2} z^{2k+m} \rho^{l-m-2k} \\ = \sum_{k=0}^{(l-m)/2} (2k+m) C_k^{(l-m)/2} z^{2k+m-1} \rho^{l-m-2k}. \tag{7.19}$$

7.2 Magnetic field due to square pickup coil

Conveniently, the magnetic field due to a square loop of unit current has a closed form. We use this expression frequently to calculate the signal in the SQUID magnetometers. It may be easier to calculate it directly, but for completeness we include it here. For a loop with sides of length a in the xy plane, the magnetic field for one unit of current in gaussian units is

$$B_x = \frac{1}{c}\left(\frac{\frac{2\sqrt{2}z(a+2y)}{\sqrt{a^2-2a(x-y)+2(x^2+y^2+z^2)}}+\frac{2\sqrt{2}z(a-2y)}{\sqrt{a^2-2a(x+y)+2(x^2+y^2+z^2)}}}{(a-2x)^2+4z^2} + \frac{\frac{2\sqrt{2}z(a-2y)}{\sqrt{a^2+2a(x-y)+2(x^2+y^2+z^2)}}+\frac{2\sqrt{2}z(a+2y)}{\sqrt{a^2+2a(x+y)+2(x^2+y^2+z^2)}}}{(a+2x)^2+4z^2}\right) \tag{7.20}$$

$$B_y = \frac{1}{c}\left(\frac{\frac{2\sqrt{2}z(a+2x)}{\sqrt{a^2+2a(x-y)+2(x^2+y^2+z^2)}}+\frac{2\sqrt{2}z(a-2x)}{\sqrt{a^2-2a(x+y)+2(x^2+y^2+z^2)}}}{(a-2y)^2+4z^2} + \frac{\frac{2\sqrt{2}z(a-2x)}{\sqrt{a^2-2a(x-y)+2(x^2+y^2+z^2)}}+\frac{2\sqrt{2}z(a+2x)}{\sqrt{a^2+2a(x+y)+2(x^2+y^2+z^2)}}}{(a+2x)^2+4z^2}\right) \tag{7.21}$$

$$\begin{aligned} cB_z = {} & \frac{\sqrt{2}(a-2y)}{(a-2y)^2+4z^2}\left(\frac{a+2x}{\sqrt{a^2+2a(x-y)+2(x^2+y^2+z^2)}} + \frac{a-2x}{\sqrt{a^2-2a(x+y)+2(x^2+y^2+z^2)}}\right) \\ & + \frac{\sqrt{2}(a-2x)}{(a+2x)^2+4z^2}\left(\frac{a+2y}{\sqrt{a^2-2a(x-y)+2(x^2+y^2+z^2)}} + \frac{a-2y}{\sqrt{a^2+2a(x+y)+2(x^2+y^2+z^2)}}\right) \\ & + \frac{\sqrt{2}(a+2y)}{(a-2y)^2+4z^2}\left(\frac{a-2x}{\sqrt{a^2-2a(x-y)+2(x^2+y^2+z^2)}} + \frac{a+2x}{\sqrt{a^2-2a(x+y)+2(x^2+y^2+z^2)}}\right) \\ & + \frac{\sqrt{2}(a+2x)}{(a+2x)^2+4z^2}\left(\frac{a-2y}{\sqrt{a^2+2a(x-y)+2(x^2+y^2+z^2)}} + \frac{a+2y}{\sqrt{a^2+2a(x+y)+2(x^2+y^2+z^2)}}\right) \end{aligned}$$

7.3 Quantum non-demolition measurements of spin precession using SQUID magnetometers

The principles of quantum mechanics require that a measurement of a system must perturb its quantum mechanical state. However, in some cases it is possible to set up a quantum

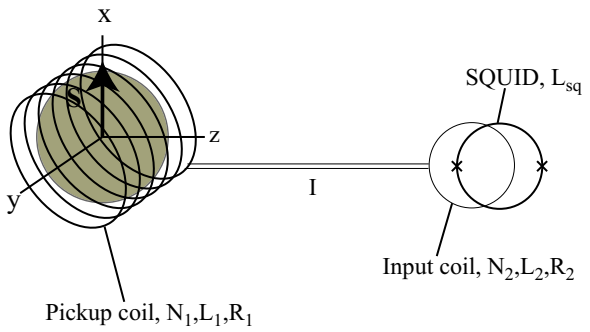

Figure 7.1: Schematic of idealized SQUID-spin coupling configuration.

non-demolition measurement that does not yield complete information about the system, but does not strongly the influence the quantity of interest. In Ref. [78], QND measurements using off resonant light were discussed in the context of atomic magnetometry. We discuss here using SQUID magnetometers for performing quantum non-demolition measurements on spins. The general form of this discussion is similar to that found in Ref. [78].

Consider performing measurements on a system of spins using the setup shown in Fig. 7.1. We assume that a spherical sample of N atoms with gyromagnetic ratio γ with total magnetic moment $m = H\gamma\hbar/2$ is initially polarized in the $\hat{\mathbf{x}}$ direction and is positioned in the center of the pickup coil. For convenience and concreteness, we assume the pickup coil is a solenoid of length a with N_1 turns per unit length, with the symmetry axis oriented along the y direction as shown in Fig. 7.1. The flux induced in the SQUID magnetometer is proportional to m_y and hence a measurement of this flux yields no information about m_x or m_z. Fluctuations of the current in the SQUID generate small fluctuations in the y component of the magnetic field B_{1y} by coupling to the pickup coil via the input coil. This generates noise in m_z by rotating the large component m_x into the z direction, but does not affect m_y. More formally, the interaction of the particles spin with the detection system is $H_I = \frac{\gamma\hbar}{2}\sigma_y B_{1y}$ which trivially commutes with σ_y. Therefore $m_y = \frac{N\gamma\hbar}{2}\langle\sigma_y\rangle$ is a constant of the motion in the presence of the detection system, yielding a quantum non-demolition measurement.

We now ask how well we can determine B_z by measuring the rotation of the spin into

the $\hat{\mathbf{y}}$ direction with the SQUID. The magnetic field is determined by $B_z = \frac{\phi}{\gamma\tau}$ where ϕ is the spin precession angle and τ is the measurement time. The accuracy with which we can measure the spin precession angle is $\delta\phi = \delta m_y/m_x$. For this analysis, we assume that measurements are made on a time scale short compared to the intrinsic relaxation time.

We first note that, as discussed in Refs. [125, 126, 127] the minimum detectable energy change in a SQUID is

$$\delta E = \frac{\delta\Phi^2}{2L_{sq}} = \frac{\delta I^2 L_{sq}}{2} = 16 k_b T\sqrt{L_{sq}C}. \tag{7.22}$$

where C is the Josephson junction shunt capacitance, L_{sq} is the inductance of the SQUID and $\delta\Phi$ is the power spectral density of the flux through the SQUID loop. For temperatures such that $k_b T \ll \hbar/\sqrt{L_{sq}C}$ quantum fluctuations limit the sensitivity to

$$\delta E > \hbar/2. \tag{7.23}$$

In this analysis we will assume our SQUIDs are operating in this regime, and hence the minimum detectable flux through the SQUID for unit bandwidth is

$$\delta\Phi_{sq} = \sqrt{\hbar L_{sq}}. \tag{7.24}$$

We can also interpret this as quantum fluctuations of the current in the SQUID

$$\delta I_{sq} = \sqrt{\frac{\hbar}{L_{sq}}}. \tag{7.25}$$

A change in the flux through the pickup coil Φ_1 generates a current I through the pickup coil and input coil

$$\Phi_1 = I(L_1 + L_2). \tag{7.26}$$

If we express the mutual inductance between SQUID and pickup coil as $M = k\sqrt{L_2 L_{sq}}$, then a change in the flux through the pickup coil leads to a flux in the SQUID

$$\Phi_{sq} = MI = k\frac{\sqrt{L_2 L_{sq}}}{L_1 + L_2}. \tag{7.27}$$

For optimal coupling, $L_2 = L_1$ and

$$\Phi_{sq} = \frac{k}{2}\sqrt{\frac{L_{sq}}{L_1}}\Phi_1 \tag{7.28}$$

We can use the law of mutual inductance, discussed in Chapter 3, to find the flux induced in the pickup coil by the y component of the magnetic moment. Neglecting edge effects, we approximate the magnetic field produced by the solenoid as constant over the sample $B_{1y} = \mu_0 N_1 I$. Hence, the flux through the pickup coil due to m_y is

$$\Phi_1 = m_y \mu_0 N_1. \tag{7.29}$$

Inserting this into Eq. 7.28 the flux through the SQUID is

$$\Phi_{sq} = m_y \frac{k\mu_0 N_1}{2} \sqrt{\frac{L_{sq}}{L_1}} \tag{7.30}$$

Using Eq. 7.24 we find the sensitivity to m_y

$$\delta m_y = \frac{2}{k\mu_0 N_1} \sqrt{\hbar L_1}. \tag{7.31}$$

Finally, the sensitivity to a small magnetic field B_z for measurement time τ is

$$\delta B_z^{sq} = \frac{1}{\gamma\tau} \frac{\delta m_y/\sqrt{\tau}}{m_x} \tag{7.32}$$

$$= \frac{4}{\gamma^2 \tau^{3/2} \mu_0 k N N_1} \sqrt{\frac{L_1}{\hbar}} \tag{7.33}$$

In addition to directly limiting the sensitivity with which the rotation angle can be determined, the magnetic field generated by quantum fluctuations in the SQUID produces relaxation of the sample by causing spin flips. The perturbation acting on the spins, averaged over the sample volume is

$$H_I = \frac{\gamma\hbar}{2} \sigma_y \delta B_{1y}. \tag{7.34}$$

Here δB_{1y} is the magnetic field produced by fluctuating currents in the pickup coil. If we assume all the spins are initially in the state $|\uparrow_x\rangle$ the probability per unit time of making a transition to the $|\downarrow_x\rangle$ state is given by the well known formula

$$W_{+\to-} = \frac{2\pi}{\hbar} \mid \langle\uparrow_x| H_I |\downarrow_x\rangle \mid^2 \frac{1}{\hbar} f(\omega) \tag{7.35}$$

where $f(\omega) = \frac{\Gamma^2/4\hbar^2}{(\omega-\omega_0)^2+\Gamma^2/4\hbar^2}$ is the density of states, $\Gamma = \hbar/T_2$ is the width of the transition and $\int f(\omega) d\omega = 1$. The matrix element is

$$\langle\uparrow_x| H_I |\downarrow_x\rangle = -i \frac{\gamma\hbar}{2} \delta B_{1y}. \tag{7.36}$$

We assume that fluctuations in the SQUID current δI_{sq} are gaussian, and since δB_{1y} is proportional to δI_{sq}, it is easy to integrate Eq. 7.35 over frequency to find the total probability for a transition $|\uparrow_x\rangle \rightarrow |\downarrow_x\rangle$

$$W_{tot} = \frac{\pi}{2}(\delta B_{1y}\gamma)^2. \tag{7.37}$$

To find δB_{1y} we note that the flux through the input coil due to fluctuations of the current in the SQUID loop δI is

$$\delta\Phi_2 = M\delta I_{sq} = k\sqrt{L_2 L_{sq}}\delta I_{sq} = \delta I(L_2 + L_1) \tag{7.38}$$

and therefore the current I through the input and pickup coil, assuming $L_2 = L_1$, is

$$\delta I = \frac{k}{2}\sqrt{\frac{\hbar}{L_1}}. \tag{7.39}$$

Hence, the pickup coil generates a magnetic field at the sample

$$\delta B_{1y} = \frac{\mu_0 k N_1}{2}\sqrt{\frac{\hbar}{L_1}} \tag{7.40}$$

Inserting this into Eq. 7.37 we find

$$W_{tot} = \frac{\pi}{2}\frac{\hbar}{L_1}\left(\frac{\mu_0 k N_1 \gamma}{2}\right)^2 \tag{7.41}$$

This stimulated spin transition rate produces relaxation of the polarization at a rate $\Gamma_{SQUID} = 2W_{tot}$ so that $m_x(t) = m_x(0)e^{-2W_{tot}t}$. Furthermore, it produces a random walk of the $\hat{\mathbf{y}}$ component of the magnetization. The total number of atoms that undergo a stimulated transition during measurement time τ is $N_s = NW_{tot}\tau$ and hence

$$\begin{aligned} \delta m_y^{atom} &= \gamma\hbar/2\sqrt{NW_{tot}\tau} \\ &= \frac{\gamma^2 k\mu_0 N_1}{4}\sqrt{\frac{N\tau\pi\hbar^3}{2L_1}} \end{aligned} \tag{7.42}$$

leading to an uncertainty in the determination of the magnetic field

$$\begin{aligned} \delta B_z^{atom} &= \frac{1}{\gamma\tau}\frac{\delta m_y^{atom}}{m_x} \\ &= \frac{\mu_0 k N_1}{2}\sqrt{\frac{\pi\hbar}{2L_1 N\tau}} \end{aligned} \tag{7.43}$$

Neglecting edge effects, the inductance of the coil is $L_1 = \mu_0 \pi R_1^2 N_1^2 a$. Adding the two contributions 7.32 and 7.43 to the noise of the magnetic field measurement in quadrature, we find

$$\delta B_z^{tot} = \sqrt{\frac{16\pi}{\hbar N^2 \gamma^4 \mu_0 \tau^3}\zeta + \frac{h\mu_0}{8N\tau}\zeta^{-1}} \tag{7.44}$$

where $\zeta = aR_1^2/k^2$. Optimizing Eq. 7.44 with respect to ζ, we find

$$\zeta_{opt} = \frac{\hbar\gamma^2\mu\tau}{8}\sqrt{\frac{N}{2\pi}} \tag{7.45}$$

and

$$\delta B_{z,opt} = \frac{2^{3/4}\pi^{1/4}}{\gamma\tau N^{3/4}}. \tag{7.46}$$

Note that the volume of the sample is $V = a\pi R_1^2 = \pi\zeta/k$. For $N = 10^{22}$ xenon atoms, Eq. 7.45 evaluates to $\zeta_{opt} = 3.6 \times 10^{-9}\,\mathrm{m}^3$. Assuming the coupling between the SQUID and input coil is near unity, this means the sample must be compressed to approximately 10 mm^3.

As pointed out in Ref. [78], if one includes intrinsic relaxation processes with rate Γ_{rel}, one finds that for measurement times T such that $T \gg (N\Gamma_{rel})^{-1}$, the sensitivity becomes

$$\delta B_z = \frac{\sqrt{\Gamma_{rel}}}{\gamma\sqrt{NT}}. \tag{7.47}$$

This is the result for a conventional shot noise limited magnetometer and holds irrespective of the detection system.

7.4 Some useful properties of liquid xenon

Table 7.1 summarizes some useful properties of liquid xenon.

Property	value
gyromagnetic ratio	$\gamma = 1177\,\mathrm{Hz/G}$
density	$[n] = 1.4 \times 10^{22}\mathrm{cm}^{-3}$, $\rho = 2.907\,\mathrm{g/cm}^3$
freezing point	163 K
coefficient of thermal expansion	$\beta' = 0.0023\,\mathrm{K}^{-1}$
dynamic viscosity	$\nu = 0.0015\,\mathrm{cm}^2/\,\mathrm{sec}$
coefficient of diffusion	$D = 2 \times 10^{-5}\,\mathrm{cm}^2/\,\mathrm{sec}$
index of refraction	$n = 1.4$
dielectric constant	$K = 1.5$
atomic polarizability	$\alpha = 4.4 \times 10^{-40}\mathrm{C} - \mathrm{m}^2/\mathrm{V}$
^{129}Xe natural abundance	26%
thermal conductivity	$\lambda = 7000$ erg/(cm-s-K)
heat capacity	$c_p = 3.5 \times 10^6$ erg/(g-K)

Table 7.1: Properties of liquid xenon.

References

[1] E.M. Purcell and N.F. Ramsey, Phys. Rev. **78**, 807 (1950).

[2] D.H. Smith, E.M. Purcell and N.F. Ramsey, Phys. Rev. **108**, 120 (1957).

[3] M.V. Romalis *et. al.*, Phys. Rev. Lett. **86**, 2505 (2001).

[4] M.A. Rosenberry and T.E. Chupp, Phys. Rev. Lett. **86**, 22 (2001).

[5] P.G. Harris *et al.*, Phys. Rev. Lett. **82**, 904 (1999).

[6] B.C. Regan *et al.*, Phys. Rev. Lett. **88**, 071805 (2002).

[7] C.S. Wu *et al.*, Phys. Rev. **105**, 1413 (1957).

[8] L.D. Landau Zh. Eksp. Theor. Fiz. **32**, 405 (1957) [Sov. Phys. JETP **5**, 405 (1957)]; Nucl. Phys. **3**, 127 (1957).

[9] J.H. Christensen, J.W. Cronin, V.L. Fitch and R. Turlay, Phys. Rev. Lett. **13**, 138 (1964).

[10] *The Physics of Time Reversal* R.G. Sachs (The University of Chicago Press, 1987).

[11] *CP Violation Without Strangeness*, S.K. Lamoreaux and I.B. Khriplovich, (Springer, 1997).

[12] A.D. Sakharov, Pis'ma ZhETF **5**32 (1967) [Sov. Phys. JETP Lett., **5**, 24 (1967)].

[13] M.E. Shapushnikov, Pis'ma ZhETF **44**, 364 (1986) [JETP Lett,**44**, 465 (1986)]; M.E. Shaposhnikov, Nucl. Phys. **B287**, 757 (1987).

[14] P. Huet, hep-ph/9406301 v2 (1994).

[15] P. Huet, A. E. Nelson, Phys. Rev. D **53**, 4578 (1996).

[16] M. Berkooz, Y. Nir, T. Volansky, Phys. Rev. Lett. **93**, 051301 (2004).

[17] M. Trodden, Rev. Mod. Phys. **71**, 1463 (1999).

[18] *The Quantum Theory of Fields, Volume 3* Steven Weinberg (Cambridge University Press, 2000).

[19] M.G. Kozlov and D.P. DeMille, Phys. Rev. Lett. **89**, 133001 (2002); D. Kawall, F. Bay, S. Bickman, Y. Jiang, and D. DeMille, Phys. Rev. Lett. **92**, 133007 (2004).

[20] T.A. Falk, K.A. Olive, M. Pospelov and R. Roiban, Nucl. Phys. **B560** (1999).

[21] J.S.M. Ginges, V.V. Flambaum, Physics Reports **397**, 63 (2004).

[22] A.M. Martensson-Pendrill, Phys. Rev. Lett. **54**, 1153 (1985).

[23] S.M. Barr, Int. J. Mod. Phys. **8**, 209 (1993).

[24] P.G.H. Sandars, Phys. Lett. **14**, 194 (1965).

[25] Z.W. Liu and H.P. Kelly, Phys. Rev. A **45**, R4210 (1992).

[26] A.M. Martensson-Pendrill and P. Oster, Physica Scripta **36**, 444 (1987).

[27] L.I. Schiff, Phys. Rev. **132**, 2194 (1963).

[28] P.G.H. Sandars, Phys. Rev. Lett. **19**, 1396 (1967).

[29] V. Spevak, N. Auerbach, V.V. Flambaum Phys. Rev. C **56**, 1357 (1997).

[30] V.V. Flambaum and J.S.M. Ginges, Phys. Rev. A **65**, 032113 (2002).

[31] J. Engel, J.L. Friar, and A.C. Hayes, Phys. Rev. C **61**, 035502 (2000).

[32] V.V. Flambaum and V.G. Zelevinsky, Phys. Rev. C **68**, 035502 (2003).

[33] O.P. Sushkov, V.V. Flambaum, I.B. Khriplovich, Zh. Exp. Teor. Fiz. **87**, 1521 (1984)[Sov. Phys. JETP **60**, 873 (1984)].

[34] V.A. Dzuba, V.V. Flambaum, J.S.M. Ginges, M.G. Kozlov, Phys. Rev. A **66**, 012111 (2002).

[35] V.V. Flambaum, I.B. Khriplovich and O.P. Sushkov, Physics Letters **162B**, 213 (1985).

[36] R.J. Crewther, P.Di Vecchia, G. Veneziano, and E. Witten, Phys. Lett. **88B**, 123 (1979); **91B** 487(E) (1980).

[37] R.D. Peccei and H.R. Quinn, Phys. Rev. Lett. **38**, 1440 (1977); Phys. Rev. D **16**, 1791 (1977).

[38] S. Weinberg, Phys. Rev. Lett. **40**, 223 (1978).

[39] F. Wilczek, Phys. Rev. Lett. **40**, 279 (1978).

[40] S.M. Barr, Phys. Rev. Lett. **68**, 1822 (1992).

[41] T. Ibrahim and P. Nath, Phys. Rev. D **57**, 478 (1998).

[42] E.N. Fortson, P.G.H. Sandars, and S.M. Barr, Physics Today **56**, 33 (2003).

[43] T.G. Vold, F.J. Raab, B. Heckel, and E.N. Fortson, Phys. Rev. Lett. **52**, 2229 (1984).

[44] S.E. Derenzo *et. al.*, Phys. Rev. A **9**, 2582 (1974).

[45] H.C. Torrey, Phys. Rev. **130**, 2306 (2004).

[46] E.R. Hunt and H.Y. Carr, Phys. Rev. **130**, 2302, (1963)

[47] B. Driehuys *et al.*, Appl. Phys. Lett. **69** , 1668 (1996).

[48] P. Anthony *et. al.*, Phys. Rev. Lett. **71**, 959 (1993).

[49] E.E.De Lange *et al.*, Radiology **210**, 851 (1999).

[50] T.W. Kornack and M.V. Romalis, Phys. Rev. Lett. 89, 253002 (2002).

[51] D. Bear *et al.*, Phys. Rev. Lett. **85**, 5038 (2000). Phys. Rev. Lett. 89, 253002 (2002).

[52] M.A. Rosenberry and T.E. Chupp, Phys. Rev. Lett. **86**, 22 (2001)

[53] T.G. Walker, W. Happer, Rev. Mod. Phys., **69**, 629 (1997).

[54] Alan Corney, *Atomic and Laser Spectroscopy* (Oxford University Press, Oxford, England, c1997)

[55] W. Happer, Rev. Mod. Phys. **44**, 169 (1972).

[56] W. Happer *et. al.*, Phys. Rev. A. **29** 3092 (1984).

[57] T.G. Walker, Phys. Rev. A **40**, 4447 (1989).

[58] R.M. Herman, Phys. Rev. Lett. **137**, A1062 (1965).

[59] Z. Wu, T.G. Walker, W. Happer, Phys. Rev. Lett. **54**, 1921 (1985).

[60] L.W. Anderson, F.M. Pipkin, J.C. Baird, Phys. Rev. **120**, 1279 (1960)

[61] N.D. Bhaskar, W.Happer, and T. McClelland, Phys. Rev. Lett., **49**, 25 (1982).

[62] I.K. Kominis, T.W. Kornack, J.C. Allred, and M.V. Romalis, Nature **422**, 596 (2003).

[63] J.C. Gallop,*SQUIDS, the Josephson effects and superconducting electronics* , Bristol, England ; Philadelphia : Adam Hilger, c1991

[64] *Principles of Superconductive Devices and Circuits* T. Van Duzer, C.W. Turner (Elsevier, 1981).

[65] K.L. Sauer, R.J. Fitzgerald, and W. Happer, Chem. Phys. Lett. **277**, 153 (1997); K.L Sauer, Ph.D. Thesis, Princeton University, 1998.

[66] R.S. Mulliken, J. Chem. Phys. **52** , 5170 (1970).

[67] W.A. Herrebout, A.A. Stolov, E.J. Sluyts, B.J. van der Veken, Chem. Phys. Lett. **295** 223, (1998).

[68] W.M. Yen and R.E. Norberg, Phys. Rev. **131**, 269 (1963).

[69] C.H. Tseng, R.W. Mair, G.P. Wong, D. Williamson, D.G. Cory, and R.L. Walsworth, Phys. Rev. E **59**, 1785 (1999).

[70] M.V. Romalis, Appl. Phys. Lett. **77**, 1080 (2000).

[71] SpinCore Technologies Inc., Gainesville, FL 32653, USA.

[72] S. Meiboom and D. Gill, Rev. Sci. Instr. **29**, 688 (1958).

[73] M. V. Romalis and M. P. Ledbetter, Phys. Rev. Lett. **87**, 067601 (2001).

[74] A.N. Youdin *et al.*, Phys. Rev. Lett. **77**, 2170 (1996).

[75] A. Kuzmich, L. Mandel, and N.P. Bigelow, Phys. Rev. Lett. **85** 1594 (2000).

[76] J.M. Geremia, J.K. Stockton and H. Mabuchi, Science **304**, 270, (2004).

[77] A. André, A. S. Sørensen, and M. D. Lukin, Phys. Rev. Lett. **92**, 230801 (2004).

[78] M. Auzinsh *et al.*, Phys. Rev. Lett. **93**, 173002 (2004).

[79] S. Vasilyev, J. Jývinen, A. I. Safonov, A. A. Kharitonov, I. I. Lukashevich, and S. Jaakkola, Phys. Rev. Lett. **89**, 153002 (2002).

[80] W.M. Klipstein, S.K. Lamoreaux, and E.N. Fortson, Phys. Rev. Lett. **76**, 2266 (1996).

[81] S. Giovanazzi, A. Grlitz, and T. Pfau, Phys. Rev. Lett. **89**, 130401 (2002).

[82] D. DeMille, Phys. Rev. Lett. 88, 067901 (2002).

[83] J. A. Sidles et al., Rev. Mod. Phys. **67**, 249 (1995).

[84] K. R. Thurber, L. E. Harrel, and D. D. Smith, J. Magn. Reson. **162**, 336 (2003).

[85] Y.-Y. Lin, N. Lisitza, S. Ahn, and W. S. Warren, Science **290**, 118 (2000).

[86] W.S. Warren *et al.*, Science **281**, 247 (1998).

[87] B. Villard and P.J. Nacher, Physica B **284**, 180 (2000).

[88] K. L. Sauer, F. Marion, P.-J. Nacher, and G. Tastevin, Phys. Rev. B **63**,184427 (2001).

[89] P.J. Nacher, N. Piegay, F. Marion, G. Tastevin, J. Low Temp. Phys. **126**, 145 (2002).

[90] D. Candela, M.E. Hayden, and P.J. Nacher, Phys. Rev. Lett. 73, 2587 (1994).

[91] J. Jeener, Phys. Rev. Lett. **82**, 1772 (1999).

[92] J. Jeener, J. Chem. Phys. **116**, 8439 (2002).

[93] N. N. Kuzma, B. Patton, K. Raman, and W. Happer, Phys. Rev. Lett. **88**, 147602 (2002).

[94] T.J. Sumner, J.M. Pendlebury, K.F. Smith, J. Phys D: Appl Phys **20** 1095 (1987)

[95] C. Ciofi et al. IEEE Transactions on Instrumentation and Measurement **47** 1, 9456 (1998).

[96] M.P. Ledbetter *et al.* J. Chem. Phys. **121**, 1454 (2004).

[97] M.P. Ledbetter, I.M. Savukov and M.V. Romalis, Phys. Rev. Lett. **94**, 060801 (2005).

[98] J.Jeener, A. Vlassenbroek, and P.J. Broekaert, J. Chem. Phys. **103**, 1309 (1995).

[99] S. Lee, W. Richter, S. Vathyam, and W.S. Warren, J. Chem. Phys. **105**, 874 (1996).

[100] J. Jeener, J. Chem. Phys. **112**, 5091 (2000).

[101] M.P. Ledbetter and M.V. Romalis, Phys. Rev. Lett. **89** 287601 (2002).

[102] G. Deville, M.Bernier, and J.M. Delrieux, Phys. Rev. B **19**, 5666 (1979)

[103] T. Enss, S. Ahn, and W. S. Warren, Chem. Phys. Lett **305**, 101 (1999).

[104] *Classical Electrodynamics*, J.D. Jackson (John Wiley and Sons, Inc. New York, 1975),2nd ed.

[105] A. Abragam, Principles of Nuclear Magnetic Resonance, (Oxford University, London, 1961), Chap. 3

[106] *Numerical Recipes in C: the art of scientific computing*, W.H.Press et al. (Cambridge University Press, Cambridge, 1992), 2nd ed.

[107] J. Naghizader and S.A. Rice, J. Chem. Phys. **36** 2710 (1962)

[108] W.M. Yen and R.E. Norberg, Phys. Rev. 131, p 269 (1963).

[109] J. Nenonen, J. Montonen, and T. Katila, Rev. Sci. Instrum. **67**, 2397 (1996).

[110] B.I. Shraiman and E.D. Siggia, Nature **405**, 639 (2000).

[111] D. Rothstein, E. Henry, and J.P. Gollub, Nature **401**, 770 (1999).

[112] E.S. Szalai and F.J. Muzzio Phys. Fluids **15** 3274 (2003).

[113] L.D. Landau and E.M. Lifshitz, *Fluid Mechanics 2nd ed.*, (Pergamon Press, 1987).

[114] J.M. Pendlebury *et al.* Phys. Rev. A **70**, 032102 (2004).

[115] S.K. Lamoreaux and R. Golub, nucl-x/0407005 v4 (2004).

[116] A.D. Buckingham and D.A. Dunmur, Trans. Faraday. Soc. **64**, 1776 (1968).

[117] E.D. Commins, S.B. Ross, D. DeMille and B.C. Regan, Phys. Rev. A **50**, 2960 (1994).

[118] E.D. Commins, Am. J. Phys. **59**, 1077 (1991).

[119] *Thermophysical properties of Neon, Argon, Krypton, and Xenon* V.A. Rabinovich, A.A. Vasserman, V.I Nedostup, L.S. Veksler (Springer-Verlag, 1988).

[120] L. Hellemans, M. De Maeyer, Chem. Phys. Lett. **146**, 609 (1988).

[121] J.Van Der Elsken and J.C.F Michielsen, Chem. Phys. Lett. **115**, 230 (1985).

[122] *Electrodynamics of Continuous Media* L.D. Landau, E.M. Lifshitz and L.P. Pitaevskii, 2nd Ed. (Pergamon Press, 1984).

[123] Y.Yeh and H.Z. Cummins, Appl. Phys. Lett. **4**, 176 (1964).

[124] A.C. Sinnock and B.L. Smith, Phys. Rev **181**, 1297 (1968).

[125] J.M. Martinis, J. Clarke, IEEE Trans. Magn. **19** 446 (1983).

[126] V.V. Danilov, K.K. Likharev and A.B. Zorin, IEEE Trans. Magn. **19** 572 (1983).

[127] J. Gallop, Supercond. Sci. Technol. **16**, 1575 (2003).

[128] Tristan Technologies, Inc., 6185 Cornerstone Court East, Suite 106 San Diego, CA 92121, USA.

[129] J. Xiong, P.T. Fox and J.-H. Gao, Human Brain Mapping **20**, 41 (2003).

[130] A.A.Babaei Brojeny and J.R. Clem, Phys. Rev. B **68**, 174514 (2003).